Title
Integration of GPS/INS and Magnetic Markers for Advanced Vehicle Control

Authors
Farrell, Jay
Barth, Matthew

Publication Date
2001-12-01

CALIFORNIA PATH PROGRAM
INSTITUTE OF TRANSPORTATION STUDIES
UNIVERSITY OF CALIFORNIA, BERKELEY

Integration of GPS/INS and Magnetic Markers for Advanced Vehicle Control

Jay Farrell, Matthew Barth
University of California, Riverside

California PATH Research Report
UCB-ITS-PRR-2001-38

This work was performed as part of the California PATH Program of the University of California, in cooperation with the State of California Business, Transportation, and Housing Agency, Department of Transportation; and the United States Department of Transportation, Federal Highway Administration.

Final Report for TO 4213

December 2001

ISSN 1055-1425

Integration of GPS/INS and Magnetic Markers for Advanced Vehicle Control

Final Report

Principal Investigator: Jay Farrell
Department of Electrical Engineering
University of California, Riverside
farrell@ee.ucr.edu

Co-Principal Investigator: Matthew Barth
Center for Environmental Research and Technology
University of California, Riverside
barth@cert.ucr.edu

September 20, 2001

Abstract

This report describes the results of a project supported by California Partners for Advanced Transit and Highways (PATH). The main objective of the project was to develop and demonstrate a triple redundancy navigation system incorporating magnetometer, inertial, and carrier phase differential Global Positioning System (GPS) measurements. The motivating application for this project was lateral vehicle control. Therefore, the system was design to operate reliably whether or not GPS and magnetometer measurements were available. The navigation system provides vehicle position, velocity, acceleration, attitude, heading, and angular rates at 150 Hz with accuracies (standard deviation) of 1.5 cm, 0.8 cm/s, 2.2 cm/s/s, 0.03 deg, 0.1 deg, and 0.1 deg/s. This navigation state vector was processed to produce a control state vector at approximately 30 Hz. This triplicate redundancy navigation system reliably demonstrated lateral vehicle control in the following situations: both GPS and magnetometer aided INS, GPS aided INS, magnetometer aided INS, and switching between GPS and magnetometer aiding of the INS at random times. The control demonstrations involved basic trajectory following as well as trajectory relative maneuvering (i.e., tracking sinusoidal perturbations and performing lane changes). These trajectory relative maneuvers were performed at arbitrary locations along the trajectory.

Executive Summary

The objective of this project was to achieve the navigation performance and reliability necessary for automated vehicle control by designing, analyzing, developing, and evaluating an integrated sensing system involving magnetometer and GPS aided INS. A key motivation for the project is the fact that no single sensing system would be capable of achieving the high level of reliability required for successful AVCSS implementation; therefore, information from a suite of sensors must be fused, with appropriate fault detection logic, to achieve the necessary level of reliability. The entire project was a 20 month effort with the resulting integrated navigation system demonstrated within the PATH AVCSS. The navigation system provides vehicle position, velocity, acceleration, attitude, heading, and angular rates at 150 Hz with accuracies (standard deviation) of 1.5 cm, 0.8 cm/s, 2.2 cm/s/s, 0.03 deg, 0.1 deg, and 0.1 deg/s. This triplicate redundancy navigation system reliably demonstrated lateral vehicle control in the following situations: both GPS and magnetometer aided INS, GPS aided INS, magnetometer aided INS, and switching between GPS and magnetometer aiding of the INS at random times. The control demonstrations involved basic trajectory following as well as trajectory relative maneuvering (i.e., tracking sinusoidal perturbations and performing lane changes). These trajectory relative maneuvers were performed at arbitrary locations along the trajectory. This project leveraged previous PATH research efforts including the carrier-phase differential GPS-aided INS developed by UCR under MOU 292, the demonstration and evaluation results and experience of MOU 374, and the magnetometer and vehicle control experience of the PATH researchers. The project was a collaborative effort between PATH and UCR researchers.

Contents

1 Project Introduction

Automated vehicle position control systems for an AHS require both a means for determining vehicle position and a means for affecting the vehicle position [18, 30]. This project focused on the accurate determination of the vehicle state, which includes the vehicle position.

The vehicle position may be determined in either relative (e.g., position relative to nearby known point) or absolute (e.g., latitude, longitude, altitude) coordinates. A variety of reference positioning systems have been considered: embedded wires [7, 17, 18], embedded magnets [30, 38], radar [18, 26], vision [9, 8, 24, 20, 27, 29, 31], INS and DGPS technology [10, 11, 33, 34, 35, 36, 37]. This effort has focused on research to develop, analyze, and demonstrate a magnetometer and DGPS aided INS with accuracy (cm's), sample rate (> 25 Hz), and latency (< 0.01 s) sufficient for vehicle control.

Taken independently, any positioning system of interest has advantages and disadvantages. The strongest criticism of any of the individual sensing techniques is that it is susceptible to a single point failure. Therefore, no single reference system can supply adequate reliability and availability to ensure safe longitudinal and lateral control. However, used jointly (with effective sensor fusion and fault detection techniques) the overall performance and reliability of the system can be significantly improved by a sensor suite including at least three sensors each with a different operating principle.

Consider, for example, a system incorporating an embedded magnet reference system (EMRS), DGPS positioning, and an Inertial Navigation System (INS). A desired path would be specified in global coordinates to pass through the locations of the embedded markers that specify an automated lane (see Section C.1). The INS would provide estimates of vehicle state and position relative to the desired trajectory (see Section C.2)at a rate high enough to satisfy control system requirements, even though the EMRS and GPS measurements occur at a slower rate. While near the desired trajectory, the three available redundant estimates of vehicle position relative to the desired path would allow effective fault detection and isolation. When the vehicle was significantly off the desired trajectory (e.g., lane changing, entering/leaving a platoon, initialization, disturbances), where the EMRS losses accuracy, the DGPS and INS systems would still provide the accurate position information necessary to complete the maneuver of interest. In addition, knowledge of global vehicle position would facilitate both the process of negotiating maneuvers with neighboring vehicles and the process of determining relative vehicle position and velocity. In situations where the GPS signals are temporarily blocked, the EMRS aided INS would continue to provide accurate lateral position information for vehicle control (see Section 4.1).

The project scope, objectives, and motivation are described in the following section. Subsequent sections describe the methodology, performance analysis, and results. The appendices provide detailed information about the INS, GPS, and control calculation methods. This report describes both the magnetometer/DGPS/INS approach and results that are the specific objectives of this research effort and a two antenna DGPS aided INS system that was implemented as a portion of the Ph.D. research of a student working on the project. The only reason that the two systems were not jointly implemented is that the project computer did not have enough serial ports available. As the analysis and experimental results show, either system can measure the position to cm accuracy and the vehicle attitude, including heading, to better than 0.1 degree.

2 Project Scope and Objectives

2.1 Scope

This project developed an *integrated* carrier phase differential GPS/magnetometer/INS navigation system. The system was designed to overcome the limitations of each independent sensing system. In addition, the system was designed to achieve the triplicate sensor redundancy necessary for the reliable level of performance required for successful commercialization. The scope of this project includes design, analysis, implementation, and evaluation of the integrated system.

2.2 Motivation

The *integrated* carrier phase differential GPS/magnetometer/INS system has several distinct advantages:

High-Sample Rate - Inclusion of the INS system provides state variable estimates at 150 Hz, significantly faster than the magnetometer or GPS systems could alone. The sample rate is also independent of vehicle velocity and independent of the availability of magnetometer or GPS measurements. The higher sample rate allows higher bandwidth vehicle control, as may be required for emergency maneuvering.

Triple Redundancy - Safe vehicle operation will require the ability to detect, isolate, and accommodate sensor failures. Reliable sensor fault isolation requires triplicate redundancy. No single sensing system will be capable of providing the integrity necessary for reliable vehicle control over a highway system.

Preview Information - Implementation within a global coordinate system (such as the WGS 84 system of GPS) enables detailed trajectory information (e.g., curvature, super-elevation, velocity profiles, entrance/exit trajectories) to be stored and available onboard the vehicle. The availability of this information enables accurate anticipation of the reference trajectory without differentiation of the on-line measurements.

Forward Projection - Projection of the control state in advance of the vehicle (equivalent to lead control) is dependent on accurate knowledge of the future trajectory and the current trajectory-relative vehicle heading and heading rate. Two techniques to accurately determine vehicle heading are discussed herein. This information will be attained from the proposed integrated navigation system without differentiation, resulting in improved signal quality; hence, more accurate forward projection.

Reduced Infrastructure Cost - Since the proposed integrated navigation system sensor suite provides redundant sensor information, it should be possible to increase the magnet spacing and reduce the number of magnets used per mile in regions where the highway has a clear view of the sky, thus reducing overall infrastructure cost. Alternatively, the magnetometers will be spaced closely (1.2 m) in areas (e.g., valleys or tunnels) where reception of at least 4 independent GPS satellite signals cannot reliably be expected. This combined approach achieves increased overall system reliability at lower infrastructure cost.

Richer State Information - The integrated system not only provides off-track position information, but also provides additional variables for high performance vehicle control (e.g., position, velocity, acceleration, attitude and angular rates). This information not only allows improved control in normal operation, but may be necessary in more demanding emergency situations.

Advanced Maneuver Capability - The integrated navigation system reliably calculates the trajectory relative vehicle state information regardless of the vehicle distance from the trajectory. This capability enables closed loop advanced (e.g., lane changing, AHS entry and exit, platoon merging) and emergency maneuvering (e.g., interrupting an advanced maneuver).

Lane Departure Warning - Since the integrated navigation system will maintain an accurate estimate of the trajectory-relative vehicle state (independent of off-track distance), lane departure can be accurately and reliably predicted. Therefore, in the interim period prior to highway automation, the integrated system would serve as a reliable lane departure warning system.

2.3 Objectives

This project had the following main objective: to develop, analyze, implement, and evaluate an integrated GPS and magnetometer aided INS for AVCSS. This objective integrated and further developed results of previous PATH research to achieve the reliability and robustness necessary for successful commercial applications. Although either the GPS/INS or magnetometer based navigation system is capable of achieving the performance and capabilities desired for AVCSS, neither by itself could achieve the high level of reliability (i.e., triplicate sensor redundancy) necessary to field a successful commercial system.

3 Methodology

Figures 1 and 2 show the block diagrams of the magnetometer/GPS/INS and two antennae differential carrier phase (DCP) GPS/INS. This implementation is referred to as a complementary filter [3]. The Inertial Measurement Unit (IMU) outputs are processed by the INS. Since the INS is an integration process, the outputs of the INS can be accurately modeled as the actual state plus a predominantly low frequency error (see Appendix B.2 and B.3). The INS outputs are processed to provide estimates of the differential GPS pseudorange, Doppler, magnetometer and integer resolved phase DCPGPS measurements. The differences between the estimated and measured signals contain two noise components—the predominantly low frequency INS component and the predominantly high frequency magnetometer or GPS component. The frequency content of each noise component can be accurately modeled. The objective of the state estimation design

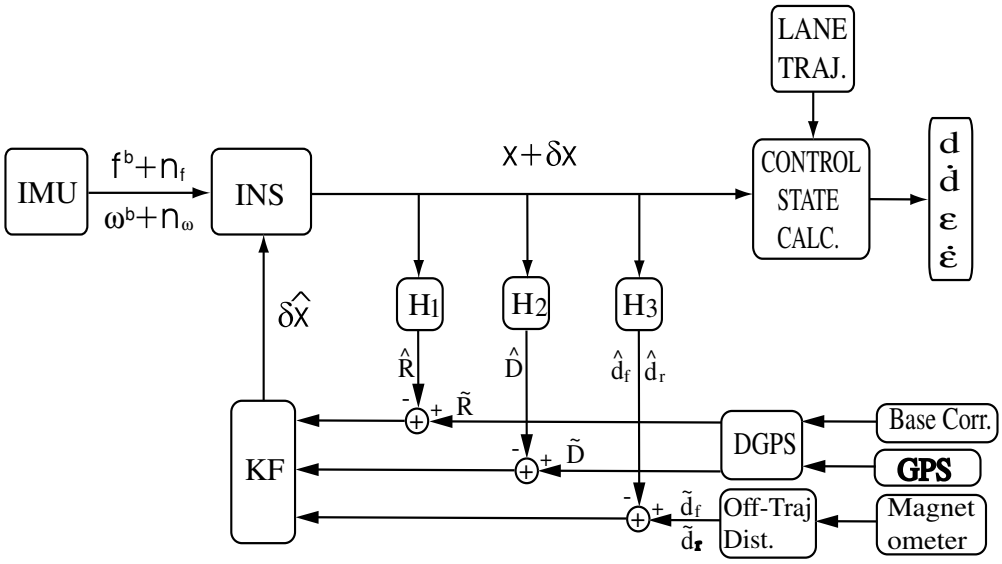

Figure 1: Complementary Filter for the Magnetometer/DCPGPS/INS System Integration

is to attenuate the magnetometer or GPS measurement noise and provide accurate estimates of the INS residual states. Therefore, the state estimator has a predominantly low pass characteristic. Subtracting the estimated residual state estimates from the INS states, in a well designed system, produces an accurate estimate of the navigation states. As shown in Figures 1 and 2, the complementary filter was implemented in a feedback form.

In the complementary filter approach, the INS is the primary navigation system which calculates the navigation states at a high rate for control, guidance, and navigation functions. The magnetometer or GPS aiding information is used when it is available and satisfies conditions designed to verify the proper sensor operation. When such aiding sensor information is not available or judged inaccurate, the INS continues its normal (unaided) operation. During either aided or unaided operation, the error covariance matrices propagated within the state estimation approach predict the accuracy of the state estimates. Such measures of the navigation accuracy are useful in higher level reasoning loops.

The main advantages of the complementary filter approach selected for this implementation are:

1. High rate INS navigation outputs are available without latency regardless of the availability and latency of the magnetometer or GPS aiding information;

2. Inputs to the Kalman filter can be accurately and properly modeled as stochastic processes, as appropriate for the technique [3];

3. Computationally intensive Kalman filter covariance propagation equations can be implemented at a low update rate even though the navigation state is calculated at 150 Hz.

Corresponding to the complementary filter of Figures 1 and 2, differential GPS is discussed in Appendix A, the magnetometer is discussed in [38], and the INS and its error states are discussed in Appendix B. The complementary filter implementation is detailed below.

3.1 INS

The INS operates in the fixed tangent frame at 150 Hz. The origin is fixed at the location of the base station antenna phase center. The navigation states include: north, east, and vertical (down – positive) positions in m; north, east, and down velocity in m/s; roll, pitch, and yaw angles in rad; platform frame gyro drift rates in rad/s; and platform frame accelerometer bias in m/s^2. The navigation error states are identical with the navigation states with the exception of the attitude errors. The attitude errors are estimated in the tangent frame as the north, east, and down tilt errors. This section discusses and analyzes the system integration and data fusion methodologies.

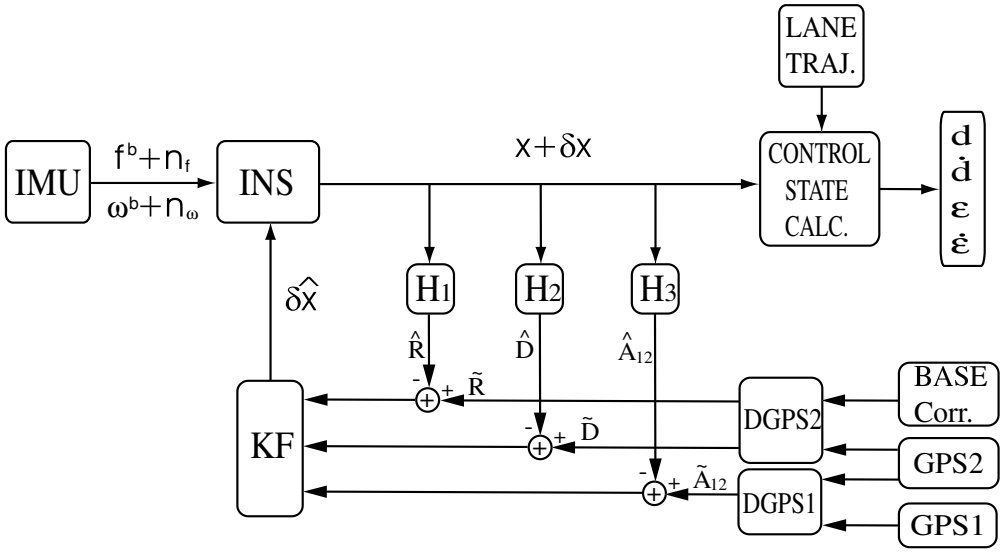

Figure 2: Complementary filter for the two antennae integer-resolved DCPGPS/INS.

3.1.1 Continuous time model

To implement the complementary filter discussed above, an extended Kalman Filter is used. The residual error state estimation is implemented based on the linearized error dynamics presented in eqn. (102). The outputs of the INS system serve as the reference trajectory around which the system residual error equations are linearized. The fifteen residual states are

$$\delta\mathbf{x} = \begin{bmatrix} \delta\mathbf{p} \\ \delta\mathbf{v} \\ \delta\rho \\ \mathbf{x}_a \\ \mathbf{x}_g \end{bmatrix} \tag{1}$$

with three position residual states in tangent frame, three velocity residual states in tangent frame, three rotation error angles, three accelerometer bias states and three gyroscope bias states. Eqn. (102) is the continuous time linearized INS error dynamic equation. The discrete time implementation of the Kalman filtering requires a discrete time state propagation matrix, $\mathbf{\Phi}$, and a discrete time process noise covariance matrix, $\mathbf{Q_d}$. Appropriate expressions for these two quantities are discussed in the following subsection.

3.1.2 Calculation of discrete time state transition matrix and process noise covariance matrix

The discrete time state transition can be described as

$$\delta\mathbf{x}_{k+1} = \mathbf{\Phi}_{((k+1)T_{gps},kT_{gps})}\delta\mathbf{x}_k + \omega_{d(k)} \tag{2}$$

with covariance propagation

$$\mathbf{P}_{k+1} = \mathbf{\Phi}_{((k+1)T_{gps},kT_{gps})}\mathbf{P}_k\mathbf{\Phi}^T_{((k+1)T_{gps},kT_{gps})} + \mathbf{Q_d}_k. \tag{3}$$

For best performance, these variables should be calculated online [13], as they depend on the measured specific force vector, the body to tangent frame rotation matrix, and the geodetic latitude as specified in eqn. (99). For the linearized error dynamics of eqn. (102), the terms $\mathbf{F}_{vp}$, $\mathbf{F}_{vv}$, $\mathbf{F}_{\rho p}$ and $\mathbf{F}_{\rho\rho}$ are all small ($< 10^{-6}$) and will be neglected in the calculation of $\mathbf{\Phi}$.

By setting the specified terms to zero and expanding the power series of $e^{\mathbf{F}t} = \mathbf{I} + \mathbf{F}t + \frac{1}{2}(\mathbf{F}t)^2 \ldots$, the

following equation results

$$\mathbf{\Phi}_{(t_2,t_1)} = \begin{bmatrix} \mathbf{I} & \mathbf{F}_{pv}T_2 & \frac{1}{2}\mathbf{F}_{pv}\mathbf{F}_{v\rho}T_2^2 & \frac{1}{3}\mathbf{F}_{pv}\mathbf{F}_{v\rho}\mathbf{F}_{\rho g}T_2^3 & \frac{1}{2}\mathbf{F}_{pv}\mathbf{F}_{va}T_2^2 \\ \mathbf{0} & \mathbf{I} & \mathbf{F}_{v\rho}T_2 & \frac{1}{2}\mathbf{F}_{v\rho}\mathbf{F}_{\rho g}T_2^2 & \mathbf{F}_{va}T_2 \\ \mathbf{0} & \mathbf{0} & \mathbf{I} & \mathbf{F}_{\rho g}T_2 & \mathbf{0} \\ \mathbf{0} & \mathbf{0} & \mathbf{0} & \mathbf{I} & \mathbf{0} \\ \mathbf{0} & \mathbf{0} & \mathbf{0} & \mathbf{0} & \mathbf{I} \end{bmatrix}. \tag{4}$$

with $\mathbf{F}_{\rho g} = \mathbf{F}_{va} = \mathbf{R}_{b2t}$, and $\mathbf{F}_{pv}$, $\mathbf{F}_{v\rho}$ as defined in Section B.2.

Using the properties of state transition matrices,

$$\mathbf{\Phi}_{(t_n,kT_{gps})} = \mathbf{\Phi}_{(t_n,t_{n-1})}\mathbf{\Phi}_{(t_{n-1},kT_{gps})} \tag{5}$$

where $\mathbf{\Phi}_{(t_n,t_{n-1})}$ is defined in eqn. (4) with $\mathbf{F}_{v\rho}$, $\mathbf{F}_{\rho g}$ and $\mathbf{F}_{va}$ being the values averaged over the time interval $[t_n, t_{n-1})$ and $\mathbf{\Phi}_{(t_{n-1},kT_{gps})}$ calculated from previous iterations by eqn. (4) and eqn. (5). The calculation of eqn. (5) is initialized with $\mathbf{\Phi}_{(kT_{gps},kT_{gps})} = \mathbf{I}$ and iterated over the interval of time propagation to yield $\mathbf{\Phi}_{((k+1)T_{gps},kT_{gps})}$. At $t = (k+1)T_{gps}$, the state error covariance is propagated by eqn. (3).

The discrete time process noise covariance for the $[kT_{gps}, (k+1)T_{gps})$ interval is defined by

$$\mathbf{Q_d}_k = \int_{kT_{gps}}^{(k+1)T_{gps}} \mathbf{\Phi}_{((k+1)T_{gps},t)}\mathbf{Q}_{(t)}\mathbf{\Phi}^T_{((k+1)T_{gps},t)}dt \tag{6}$$

where $\mathbf{Q}_{(t)}$ is the continuous time process noise covariance matrix. This integral can be approximated as

$$\mathbf{Q_d}_k = \sum_1^N \mathbf{\Phi}_{(t_{i+1},t_i)}\mathbf{Q}_{(t_i)}\mathbf{\Phi}^T_{(t_{i+1},t_i)}dT_i \tag{7}$$

where $t_1 = kT_{gps}$, $t_N = (k+1)T_{gps}$, $dT_i = t_{i+1} - t_i$ and $\sum_1^N dT_i = T_{gps}$. For the present implementation, $dT_i = 0.067$s and

$$\mathbf{Q}(t) = \begin{bmatrix} \mathbf{Q}_p & \mathbf{0} & \mathbf{0} & \mathbf{0} & \mathbf{0} \\ \mathbf{0} & \mathbf{Q}_v & \mathbf{0} & \mathbf{0} & \mathbf{0} \\ \mathbf{0} & \mathbf{0} & \mathbf{Q}_g & \mathbf{0} & \mathbf{0} \\ \mathbf{0} & \mathbf{0} & \mathbf{0} & \mathbf{Q}_{gd} & \mathbf{0} \\ \mathbf{0} & \mathbf{0} & \mathbf{0} & \mathbf{0} & \mathbf{Q}_{ad} \end{bmatrix} \tag{8}$$

with

$$\begin{aligned} \mathbf{Q}_p &= diag(\sigma_p^2, \sigma_p^2, \sigma_p^2,), \\ \mathbf{Q}_v &= \mathbf{R}_{b2t}\Sigma_v^2\mathbf{R}_{b2t}^T, \\ \mathbf{Q}_g &= \mathbf{R}_{b2t}\Sigma_g^2\mathbf{R}_{b2t}^T, \\ \mathbf{Q}_{gd} &= diag(\sigma_{qd}^2, \sigma_{qd}^2, \sigma_{qd}^2), \\ \mathbf{Q}_{ad} &= diag(\sigma_{ad}^2, \sigma_{ad}^2, \sigma_{ad}^2). \end{aligned}$$

In above,

$$\begin{aligned} \sigma_p &= 1 \times 10^{-5}\ m/s/\sqrt{Hz}, \\ \sigma_v &= 2.2 \times 10^{-2}\ m/s^2/\sqrt{Hz}, \\ \sigma_g &= 2.2 \times 10^{-3}\ rad/s/\sqrt{Hz}, \\ \sigma_{qd} &= 2.2 \times 10^{-5}\ (rad/s/s)/\sqrt{Hz}, \\ \sigma_{ad} &= 2.0 \times 10^{-4}\ (m/s/s/s)/\sqrt{Hz}; \end{aligned}$$

and since $\Sigma_v = \sigma_v\mathbf{I}$ and $\Sigma_g = \sigma_g\mathbf{I}$ in these equations,

$$\mathbf{R}_{v2t}\Sigma_v^2\mathbf{R}_{v2t}^T = \sigma_v^2\mathbf{R}_{v2t}\mathbf{I}\mathbf{R}_{v2t}^T = \sigma_v^2\mathbf{I}, \tag{9}$$

$$\mathbf{R}_{v2t}\Sigma_g^2\mathbf{R}_{v2t}^T = \sigma_g^2\mathbf{R}_{v2t}\mathbf{I}\mathbf{R}_{v2t}^T = \sigma_g^2\mathbf{I}. \tag{10}$$

3.2 Magnetometer and GPS aided INS

There are two magnetometers on the vehicle. The front and rear magnetometers measure the front and rear off-trajectory distances, when the trajectory is defined by a trail of magnets embedded in the roadway. The INS measures the vehicle position, velocity and attitude in the tangent frame. The INS states are used to predict the magnetometer measurements. The residual between each magnetometer measurement and the INS estimate is useful for INS calibration. This section describes the theory and methodology of integrating the magnetometers with the INS for situations where the magnetometers and the INS are not co-located. The analysis of Section 4.1 shows that this approach allows full attitude determination even with a single magnetometer.

The raw measurement of a magnetometer is sensitive to two types of interference [38]: the earth magnetic field, and high frequency magnetic noise generated by the engine. In addition, if the goal is to use the magnetometer to measure horizontal distance to a magnet, then the change in magnetometer reading due to vertical motion of the vehicle would be considered as error. The PATH magnetometer system compensates each of these three error sources [38].

In field tests of the PATH magnetometer application, a series of 2.5 cm diameter and 10 cm long ceramic magnetic bars were buried vertically in the test track. Each magnetic bar provides a 20 cm to 50 cm radius M-field. Tests and experiences show that the PATH magnetometer is able to reliably read the vehicle deviation independent of variations in the height. The accuracy of the measurements is high (< 2 cm) and its latency is low (2-6 ms) due to fast data processing. No problems were encountered in tests at speeds up to 135 km/h (85 MPH).

The following sections present the equations that the INS will use to predict the magnetometer measurements and that the EKF will use to estimate the INS calibration errors.

3.2.1 Magnetometer off-trajectory distance model

Figure 3 shows the geometry and defines terms necessary for the derivation of the model of the magnetometer measurement of the off-trajectory distance. Since the PATH magnetometer is designed to be relatively independent of variations in the height the measurement model is only affected by horizontal position errors. Let $\mathbf{P_m}(x_m, y_m)$ and $\mathbf{P_T}(x_t, y_t)$ denote the true magnetometer position and the position of the corresponding nearest point on the trajectory. Let $\hat{\mathbf{P}}_\mathbf{m}(\hat{x}_m, \hat{y}_m)$ and $\mathbf{P}_\lambda(x_\lambda, y_\lambda)$ denote the INS calculation of the magnetometer position and the position of the corresponding nearest point on the trajectory. $\mathbf{H_m}$ is the unit vector pointing from $\mathbf{P_T}(x_t, y_t)$ to $\mathbf{P_m}(x_m, y_m)$, which is normal to the trajectory. Due to $||\hat{\mathbf{P}}_\mathbf{m} - \mathbf{P_m}||$ being small, the segment $(\mathbf{P}_\lambda - \mathbf{P_T})$ is tangent to the trajectory, and the vector $(\hat{\mathbf{P}}_\mathbf{m} - \mathbf{P}_\lambda)$ is parallel to $\mathbf{H_m}$. $\mathbf{V}$ is the unit vector pointing from $\mathbf{P_T}(x_t, y_t)$ to $\mathbf{P}_\lambda(x_\lambda, y_\lambda)$, which is tangent to the trajectory. Hence, $\mathbf{H_m}$ and $\mathbf{V}$ are orthogonal.

The magnetometer off-trajectory distance calculated by an INS collocated with the magnetometer is

$$\begin{aligned}
\hat{d} &= ||\hat{\mathbf{P}}_\mathbf{m} - \mathbf{P}_\lambda|| && (11)\\
&= \mathbf{H_m}(\hat{\mathbf{P}}_\mathbf{m} - \mathbf{P}_\lambda)\\
&= \mathbf{H_m}(\hat{\mathbf{P}}_\mathbf{m} - \mathbf{P_m}) + \mathbf{H_m}(\mathbf{P_m} - \mathbf{P_T}) + \mathbf{H_m}(\mathbf{P_T} - \mathbf{P}_\lambda)\\
&= \mathbf{H_m}(\hat{\mathbf{P}}_\mathbf{m} - \mathbf{P_m}) + \mathbf{H_m}(\mathbf{P_m} - \mathbf{P_T})\\
&= \mathbf{H_m}(\hat{\mathbf{P}}_\mathbf{m} - \mathbf{P_m}) + ||\mathbf{P_m} - \mathbf{P_T}|| && (12)
\end{aligned}$$

with $\mathbf{H_m}(\mathbf{P_T} - \mathbf{P}_\lambda) \propto -\mathbf{H_m}\mathbf{V} = \mathbf{0}$ due to $\mathbf{H_m}$ and $\mathbf{V}$ being orthogonal. The magnetometer measured off-trajectory distance is

$$\tilde{d} = ||\mathbf{P_m} - \mathbf{P_T}|| + n \qquad (13)$$

with n being the measurement noise. Therefore, the residual measurement equation is

$$\begin{aligned}
\delta d &= \tilde{d} - \hat{d} && (14)\\
&= \mathbf{H_m}(\mathbf{P_m} - \hat{\mathbf{P}}_\mathbf{m}) + n\\
&= \mathbf{H_m}\begin{bmatrix} \delta x_m \\ \delta y_m \end{bmatrix} + n && (15)
\end{aligned}$$

with

$$\mathbf{H_m} = \left[\frac{(x_m - x_t)}{\sqrt{(x_m - x_t)^2 + (y_m - y_t)^2}} \quad \frac{(y_m - y_t)}{\sqrt{(x_m - x_t)^2 + (y_m - y_t)^2}} \right]_{\mathbf{P_m}(x_m, y_m) \approx \hat{\mathbf{P}}_\mathbf{m}(\hat{x}_m, \hat{y}_m)}. \qquad (16)$$

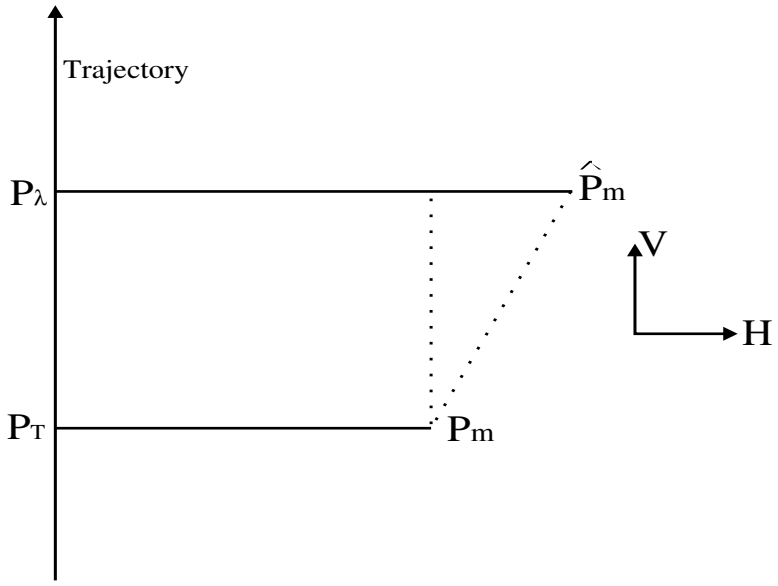

Figure 3: Geometry of the magnetometer off-trajectory calculation. $\mathbf{P_m}$ denotes the true magnetometer location. $\hat{\mathbf{P}}_\mathbf{m}$ is the magnetometer position calculated by the INS. $\mathbf{P_T}$ and $\mathbf{P}_\lambda$ are the nearest points to $\mathbf{P_m}$ and $\hat{\mathbf{P}}_\mathbf{m}$ on the trajectory. $\mathbf{H}$ and $\mathbf{V}$ are the normal and tangent to the trajectory at $\mathbf{P_T}$.

This analysis shows that the residual magnetometer measurement contains information useful for correcting the position estimate in the direction normal to the trajectory. This is extremely desirable since it allows an integrated magnetometer/GPS/INS approach to overcome a difficulty of the magnetometer approach as well as a difficulty of the GPS/INS approach. In the situations where some GPS signals are blocked, the blocked signals are usually those from satellites in the direction lateral to the trajectory (i.e., $\mathbf{H_m}$). This is true for example in *urban canyons* formed by trees or buildings. In such situations, GPS can calibrate the INS error tangent to the trajectory (i.e., arc length), but not the INS error lateral to the trajectory. The magnetometer has the reverse characteristics. The above analysis shows that when lateral GPS signals are blocked, the magnetometer and GPS calibrate complementary portions of the INS error.

Note that knowledge of the magnet locations is not required for implementation. The INS predicts the magnetometer off trajectory distance using eqn. (11). This calculation is identical to the control state calculation of d described in Appendix C. As long as the magnetometer system supplies a time tagged measurement, the INS can calculate the magnetometer off trajectory distance without knowledge of the magnet location.

3.2.2 On-vehicle magnetometer configuration

The GPS/INS and magnetometer configuration is shown in Figure 4. There are two magnetometers on the vehicle. One on the front and one on the rear bumbers. The light lines are the outline of a box enclosing the vehicle chassis and the wide dotted lines indicate the offsets from $\mathbf{G}$ to $\mathbf{S_f}$ and $\mathbf{S_r}$ in body frame. In the body frame, $\mathbf{G}$ denotes the GPS/INS effective position, $\mathbf{S_f}$ denotes the front magnetometer position and $\mathbf{S_r}$ denotes the rear magnetometer position. In the body frame, the sensor offset vectors are

$$[\mathbf{S_f} - \mathbf{G}]^b = \begin{bmatrix} l_f \\ -d \\ h \end{bmatrix} \qquad [\mathbf{S_r} - \mathbf{G}]^b = \begin{bmatrix} -l_r \\ -d \\ h \end{bmatrix} \tag{17}$$

where l_f is the distance between $\mathbf{G}$ and $\mathbf{S_f}$ along the $x-axis$ of the body frame, l_r is distance between $\mathbf{G}$ and $\mathbf{S_r}$ along the $x-axis$ of the body frame, d is the distance between $\mathbf{G}$ and either magnetometer along the $y-axis$ of the body frame, and h being the distance between $\mathbf{G}$ and either magnetometer ($\mathbf{S_f}$ or $\mathbf{S_r}$) along the $z-axis$ of the body frame. We have assumed that the vector from $\mathbf{S_f}$ to $\mathbf{S_r}$ is parallel to the $x-axis$ of the vehicle body frame. This assumption is not necessary for the theory of the approach to work. It is (approximately) true in this application of the approach.

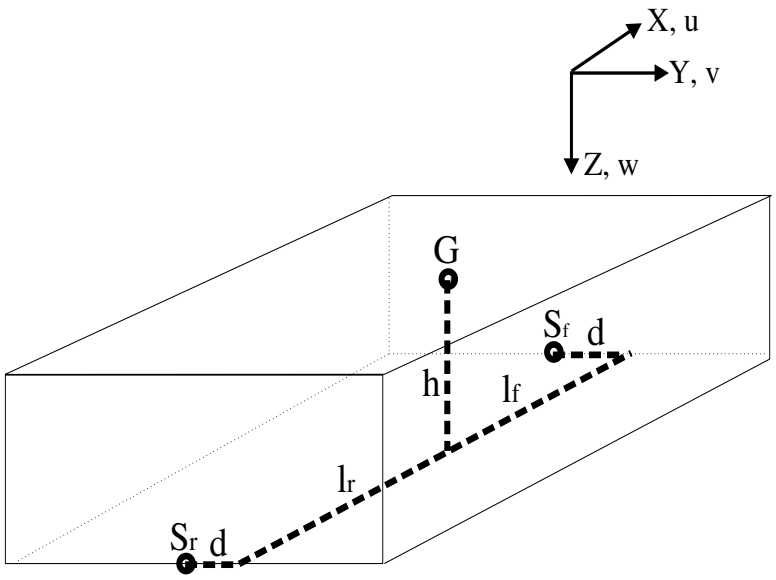

Figure 4: Configuration of the magnetometers and INS on the vehicle chassis. The light lines are the outline of a box enclosing the vehicle chassis. The INS effective position is indicated by G. The front and rear magnetometer positions are indicated by S_f and S_r, respectively. The wide dotted lines indicated the offsets from G to S_f and S_r in body frame.

Denoting the tangent frame coordinates of the GPS/INS, the front magnetometer and the rear magnetometer as $\mathbf{G} = (x, y, z)$, $\mathbf{S_f} = (x_f, y_f, z_f)$ and $\mathbf{S_r} = (x_r, y_r, z_r)$, respectively, yields the following equations:

$$\begin{bmatrix} x_f \\ y_f \\ z_f \end{bmatrix} = \begin{bmatrix} x \\ y \\ z \end{bmatrix} + \mathbf{R}_{b2t} \begin{bmatrix} l_f \\ -d \\ h \end{bmatrix} \tag{18}$$

$$\begin{bmatrix} x_r \\ y_r \\ z_r \end{bmatrix} = \begin{bmatrix} x \\ y \\ z \end{bmatrix} + \mathbf{R}_{b2t} \begin{bmatrix} -l_r \\ -d \\ h \end{bmatrix} \tag{19}$$

with $\mathbf{R}_{b2t}$ being the rotation matrix from the vehicle body frame to the tangent frame. The INS uses these equations to predict the tangent plane positions of each magnetometer. With $\hat{\mathbf{G}} = (\hat{x}, \hat{y}, \hat{z})$, $\hat{\mathbf{S}}_\mathbf{f} = (\hat{x}_f, \hat{y}_f, \hat{z}_f)$ and $\hat{\mathbf{S}}_\mathbf{r} = (\hat{x}_r, \hat{y}_r, \hat{z}_r)$, the equations are

$$\begin{bmatrix} \hat{x}_f \\ \hat{y}_f \\ \hat{z}_f \end{bmatrix} = \begin{bmatrix} \hat{x} \\ \hat{y} \\ \hat{z} \end{bmatrix} + \hat{\mathbf{R}}_{b2t} \begin{bmatrix} l_f \\ -d \\ h \end{bmatrix}, \tag{20}$$

$$\begin{bmatrix} \hat{x}_r \\ \hat{y}_r \\ \hat{z}_r \end{bmatrix} = \begin{bmatrix} \hat{x} \\ \hat{y} \\ \hat{z} \end{bmatrix} + \hat{\mathbf{R}}_{b2t} \begin{bmatrix} -l_r \\ -d \\ h \end{bmatrix} \tag{21}$$

where $\hat{\mathbf{R}}_{b2t}$ is the INS estimate of $\mathbf{R}_{b2t}$. These matrices are related by

$$\hat{\mathbf{R}}_{\mathbf{b2t}} = (\mathbf{I} - [\rho\times])\mathbf{R}_{\mathbf{b2t}} + h.o.t.'s \tag{22}$$

with $[\rho\times]$ being the skew-symmetric matrix formed by the small rotation angle error vector $\rho = [\epsilon_N, \epsilon_E, \epsilon_D]^T$,

$$[\rho\times] = \begin{bmatrix} 0 & -\epsilon_D & \epsilon_E \\ \epsilon_D & 0 & -\epsilon_N \\ -\epsilon_E & \epsilon_N & 0 \end{bmatrix}. \tag{23}$$

The matrix $[\rho\times]$ is the correction that is required to align the calculated tangent frame to the true tangent frame. One of our objectives is to estimate ρ.

Subtracting eqn. (20) from eqn. (18) and eqn. (21) from eqn. (19), substituting in eqn. (22), and rearranging yields

$$\begin{bmatrix} \delta x_f \\ \delta y_f \\ \delta z_f \end{bmatrix} = \begin{bmatrix} \delta x \\ \delta y \\ \delta z \end{bmatrix} + [\rho\times]\,\hat{\mathbf{R}}_{b2t} \begin{bmatrix} l_f \\ -d \\ h \end{bmatrix} + \begin{bmatrix} n_{x_f} \\ n_{y_f} \\ n_{z_f} \end{bmatrix} \tag{24}$$

$$\begin{bmatrix} \delta x_r \\ \delta y_r \\ \delta z_r \end{bmatrix} = \begin{bmatrix} \delta x \\ \delta y \\ \delta z \end{bmatrix} + [\rho\times]\,\hat{\mathbf{R}}_{b2t} \begin{bmatrix} -l_r \\ -d \\ h \end{bmatrix} + \begin{bmatrix} n_{x_r} \\ n_{y_r} \\ n_{z_r} \end{bmatrix} \tag{25}$$

where $\delta\xi = \xi - \hat{\xi}$ denotes the error between actual and calculated quantities and n_ξ is the error due to linearization. Define

$$\begin{bmatrix} \Delta\hat{x}_f^t \\ \Delta\hat{y}_f^t \\ \Delta\hat{z}_f^t \end{bmatrix} = \hat{\mathbf{R}}_{b2t} \begin{bmatrix} l_f \\ -d \\ h \end{bmatrix}$$

and

$$\begin{bmatrix} \Delta\hat{x}_r^t \\ \Delta\hat{y}_r^t \\ \Delta\hat{z}_r^t \end{bmatrix} = \hat{\mathbf{R}}_{b2t} \begin{bmatrix} -l_r \\ -d \\ h \end{bmatrix}.$$

Note that these vectors can be calculated online by the INS. The linearized equations relating the INS errors to the error in the calculated magnetometer positions are then

$$\begin{bmatrix} \delta x_f \\ \delta y_f \\ \delta z_f \end{bmatrix} = \begin{bmatrix} \delta x \\ \delta y \\ \delta z \end{bmatrix} - \begin{bmatrix} 0 & -\Delta\hat{z}_f^t & \Delta\hat{y}_f^t \\ \Delta\hat{z}_f^t & 0 & -\Delta\hat{x}_f^t \\ -\Delta\hat{y}_f^t & \Delta\hat{x}_f^t & 0 \end{bmatrix} \begin{bmatrix} \epsilon_N \\ \epsilon_E \\ \epsilon_D \end{bmatrix} + \begin{bmatrix} n_{x_f} \\ n_{y_f} \\ n_{z_f} \end{bmatrix}, \text{ and} \tag{26}$$

$$\begin{bmatrix} \delta x_r \\ \delta y_r \\ \delta z_r \end{bmatrix} = \begin{bmatrix} \delta x \\ \delta y \\ \delta z \end{bmatrix} - \begin{bmatrix} 0 & -\Delta\hat{z}_r^t & \Delta\hat{y}_r^t \\ \Delta\hat{z}_r^t & 0 & -\Delta\hat{x}_r^t \\ -\Delta\hat{y}_r^t & \Delta\hat{x}_r^t & 0 \end{bmatrix} \begin{bmatrix} \epsilon_N \\ \epsilon_E \\ \epsilon_D \end{bmatrix} + \begin{bmatrix} n_{x_r} \\ n_{y_r} \\ n_{z_r} \end{bmatrix}. \tag{27}$$

The following subsection extends this analysis to relate the INS state error to the residual magnetometer measurement error.

3.2.3 Magnetometer measurement and its linearized equation

Let $\mathbf{P_{t_f}}(x_{t_f}, y_{t_f})$ be the nearest point to $\mathbf{S_f}$ on the trajectory. Let $\mathbf{P_{t_r}}(x_{t_r}, y_{t_r})$ be the nearest point to $\mathbf{S_r}$ on the trajectory. The off-trajectory distance measurements of the front and rear magnetometers are

$$\tilde{d}_f = \sqrt{(x_f - x_{t_f})^2 + (y_f - y_{t_f})^2} + n_f{}' \tag{28}$$

$$\tilde{d}_r = \sqrt{(x_r - x_{t_r})^2 + (y_r - y_{t_r})^2} + n_r{}' \tag{29}$$

where $n_f{}'$ and $n_r{}'$ denote the front measurement noise and the rear measurement noise, respectively. Linearizing eqns. (28) – (29) at $\hat{\mathbf{S}}_\mathbf{f} = (\hat{x}_f, \hat{y}_f, \hat{z}_f)$ and $\hat{\mathbf{S}}_\mathbf{r} = (\hat{x}_r, \hat{y}_r, \hat{z}_r)$, following the approach of Section 3.2.1, yields the following linear equations:

$$\begin{aligned} \delta d_f &= \tilde{d}_f - \hat{d}_f \\ &= \mathbf{H_f} \begin{bmatrix} \delta x_f \\ \delta y_f \end{bmatrix} + h.o.t.'s + n_f{}' \end{aligned} \tag{30}$$

$$\begin{aligned} \delta d_r &= \tilde{d}_r - \hat{d}_r \\ &= \mathbf{H_r} \begin{bmatrix} \delta x_r \\ \delta y_r \end{bmatrix} + h.o.t.'s + n_r{}' \end{aligned} \tag{31}$$

where $h.o.t.'s$ represents the higher order terms in the expansion,

$$\mathbf{H_f} = \left[\frac{(x_f - x_{t_f})}{\sqrt{(x_f - x_{t_f})^2 + (y_f - y_{t_f})^2}} \quad \frac{(y_f - y_{t_f})}{\sqrt{(x_f - x_{t_f})^2 + (y_f - y_{t_f})^2}} \right]_{(x_f, y_f) = (\hat{x}_f, \hat{y}_f)}$$

and

$$\mathbf{H_r} = \left[\begin{array}{cc} \frac{(x_r - x_{t_r})}{\sqrt{(x_r-x_{t_r})^2+(y_r-y_{t_r})^2}} & \frac{(y_r - y_{t_r})}{\sqrt{(x_r-x_{t_r})^2+(y_r-y_{t_r})^2}} \end{array} \right]_{(x_r,y_r)=(\hat{x}_r,\hat{y}_r)}.$$

For highway trajectories, the curvature is small ($< \frac{1}{800} m^{-1}$). Therefore, since $||\mathbf{S_r} - \mathbf{S_r}|| << 800m$,

$$\mathbf{H_f} = \mathbf{H_r} = \mathbf{H_m} \tag{32}$$

with $\mathbf{H_m}$ being the unit vector normal to the trajectory defined in Section 3.2.1.

In this implementation, the calculated values of d_f and d_r are needed at a time synchronized with the magnetometer measurements. Note that these quantities can be calculated without explicit knowledge of the location of the magnets. A method for calculating $\hat{d}_G$, the distance of the INS from the trajectory, is described in [35]. The calculation described in [35] also produces the normal to the trajectory, so that $\hat{\mathbf{H}}_\mathbf{m}$ is available. Therefore, the calculated front and rear magnetometer off-trajectory distances ($\hat{d}_f$ and $\hat{d}_r$) are

$$\hat{d}_f = \hat{\mathbf{H}}_\mathbf{m} \left[\begin{array}{c} \hat{x}_f - \hat{x} \\ \hat{y}_f - \hat{y} \end{array} \right] + \hat{d}_G, \tag{33}$$

$$\hat{d}_r = \hat{\mathbf{H}}_\mathbf{m} \left[\begin{array}{c} \hat{x}_r - \hat{x} \\ \hat{y}_r - \hat{y} \end{array} \right] + \hat{d}_G \tag{34}$$

where the terms $[\hat{x}_f - \hat{x}, \hat{y}_f - \hat{y}]$ and $[\hat{x}_r - \hat{x}, \hat{y}_r - \hat{y}]$ are calculated as shown in eqns. (20–21).

3.2.4 Measurement matrix definition

Substituting δx_f and δy_f of eqn. (26) into eqn. (30) and δx_r and δy_r of eqn. (27) into eqn. (31), and rearranging yields the following equations:

$$\delta d_f = \mathbf{H_f} \left[\begin{array}{ccccc} 1 & 0 & 0 & \Delta\hat{z}_f^t & -\Delta\hat{y}_f^t \\ 0 & 1 & -\Delta\hat{z}_f^t & 0 & \Delta\hat{x}_f^t \end{array} \right] \left[\begin{array}{c} \delta x \\ \delta y \\ \epsilon_N \\ \epsilon_E \\ \epsilon_D \end{array} \right] + n_f \tag{35}$$

$$\delta d_r = \mathbf{H_r} \left[\begin{array}{ccccc} 1 & 0 & 0 & \Delta\hat{z}_r^t & -\Delta\hat{y}_r^t \\ 0 & 1 & -\Delta\hat{z}_r^t & 0 & \Delta\hat{x}_r^t \end{array} \right] \left[\begin{array}{c} \delta x \\ \delta y \\ \epsilon_N \\ \epsilon_E \\ \epsilon_D \end{array} \right] + n_r \tag{36}$$

where n_f and n_r represent the front and rear magnetometer measurement noise and linearization error terms. Combining eqn. (35) and eqn. (36) provides the desired measurement equation as

$$\left[\begin{array}{c} \delta d_f \\ \delta d_r \end{array} \right] = \mathbf{H}_{fr_m} \left[\begin{array}{c} \delta x \\ \delta y \\ \epsilon_N \\ \epsilon_E \\ \epsilon_D \end{array} \right] + \left[\begin{array}{c} n_f \\ n_r \end{array} \right]. \tag{37}$$

The measurement matrix, $\mathbf{H}_{fr_m}$, is

$$\begin{aligned} \mathbf{H}_{fr_m} &= \left[\begin{array}{ccccc} h_{p_{N_f}} & h_{p_{E_f}} & h_{\rho_{N_f}} & h_{\rho_{E_f}} & h_{\rho_{D_f}} \\ h_{p_{N_r}} & h_{p_{E_r}} & h_{\rho_{N_r}} & h_{\rho_{E_r}} & h_{\rho_{D_r}} \end{array} \right] \\ &= \left[\begin{array}{cc} \mathbf{H_m} & 0 \\ 0 & \mathbf{H_m} \end{array} \right] \left[\begin{array}{ccccc} 1 & 0 & 0 & \Delta\hat{z}_f^t & -\Delta\hat{y}_f^t \\ 0 & 1 & -\Delta\hat{z}_f^t & 0 & \Delta\hat{x}_f^t \\ 1 & 0 & 0 & \Delta\hat{z}_r^t & -\Delta\hat{y}_r^t \\ 0 & 1 & -\Delta\hat{z}_r^t & 0 & \Delta\hat{x}_r^t \end{array} \right] \end{aligned} \tag{38}$$

with $\mathbf{H_m} \in \Re^{1\times 2}$ and $\mathbf{H}_{fr_m} \in \Re^{1\times 5}$. This linearized measurement equation is used in the extended Kalman filter to estimate the INS errors.

3.2.5 Linearized Measurement Equations

The DCPGPS residual model is presented in eqn. (88) in the ECEF frame. It can be rewritten in the tangent frame as

$$\delta\phi = (\nabla\Delta\phi + N)\lambda - \hat{R} \quad = \quad \mathbf{h}^{(ij)}\mathbf{R}_{t2e}\delta\mathbf{p} + n_\phi \tag{39}$$

where $(\nabla\Delta\phi + N)\lambda$ is the ambiguity-resolved double difference GPS phase range. The operation $\mathbf{H_1}$ of Figure 1 is

$$\hat{R} \quad = \quad \|\mathbf{X} - (\mathbf{X}_0 + \mathbf{R}_{t2e}\mathbf{p})\| \tag{40}$$

where $\mathbf{X}$ is the satellite position in the ECEF frame, $\mathbf{X_0}$ is the base station GPS antenna position in the ECEF frame, and $\mathbf{p}$ is the INS position in the tangent frame. Therefore,

$$\begin{aligned} \mathbf{h}_p &= [\ h_{p_N} \quad h_{p_E} \quad h_{p_D}\ ] \\ &= \mathbf{h}^{(ij)}\mathbf{R}_{t2e} \end{aligned} \tag{41}$$

is the definition of the linearized range measurement vector relating the phase residual to the position residual state, the double difference GPS line-of-sight vector, and the double differential phase noise n_ϕ.

Projecting the tangent frame INS velocity onto the double difference Doppler measurement, subtracting it from eqn. (89) and rewriting in the tangent frame yields

$$\delta D = \nabla\Delta D\lambda - \hat{D} \quad = \quad \mathbf{h}^{(ij)}\mathbf{R}_{t2e}\delta\mathbf{v} + n_D \tag{42}$$

where $\nabla\Delta D\lambda$ is double differential GPS Doppler measurement. The operation corresponding to $\mathbf{H_2}$ of Figure 1 is

$$\hat{D} \quad = \quad \mathbf{h}^{(ij)}\mathbf{R}_{t2e}\mathbf{v} \tag{43}$$

where $\mathbf{v}$ is the INS velocity in the tangent frame. Therefore,

$$\begin{aligned} \mathbf{h}_v &= [\ h_{v_N} \quad h_{v_E} \quad h_{v_D}\ ] \\ &= \mathbf{h}^{(ij)}\mathbf{R}_{t2e} \end{aligned} \tag{44}$$

is the Doppler measurement vector relating the residual Doppler measurement to the velocity residual states and the double differential Doppler measurement noise n_D.

The magnetometer measurement residual model is defined in eqn. (37) with $\mathbf{H}_{fr_m}$ defined in eqn. (38). The off-trajectory distance calculations corresponding to $\mathbf{H_3}$ in Figure 1 is defined in Eqns. (33 – 34).

Combining the measurement models from the GPS carrier phase, Doppler, and magnetometer measurement residuals yields

$$\begin{bmatrix} \delta\phi \\ \delta D \\ \delta d_f \\ \delta d_r \end{bmatrix} \quad = \quad \mathbf{H}\delta\mathbf{x} + \begin{bmatrix} n_\phi \\ n_D \\ n_f \\ n_r \end{bmatrix} \tag{45}$$

where

$$\mathbf{H} = \begin{bmatrix} h_{p_N} & h_{p_E} & h_{p_D} & 0 & 0 & 0 & 0 & 0 & 0 & 0 & 0 & 0 & 0 & 0 & 0 \\ 0 & 0 & 0 & h_{v_N} & h_{v_E} & h_{v_D} & 0 & 0 & 0 & 0 & 0 & 0 & 0 & 0 & 0 \\ h_{p_{N_f}} & h_{p_{E_f}} & 0 & 0 & 0 & 0 & h_{\rho_{N_f}} & h_{\rho_{E_f}} & h_{\rho_{D_f}} & 0 & 0 & 0 & 0 & 0 & 0 \\ h_{p_{N_r}} & h_{p_{E_r}} & 0 & 0 & 0 & 0 & h_{\rho_{N_r}} & h_{\rho_{E_r}} & h_{\rho_{D_r}} & 0 & 0 & 0 & 0 & 0 & 0 \end{bmatrix}. \tag{46}$$

3.3 Two Antenna GPS aided INS

The following sections present the equations that the INS will use to predict the two antennae DCPGPS measurements and that the EKF will use to estimate the INS calibration errors. The two GPS antennae are rigidly attached to the vehicle body at known locations offset in the horizontal plane.

Eqn. (85) and eqn. (88) give the relationship between the GPS receiver differential measurement and position residual error $\Delta\mathbf{x}$ in ECEF frame. Note that the linearization point is the INS state saved synchronously with the GPS measurement. Therefore, $\Delta\mathbf{x}$ is the estimated correction to the INS state in the ECEF frame. The equation $\Delta\mathbf{x} = \mathbf{R_{t2e}}\Delta\mathbf{x}^t$ gives the relationship between the position residual error in ECEF frame and the position residual error $\Delta\mathbf{x}^t$ in the tangent frame.

3.3.1 Linearized INS residual model

Let $\mathbf{A_1^t}$, $\mathbf{A_2^t}$ and $\mathbf{G^t}$ denote the true position coordinates of GPS antenna 1, GPS antenna 2 and INS in the tangent frame, respectively. Let $\hat{\mathbf{A}}_\mathbf{1}^\mathbf{t}$, $\hat{\mathbf{A}}_\mathbf{2}^\mathbf{t}$ and $\hat{\mathbf{G}}^\mathbf{t}$ denote the position coordinates of GPS antenna 1, GPS antenna 2 and INS in the tangent frame, respectively, as calculated by the INS at the GPS measurement time. Let $\mathbf{A_1^b}$ and $\mathbf{A_2^b}$ denote the coordinates of GPS antenna 1 and GPS antenna 2 in the body frame, which are known. Hence, the true positions of GPS antennae in the tangent frame are:

$$\mathbf{A_1^t} = \mathbf{G^t} + \mathbf{R_{b2t}}\mathbf{A_1^b} \tag{47}$$

$$\mathbf{A_2^t} = \mathbf{G^t} + \mathbf{R_{b2t}}\mathbf{A_2^b} \tag{48}$$

and the predicted positions of GPS antennae, based on the calculated INS states, are

$$\hat{\mathbf{A}}_\mathbf{1}^\mathbf{t} = \hat{\mathbf{G}}^\mathbf{t} + \hat{\mathbf{R}}_\mathbf{b2t}\mathbf{A_1^b} \tag{49}$$

$$\hat{\mathbf{A}}_\mathbf{2}^\mathbf{t} = \hat{\mathbf{G}}^\mathbf{t} + \hat{\mathbf{R}}_\mathbf{b2t}\mathbf{A_2^b} \tag{50}$$

since $\mathbf{G}^b$ is the origin of the body frame coordinate system.

Subtracting eqn. (49) from eqn. (47) and eqn. (50) from eqn. (48), yields

$$\begin{aligned} \mathbf{\Delta x_1^t} &= \mathbf{\Delta x_G^t} + [\rho\times]\hat{\mathbf{R}}_\mathbf{b2t}\mathbf{A_1^b} + \mathbf{n_1} \\ &= \mathbf{\Delta x_G^t} + [\rho\times]\hat{\mathbf{A}}_\mathbf{1}^\mathbf{t} + \mathbf{n_1} \end{aligned} \tag{51}$$

$$\begin{aligned} \mathbf{\Delta x_2^t} &= \mathbf{\Delta x_G^t} + [\rho\times]\hat{\mathbf{R}}_\mathbf{b2t}\mathbf{A_2^b} + \mathbf{n_2} \\ &= \mathbf{\Delta x_G^t} + [\rho\times]\hat{\mathbf{A}}_\mathbf{2}^\mathbf{t} + \mathbf{n_2} \end{aligned} \tag{52}$$

where $\hat{\mathbf{R}}_{b2t}$ is the INS estimate of $\mathbf{R}_{b2t}$. These matrices are related by

$$\hat{\mathbf{R}}_\mathbf{b2t} = (\mathbf{I} - [\rho\times])\mathbf{R_{b2t}} + h.o.t.'s \tag{53}$$

where $\mathbf{\Delta x_1^t} = \mathbf{A_1^t} - \hat{\mathbf{A}}_\mathbf{1}^\mathbf{t}$, $\mathbf{\Delta x_2^t} = \mathbf{A_2^t} - \hat{\mathbf{A}}_\mathbf{2}^\mathbf{t}$, $\mathbf{\Delta x_G^t} = \mathbf{G^t} - \hat{\mathbf{G}}^\mathbf{t}$, $\mathbf{n_1}$ is the GPS antenna 1 linearization error vector, and $\mathbf{n_2}$ is the GPS antenna 2 linearization error vector, and $[\rho\times]$ is the skew-symmetric rotation matrix formed by the small angle error $\rho = [\epsilon_N, \epsilon_E, \epsilon_D]^T$:

$$[\rho\times] = \begin{bmatrix} 0 & -\epsilon_D & \epsilon_E \\ \epsilon_D & 0 & -\epsilon_N \\ -\epsilon_E & \epsilon_N & 0 \end{bmatrix}. \tag{54}$$

Eqns. (51) and (52) present the linear relationship between each GPS antenna tangent plane position error and the INS position and the small rotation angle errors. Eqns. (51) and (52) are applicable for the case where both the GPS antenna $\mathbf{A_1}$ and $\mathbf{A_2}$ positions can be accurately estimated from differential carrier phase measurements. In this case, the position accuracy can be calculated at the cm level and the attitude at the sub-degree level.

If only the short baseline between $\mathbf{A_1}$ and $\mathbf{A_2}$ is accurately estimated based on double-differenced, carrier phase measurements between the two antennae, then differencing eqns. (52) and (51) yields

$$\mathbf{\Delta x_{12}^t} = [\rho\times]\hat{\mathbf{A}}_\mathbf{12}^\mathbf{t} + \mathbf{n_{12}^{'}} \tag{55}$$

with $\mathbf{\Delta x_{12}^t} = \mathbf{A_{12}^t} - \hat{\mathbf{A}}_\mathbf{12}^\mathbf{t}$, $\mathbf{A_{12}^t} = \mathbf{A_1^t} - \mathbf{A_2^t}$ and $\hat{\mathbf{A}}_\mathbf{12}^\mathbf{t} = \hat{\mathbf{A}}_\mathbf{1}^\mathbf{t} - \hat{\mathbf{A}}_\mathbf{2}^\mathbf{t}$, which gives the linear relationship between the short baseline vector residual error and the small rotation angle error. Note that this would allow sub-degree attitude estimation.

Note that this section has only derived the linearized models of the error in the INS prediction of the GPS antennae positions. These linearized models depend on the INS position and attitude errors. This section has not related these linear models to the GPS measurements. The relation to the GPS measurements is presented in the following section.

3.3.2 Measurement matrix definition

Transforming the short baseline vector residual $\mathbf{\Delta x_{12}^t}$ of eqn. (55) from the tangent frame to the ECEF frame and rearranging it yields

$$\begin{aligned} \mathbf{\Delta x_{12}} &= \mathbf{R}_{t2e}([-\hat{\mathbf{A}}_\mathbf{12}^t\times]\rho + \mathbf{n_{A_{12}}^{'}}) \\ &= \mathbf{R}_{t2e}\begin{bmatrix} 0 & \hat{z}_{12}^t & -\hat{y}_{12}^t \\ -\hat{z}_{12}^t & 0 & \hat{x}_{12}^t \\ \hat{y}_{12}^t & -\hat{x}_{12}^t & 0 \end{bmatrix}\begin{bmatrix} \epsilon_N \\ \epsilon_E \\ \epsilon_D \end{bmatrix} + \mathbf{n_{12}^{''}} \end{aligned} \tag{56}$$

with $\mathbf{\Delta x_{12}}$ being the baseline residual error in the ECEF frame, $\mathbf{R}_{t2e}$ being the rotation transformation matrix from the tangent frame to the ECEF frame, $\hat{\mathbf{A}}^t_{\mathbf{12}} = \hat{\mathbf{R}}_{b2t} A^b_{12} = [\hat{x}^t_{12} \;\; \hat{y}^t_{12} \;\; \hat{z}^t_{12}]^T$ and $\mathbf{n''_{12}}$ being the linearized noise vector in the ECEF frame.

For each ambiguity resolved carrier phase measurement defined in eqn. (94), the scalar carrier phase measurement residual is

$$\begin{aligned} \delta A_{12} &= (\nabla\Delta\phi + N)\lambda - \hat{A}_{12} = \mathbf{h}^{(ij)}\mathbf{\Delta x_{12}} \\ &= \mathbf{h}^{(ij)}\mathbf{R}_{t2e}\begin{bmatrix} 0 & \hat{z}^t_{12} & -\hat{y}^t_{12} \\ -\hat{z}^t_{12} & 0 & \hat{x}^t_{12} \\ \hat{y}^t_{12} & -\hat{x}^t_{12} & 0 \end{bmatrix}\begin{bmatrix} \epsilon_N \\ \epsilon_E \\ \epsilon_D \end{bmatrix} + n_{12} \end{aligned} \tag{57}$$

where

$$\hat{A}_{12} = \mathbf{h}^{(ij)}\hat{\mathbf{R}}_{\mathbf{t2e}}\hat{\mathbf{R}}_{\mathbf{b2t}}\mathbf{A^b_{12}} \tag{58}$$

which is calculated based on INS rotation matrices[1], $\mathbf{h}^{(ij)}$ is the GPS satellite unit vector, $\mathbf{A^b_{12}}$ is the known baseline vector in the body frame and n_{12} is the scalar noise from both the carrier phase measurements and linearization. Hence the definition of the measurement vector for each satellite is

$$\begin{aligned} \mathbf{h}_\rho &= [\; h_{\rho_N} \quad h_{\rho_E} \quad h_{\rho_D} \;] \\ &= \mathbf{h}^{(ij)}\mathbf{R}_{t2e}\begin{bmatrix} 0 & \hat{z}^t_{12} & -\hat{y}^t_{12} \\ -\hat{z}^t_{12} & 0 & \hat{x}^t_{12} \\ \hat{y}^t_{12} & -\hat{x}^t_{12} & 0 \end{bmatrix} \end{aligned} \tag{59}$$

with h_{ρ_N}, h_{ρ_E} and h_{ρ_D} being three components of the measurement vector.

3.3.3 Linearized Measurement Equations

Three measurements are used for each satellite: integer-resolved, double-differenced, carrier phase range; Doppler; and the integer-resolved, double-differenced baseline measurement. The linear observation matrix used in the extended Kalman filter for each satellite is derived below.

The integer-resolved, double-difference phase residual model is presented in eqn. (88) in the ECEF frame. It can be rewritten in the tangent frame as

$$\delta\phi = (\nabla\Delta\phi + N)\lambda - \nabla\hat{R}^{(ij)} = \mathbf{h}^{(ij)}\mathbf{R}_{t2e}\delta\mathbf{p} + n_\phi \tag{60}$$

where $(\nabla\Delta\phi + N)\lambda$ is the ambiguity-resolved, double-differential GPS phase range, and n_ϕ is the double differential phase noise. The calculation corresponding to operation $\mathbf{H_1}$ of Figure 2 is

$$\nabla\hat{R} = \|\mathbf{X}^{(i)} - (\mathbf{X}_0 + \hat{\mathbf{R}}_{t2e}\hat{\mathbf{p}})\| - \|\mathbf{X}^{(j)} - (\mathbf{X}_0 + \hat{\mathbf{R}}_{t2e}\hat{\mathbf{p}})\| \tag{61}$$

with $\mathbf{X}$ being the satellite coordinates in the ECEF frame, $\mathbf{X_0}$ being the base station GPS antenna position in the ECEF frame, and $\mathbf{p}$ being the INS position in the tangent frame. Therefore,

$$\begin{aligned} \mathbf{h}_p &= [\; h_{p_N} \quad h_{p_E} \quad h_{p_D} \;] \\ &= \mathbf{h}^{(ij)}\mathbf{R}_{t2e} \end{aligned} \tag{62}$$

is the definition of the linearized carrier phase range measurement vector for the residual position.

Projecting the tangent frame INS velocity onto the GPS user-to-satellite unit vector, subtracting it from eqn. (89), and rewriting in the tangent frame yields

$$\delta D = \nabla\Delta D\lambda - \hat{D} = \mathbf{h}^{(ij)}\mathbf{R}_{t2e}\delta\mathbf{v} + n_D \tag{63}$$

where $\nabla\Delta D\lambda$ is double differential GPS Doppler measurement, and n_D is the double differential Doppler measurement noise. The operation corresponding to $\mathbf{H_2}$ in Figure 2 is

$$\hat{D} = \hat{\mathbf{h}}^{(ij)}\hat{\mathbf{R}}_{t2e}\hat{\mathbf{v}} \tag{64}$$

[1] Error in $\hat{\mathbf{R}}_{t2e}$ is related to the position error. The error in this rotation matrix is small (< 10 μ deg) and neglected in this analysis.

with $\mathbf{v}$ being the INS velocity in the tangent frame. Therefore,

$$\begin{aligned} \mathbf{h}_v &= \begin{bmatrix} h_{v_N} & h_{v_E} & h_{v_D} \end{bmatrix} \\ &= \mathbf{h}^{(ij)}\mathbf{R}_{t2e} \end{aligned} \tag{65}$$

is the Doppler measurement vector corresponding to the velocity residual.

The calculation corresponding to $\mathbf{H_3}$ in Figure 2 is shown in eqn. (58). The linearized measurement equation is shown in eqn. (59) for the rotation error states.

Combining the phase, Doppler, and short baseline measurement models yields

$$\begin{bmatrix} \delta\phi \\ \delta D \\ \delta A_{12} \end{bmatrix} = \mathbf{H}\delta\mathbf{x} + \begin{bmatrix} n_\phi \\ n_D \\ n_{12} \end{bmatrix} \tag{66}$$

where

$$\mathbf{H} = \begin{bmatrix} h_{p_N} & h_{p_E} & h_{p_D} & 0 & 0 & 0 & 0 & 0 & 0 & 0 & 0 & 0 & 0 & 0 & 0 \\ 0 & 0 & 0 & h_{v_N} & h_{v_E} & h_{v_D} & 0 & 0 & 0 & 0 & 0 & 0 & 0 & 0 & 0 \\ 0 & 0 & 0 & 0 & 0 & 0 & h_{\rho_N} & h_{\rho_E} & h_{\rho_D} & 0 & 0 & 0 & 0 & 0 & 0 \end{bmatrix} \tag{67}$$

with the state variables and other terms defined above.

3.4 Extended Kalman Filter

In either system described herein, the magnetometer and GPS measurements and the INS dynamics are nonlinear functions of the INS state. The extended Kalman filter is implemented in residual state space by linearizing the magnetometer and GPS measurement equations, and INS dynamics.

The INS residual states and their covariance time update are

$$\delta\mathbf{x}^-_{k+1} = \mathbf{0}, \tag{68}$$

$$\mathbf{P}^-_{k+1} = \mathbf{\Phi}_{((k+1)T_{gps},kT_{gps})}\mathbf{P}^+_k\mathbf{\Phi}^T_{((k+1)T_{gps},kT_{gps})} + \mathbf{Q_d}_k. \tag{69}$$

When the valid magnetometer or differential GPS measurements are available, the filter gains are calculated as

$$\mathbf{K} = \mathbf{P}^-_{k+1}\mathbf{H}^T_{k+1}(\mathbf{H}_{k+1}\mathbf{P}^-_{k+1}\mathbf{H}^T_{k+1} + \mathbf{R}_{k+1})^{-1} \tag{70}$$

with $\mathbf{R}$ being the measurement covariance matrix corresponding to either eqn. (45) or (67), the residual state covariance matrix and the residual state measurement updates are calculated as

$$\mathbf{P}^+_{k+1} = (\mathbf{I} - \mathbf{K}\mathbf{H}_{k+1})\mathbf{P}^-_{k+1} \tag{71}$$

$$\delta\mathbf{x}^+_{k+1} = \mathbf{K}\begin{bmatrix} \delta\phi \\ \delta D \\ \delta d_f \\ \delta d_r \end{bmatrix}_{k+1}. \tag{72}$$

The estimate $\delta\mathbf{x}^+_{k+1}$ is fed back to correct INS states, as shown in Figures 1 and 2. Therefore, the initial predicted residual state for the next time propagation is $\delta\mathbf{x}^-_{k+1} = \mathbf{0}$.

When valid differential GPS or magnetometer measurements are not available, the time update of eqns. (68 – 69) still occur, to account for the increased uncertainty of the INS state. At any epoch for which magnetometer or GPS measurements are not available, $\mathbf{K}$ is set to zero, and the measurement update still occurs. This effectively sets $\mathbf{P}^+_{k+1} = \mathbf{P}^-_{k+1}$, so that $\mathbf{P}^+_{k+1}$ is properly initialized for the next time update. In the actual implementation, the measurement updates are performed as a set of scalar measurement updates (see Sect. 4.5.1 of [10]); therefore, the previous comments of this paragraph are applied on a per measurement basis.

4 Performance Analysis

This section uses covariance analysis to predict the performance that will be attained by each of the two approaches under consideration. The covariance analysis methodology is discussed in Section 4.4.2 of [10].

4.1 Magnetometer and GPS aided INS

Covariance analysis is performed to predict the system performance. The system covariance is calculated by the recursive Kalman filter time and measurement covariance updates, of eqns. (69–71), where the measurement matrix is defined in eqn. (46). The values of $\mathbf{\Phi}$, $\mathbf{Q}_d$ and $\mathbf{R}$ are defined and calculated in Section 3.1.2.

Figure 5 shows the standard deviation, determined by covariance analysis methods, for DGPS-aided INS (top), magnetometer-aided INS (middle), and front and rear magnetometer/DGPS aided INS (bottom). The left column of figures shows the position error standard deviations (STD's). The right column of figures shows the attitude error STD's. The analysis was performed for a vehicle driving without acceleration along a south to north trajectory, so that for the left column of plots the solid line is the tangential position error, the dashed line is normal position error, and the dotted line is vertical position error. A nonaccelerating vehicle is the worst case situation for INS error observability (see Section 6.8 in [10]).

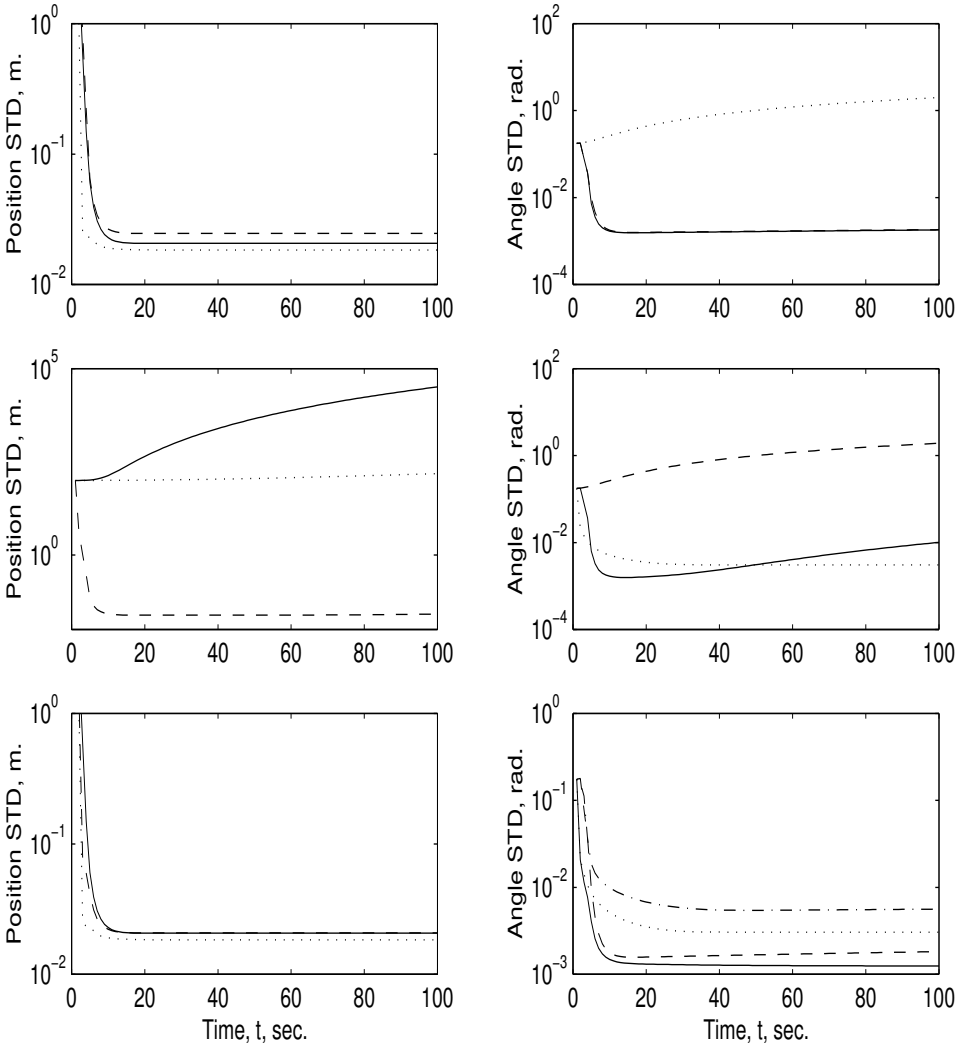

Figure 5: Covariance Analysis Comparison between DCPGPS aided INS, magnetometer aided INS, and the integrated magnetometer/DCPGPS aided INS. The left column contains plots of the position standard deviation (STD) for the three systems: dashed–normal to trajectory, solid–parallel to trajectory, dotted–vertical. The right column contains plots of the attitude STD for the three systems: dashed–pitch, solid–roll, dotted–yaw. The top two plots indicate the performance of the GPS/INS approach. The middle two plots indicate the performance of the front and rear magnetometer/INS approach. The bottom plots indicate the performance of the front and rear magnetometer/GPS/INS approach. The extra line (dashed dotted) on the graph in the third row right column displays the heading STD for the single (front) magnetometer/GPS/INS approach.

The error model for the covariance analysis includes 15 inertial error states, continuous-time white measurement noise from three accelerometers ($\sigma_a = 1 \times 10^{-2} \frac{m}{s^2\sqrt{Hz}}$) and three gyros ($\sigma_g = 2.2 \times 10^{-4} \frac{rad}{s\sqrt{Hz}}$), continuous-time white process noise for three accelerometer biases ($\sigma_a = 1 \times 10^{-6} \frac{m}{s^3\sqrt{Hz}}$) and three gyros biases ($\sigma_g = 1 \times 10^{-8} \frac{rad}{s^2\sqrt{Hz}}$), white carrier phase GPS measurement noise ($\sigma_G = 1.0\ cm$), and white magnetometer measurement noise ($\sigma_M = 1.0\ cm$). For this analysis, the magnetometer to INS offsets are $d = 0.3\ m,\ h = 1.0\ m,\ l_f = 1.0\ m,$ and $l_r = 1.0\ m$.

The position error STD plots of the left column show that DGPS-aided INS provides position estimates in all three dimensions at the 3.5 cm level. The magnetometer-aided INS accurately estimates the lateral vehicle position (2.8 cm), but is not capable of estimating vertical or longitudinal position[2]. The magnetometer/DGPS-aided INS accurately estimates position in all three dimensions at the 2.8 cm level.

The attitude error STD plots of the right column show that the DGPS-aided INS is able to accurately estimate pitch and roll ($STD \approx 0.1\ deg$), but that yaw errors (for a non-accelerating vehicle) are not observable. This lack of observability is well understood and discussed in the literature, see for example Section 6.8 of [10]. The magnetometer-aided INS is able to accurately estimate yaw ($STD = 0.18\ deg$) due to the spacing between the two magnetometers, but cannot estimate pitch or roll. The fourth line (dashed dotted) of the bottom right column shows the yaw estimation accuracy when only the front magnetometer measurement is used as an aiding signal. This front magnetometer/DGPS-aided INS achieves a yaw error STD of 0.32 $degs$. The front and rear magnetometer/DGPS-aided INS is able to accurately estimate all three attitude states. Of primary importance, yaw accuracy is predicted to have $STD = 0.18\ deg$.

4.2 Two Antenna GPS aided INS

Covariance analysis is performed to predict the system performance. The system covariance is calculated by the recursive Kalman filter time and measurement covariance updates, of eqns. (69–71), where the measurement matrix is defined in eqn. (67). The values of $\mathbf{\Phi}$, $\mathbf{Q}_d$ and $\mathbf{R}$ are defined and calculated in Section 3.1.2. For two antennae DGPS aided INS, the measurement matrix $\mathbf{H}$ is defined as eqn. (67) with $a = 1.0$ meter and $b = 0.13$ meter corresponding to Figure 10. For one antenna DGPS aided INS, the measurement matrix $\mathbf{H}$ is defined as the first two rows of eqn. (67).

Since a main interest is the accuracy of the estimated heading, we analyze the worst case scenario of a non-accelerating vehicle. The assumptions for this special situation are:

- the vehicle is driving at a constant speed without acceleration;
- the geometry of GPS is formed by four satellites with one directly above the GPS receiver and other three equally separated with 45 degree elevation angle.

Figure 6 shows the position and velocity error standard deviations for one antenna carrier phase DGPS aided INS[3] (top sub-figures) and two antenna carrier phase DGPS aided INS (bottom sub-figures). The left sub-figures are the standard deviation of position errors The right sub-figures are the standard deviation of velocity errors. The solid line represents the north error. The dashed line represents the east error. The dotted line represents the down direction error. The figure shows both the position and velocity are accurately estimated for both cases. The position errors of one antenna DGPS aided INS are within 0.026 meter when the system is in steady state, while the position errors of two antennae DGPS aided INS are within 0.021 meter. The velocity errors of one antenna DGPS aided INS are within 0.022 m/s when system is in steady state; while the velocity errors of two antennae DGPS aided INS are within 0.020 m/s.

Figure 7 shows the attitude error standard deviations for one antenna carrier phase DGPS aided INS (top figure) and two antennae carrier phase DGPS aided INS (bottom figure). In the figure, the solid line represents the roll angle error, the dashed line represents the pitch angle error, the dotted line represents the yaw/heading angle error. One antenna DGPS aided INS is able to accurately estimate the pitch and roll angles with error standard deviations less than 0.11 deg, but the yaw angle error is not observable for a non-acceleration vehicle; while two antennae DGPS aided INS is able to accurately estimate all three attitude states with the roll angle error less than 0.11 deg, the pitch angle error less than 0.09 deg and the yaw angle error less than 0.27 deg.

[2]The magnetometer system can track longitudinal position to the accuracy of the magnet spacing if the magnet polarities are used to implement an error correcting code.

[3]The single GPS antenna is directly above the INS by 0.13 m.

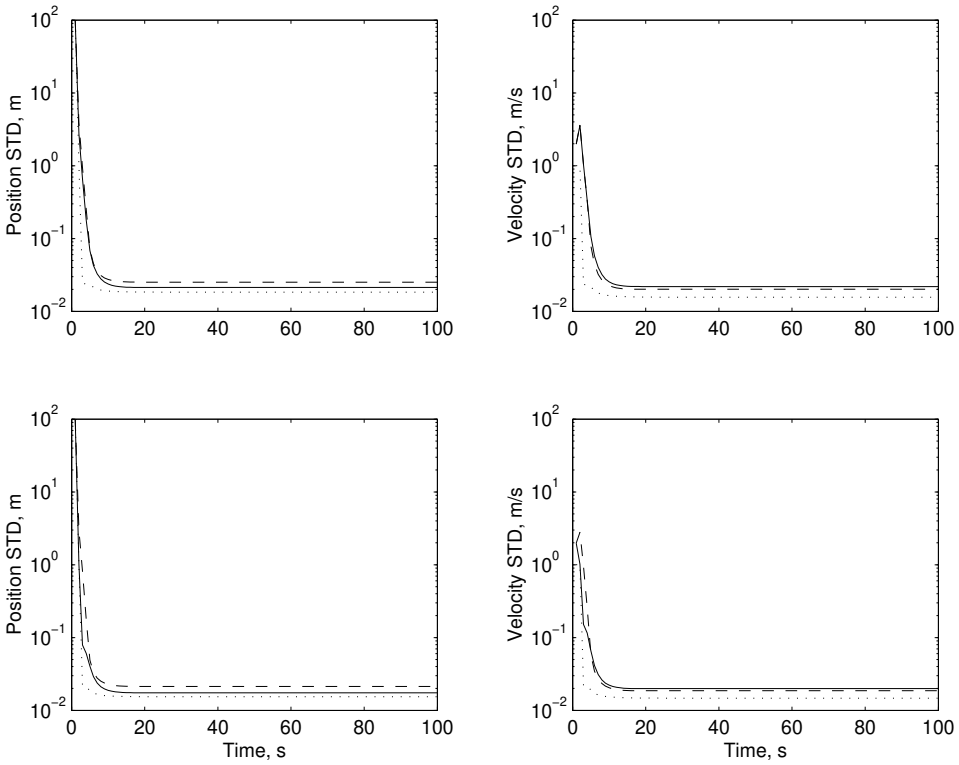

Figure 6: Position and velocity error standard deviation comparison between one antenna carrier phase DGPS/INS (top sub-figures) and two antenna carrier phase DGPS/INS (bottom sub-figures). The solid line is north. The dashed line is east. The dotted line is down.

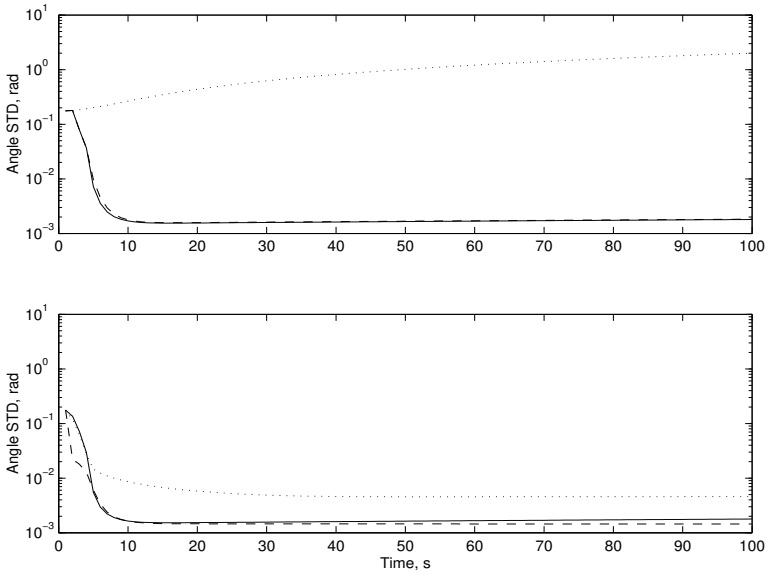

Figure 7: Attitude error standard deviation comparison between one antenna carrier phase DGPS/INS (top sub-figure) and two antennae carrier phase DGPS/INS (bottom sub-figure). The solid line is roll. The dashed line is pitch. The dotted line is heading.

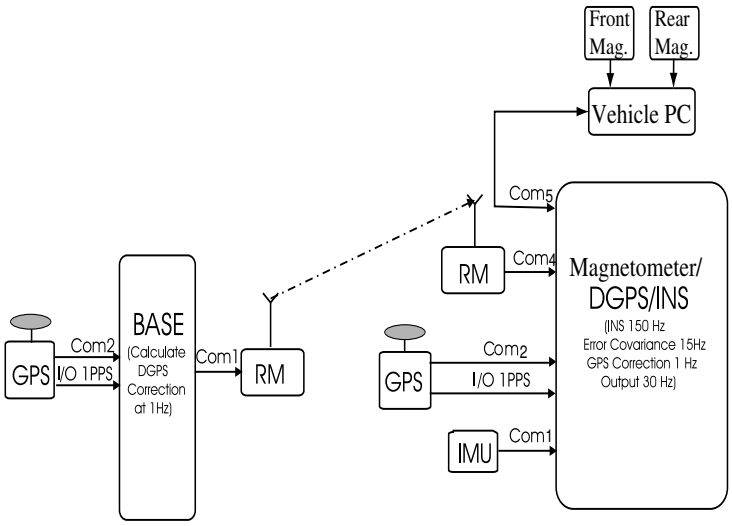

Figure 8: Magnetometer/GPS/INS integrated navigation system hardware composition and correction

5 Hardware and Software Design

This section describes the hardware, software architecture, and synchronization issues related to the two systems under discussion.

5.1 Magnetometer and GPS aided INS

This section describes the hardware, software architecture, and synchronization issues related to the magnetometer and DCPGPS aided INS.

5.1.1 Hardware Description for Magnetometer/GPS/INS

The system includes a stationary *base* station at a known ECEF location and a *rover* with a GPS antenna, two magnetometers, and an Inertial Measurement Unit (IMU). The system hardware composition and connections are shown in Figure 8.

At the base, the GPS receiver serial port output and the synchronizing 1PPS signal (a pulse aligned with the time of applicability of the GPS measurements) are connected to a PC by com2 at a 115.2k baud rate and an I/O port. After the base station calculation, GPS corrections (pseudorange, carrier phase, and Doppler) are broadcast at a 115.2k baud rate by the radio modem with a data package rate of once per second. The methodology and implementation of the base station is detailed in [12].

At the rover, the IMU is a CrossBow DMU-6X which includes a three-axis 2 g solid-state accelerometer (100Hz bandwidth) and a three-axis 100 deg/s solid-state gyro (10 Hz bandwidth). The DMU-6X performs anti-alias filtering, A/D conversion, start-up bias and axis-misalignment correction, and outputs the set of six inertial measurements by serial port at 150 Hz with a default baud rate of 38.4k to PC com1. The inexpensive solid state inertial instruments would be similar to the type of instrument expected in commercial automotive applications. The rover GPS serial port output and its 1PPS sychronizing signal are connected to the PC by com2 at a 115.2k baud rate and an I/O port. The base station corrections are connected to the PC via com4, and the vehicle control states are sent out by PC com5 at a 115.2k baud rate. The vehicle is equipped with two magnetometers. The magnetometers perform magnetic field detection, A/D conversion, and data transmission to the vehicle PC via serial ports. The vehicle PC receives the magnetometer measurements, packages them, and sends them to the integrated navigation system via com5. At the rover, a Pentium notebook, with an extended quad serial port PCMCIA card, is used to implement the tight integration of the GPS/INS/Magnetometer. In the system, the INS processing is calculated at 150 Hz. System error covariance propagation is calculated at 15 Hz. GPS aided INS is calculated at 1 Hz. The control state is calculated at 30 Hz. The base and rover use dual frequency Novatel RT-2 GPS receivers of that output pseudorange, carrier phase, and Doppler measurements for both L1 and L2. The magnetometer update rate

is discussed below. The differential base station to rover serial port connection is implemented through a 115.2k baud rate Freewave radio modem.

5.1.2 Synchronization between Magnetometers, GPS and INS

The synchronization between the GPS and the INS is discussed in [37]. The main new synchronization issue is that of the magnetometers with the synchronized GPS and INS.

As discussed [37], the maximum time error of the INS, after synchronization and compensation, is 0.0009 seconds, which is more than sufficient for land vehicle automatic control. The magnetometer measurements are also latent. The magnitude of this latency is determined by the time delay between the magnetometer passing the magnet and the navigation PC receiving this measurement. This delay is composed by three terms:

- **Magnetometer detection delay**: This delay is the sum of the magnetic field sensor delay, the A/D conversion time, and the transmission time between the magnetometer and the vehicle PC, and the peak detection latency. It may take $2 \sim 4$ milliseconds to detect that a peak after a magnet has been passed (specification provided by the magnetometer designer).
- **Vehicle PC processing delay**: This delay is determined by the vehicle PC software. An estimate of this delay is included in the data package that the vehicle PC transmits to the navigation PC.
- **Transmission delay between the vehicle PC and the navigation PC**: The 40 byte data package is transmitted from the vehicle PC to the navigation PC at a 115.2k baud rate. Hence, this delay can be calculated as $40 \times 10/115200 = 0.00347$ seconds.

In this system implementation, the magnetometer detection delay is approximately 0.003 seconds with a maximum time uncertainty 0.001 seconds. The vehicle PC processing delay is determined by the software on the vehicle PC with accuracy of one millisecond. The transmission delay between the vehicle PC and the navigation PC is 0.00347 seconds. Hence, the maximum synchronization time error between the magnetometers and GPS/INS is 0.0029 millisecond (1 millisecond detection error + 1 millisecond processing error + and 0.9 milliseconds INS latency error). This synchronization error yields less than 1 cm of lateral error for a vehicle with lateral velocity of less than 3 meters per second; therefore, this synchronization accuracy is acceptable.

5.1.3 QNX System Software Design and Implementation

The GPS/INS/Magnetometer system software is implemented using the QNX Real-Time Platform with multiple threads. The system modular architecture is illustrated in Figure 9.

The micro-kernel, process manager, and POSIX (a protocol of UNIX) m-queue blocks form the QNX Real-Time Platform, which is scalable and embeddable. The other modules are connected to the QNX Real-Time Platform. The system program consists of six threads and two drivers. The serial and PCMCIA drivers are used to communicate with hardware by address mapping and interrupt processing. The serial driver, which is used to receive 150 Hz IMU measurements, transmits data to the INS process by returning an event whenever it accumulates more than eighteen bytes. This driver is also used to count the received number of data bytes to synchronize the Kalman filter and vehicle control for data latency compensation. The PCMCIA driver is used to receive the GPS and magnetometer measurements, to receive the *base* corrections, to send vehicle control states to the vehicle, and to receive miscellaneous data from the vehicle. The six threads are INS, GPS, EKF, vehicle control, data logging, and data display. The six threads use the shared memory not only to save memory space, but also to make data exchange more convenient and efficient.

A real-time software package, called $MagGpsInsAtt$, was designed and implemented in QNX Real-Time Platform with Photon graphics. The C source code is 195.4 KB, the header files are 44.3 KB, and the executive file (with code size optimization and without the debug option) is 175 KB which is embedable. The test results with this software package are shown in Section 6.1.

5.2 Two Antenna GPS aided INS

This section describes the hardware, software architecture, and synchronization issues related to the two antennae DCPGPS aided INS.

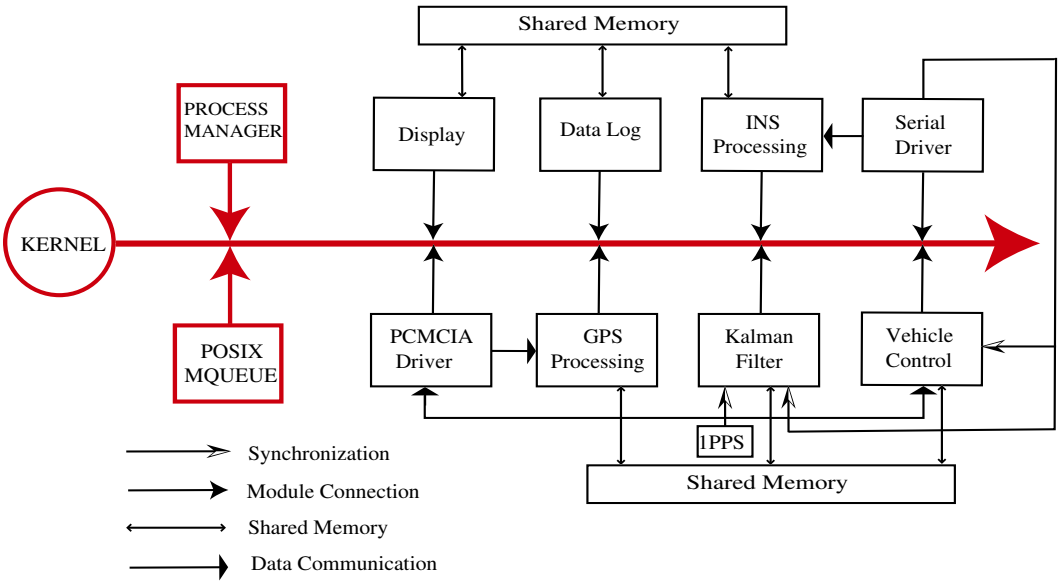

Figure 9: Realtime software architecture in QNX.

5.2.1 Hardware Description for Two-Antenna GPS/INS

The hardware includes a stationary *base* station, at a known ECEF location, and a *rover*, with two GPS antennae and an Inertial Measurement Unit (IMU) mounted as illustrated in Figure 10. The system hardware composition and connection are shown in Figure 11.

At the base, the GPS receiver serial port and synchronizing 1PPS signal (a pulse aligned with the time of applicability of the GPS measurements) are connected to a PC by com2 at a 115.2k baud rate and an I/O port, respectively. After the base station calculations, GPS corrections for pseudorange, carrier phase, and Doppler are broadcast at a 115.2k baud rate by the radio modem (RM) with a data package rate of once per second. The methodology and implementation of the base station is detailed in [12].

At the rover, the IMU is a CrossBow DMU-6X which includes a three-axis 2 g solid-state accelerometer (100Hz bandwidth) and a three-axis 100 deg/s solid-state gyro (10 Hz bandwidth). The DMU-6X performs anti-alias filtering, A/D conversion, start-up bias and axis-misalignment correction, and outputs the set of six inertial measurements by serial port at 150 Hz with a default baud rate 38.4k to PC com1. The inexpensive solid state inertial instruments would be similar to the type of instrument expected in commercial automotive applications. $\mathbf{GPS}_2$ receiver measurements and its 1PPS sychronizing signal are connected to a PC by com2 at a 115.2k baud rate and an I/O port, respectively. $\mathbf{GPS}_1$ outputs are connected to the PC by com3 at a 115.2k baud rate. The base station corrections are connected to the PC via com4, and the vehicle control states are sent out by PC com5 at a 115.2k baud rate. At the rover, a Pentium notebook, with extended serial PCMCIA card, is used to implement the tight integration of the Two-Antenna GPS/INS. In the system, the

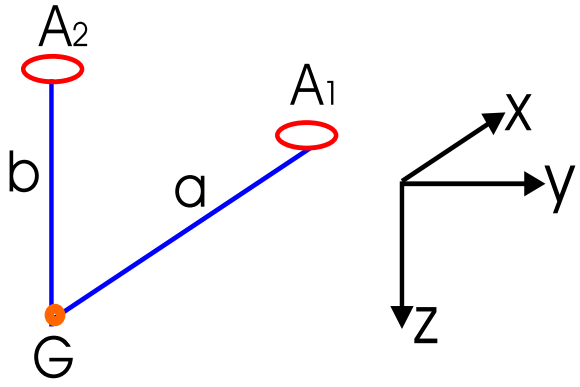

Figure 10: Two-antennae configuration for GPS/INS attitude determination.

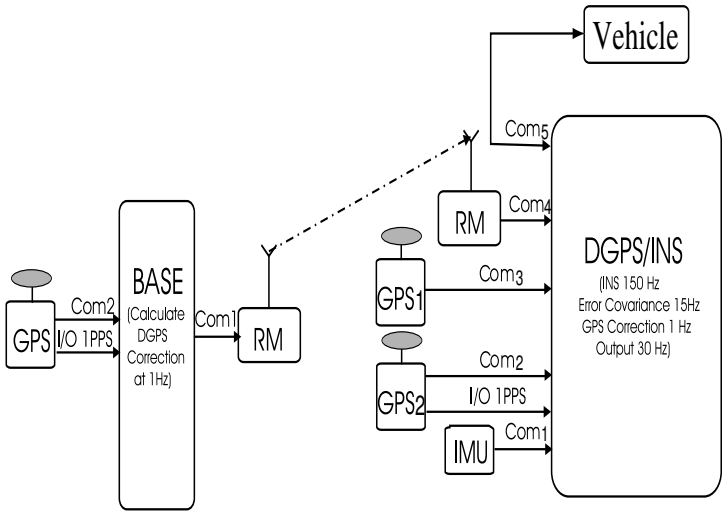

Figure 11: Two antennae GPS/INS integrated navigation system hardware architecture.

INS processing is calculated at 150 Hz. The system error covariance propagation is calculated at 15 Hz. The GPS aided INS is calculated at 1 Hz. The control states are calculated at 30 Hz. The base **GPS** and $\mathbf{GPS}_2$ are dual frequency GPS receivers (Novatel RT-2) which outputs pseudorange, carrier phase, and Doppler measurements for both L1 and L2. $\mathbf{GPS}_1$ is a single frequency GPS receiver that outputs L1 carrier phase measurements. The differential base station to rover serial port connection is implemented through a 115.2k baud rate Freewave radio modem.

5.2.2 QNX System Software Design of Two-Antenna GPS/INS

A real-time software package, called *GpsInsAtt*, was designed and implemented using the QNX Real-Time Platform with Photon graphics. The C source code is 179.8 KB, the header files are 43.5 KB, and the executive file (with code size optimization and without the debug option) is 161 KB. This is small enough to be suitable for embedded system.

The system is implemented with multiple threads. The system modular architecture and relationship are shown in Figure 9. The micro-kernel, process manager, and POSIX (a protocol of UNIX) m-queue blocks form the QNX Real-Time Platform, which is scalable and embedded, and other modules are connected to the QNX Real-Time Platform. By module connection, the program performs functions related to the QNX Real-Time Platform, such as thread scheduling and message passing. The system program consists of six threads and two drivers. The serial driver and PCMCIA driver are used to communicate with hardware by address mapping in response to interrupts. The six threads that perform system functions are INS, GPS, Kalman filter, vehicle control, data log, and data display. The serial driver, which is used to receive IMU measurements, transmits data to INS processing by returning an event whenever it accumulates more than eighteen Bytes of data, and is used to count the received number of data bytes to synchronize the Kalman filter and vehicle control for data latency compensation. The $\mathbf{GPS}_2$ 1PPS is used to synchronize the Kalman filter time update. The PCMCIA driver is used to receive the $\mathbf{GPS}_1$ measurement data, the $\mathbf{GPS}_2$ measurement data, and the *base* corrections. It is also used to send the trajectory relative vehicle control state to the vehicle and to receive the vehicle information from the control computer. The six threads use shared memory not only to save memory space, but also to make data exchange more convenient and efficient. The test results with this software package are presented in Section 6.2.

6 Experimental Results

This section describes results of experiments completed in the parking lot of the UCR CE-CERT facility in Riverside, CA during May 2001. The magnetometer and DCPGPS aided INS results are described in Subsection 6.1. The two antenna DCPGPS aided INS results are presented in Subsection 6.2.

6.1 Magnetometer and GPS aided INS

This section presents on vehicle GPS/INS/Magnetometer test results. All the results were obtained while the integrated system had integer-resolved GPS phase lock. Since the magnetometer can not provide measurements unless it is moving, all the results described below involve lateral control of a moving vehicle. The lateral control algorithm is described in [14]. The control state calculation approach is presented in [14, 35]. All results are for trajectory following. Trajectory relative maneuvering [14, 35] was not possible as the experiments required laying out a path of magnetic bars along the trajectory.

6.1.1 GPS/INS/Magnetometer based vehicle control with GPS On

For this set of experiments, both differential GPS carrier phase and magnetometer measurements are used to aid the INS. Therefore, triple sensor redundancy is available. The magnetometer corrects lateral error relative to the trajectory formed by the magnetic bars. GPS corrects both the longitudinal and lateral error relative to a curve fit trajectory. The method for determining the curve fit trajectory is described in [11].

Figure 12 shows the position, velocity, and angle data from GPS/INS/magnetometer for trajectory following vehicle control. The top sub-figures show a north-east plot of the horizontal position data and time series plots of the position estimates. The middle sub-figures show the time series plots of the velocity estimates and acceleration measurements. The bottom sub-figures show time series plots of the attitude estimates and angular rate measurements. Note that the vehicle is driving (essentially) east to west. The North coordinate therefore shows the control system convergence toward the trajectory.

Figure 13 shows the trajectory relative control data for GPS/INS/Magnetometer based trajectory following. In this figure, the GPS/INS/Magnetometer control states $(d, \dot{d}, \epsilon, \dot{\epsilon})$ are shown in the four plots of the left column. The upper left figure shows the off-trajectory estimate d of the GPS/INS/Magnetometer (solid) and the front magnetometer measurement of d (dotted). The Kalman filter corrections are clearly indicated in the calculated off-trajectory distance plot. The magnetometer data is equal to zero for the first five seconds, since the magnetometer has not yet reached the first magnet. The magnetometer and GPS/INS/magnetometer estimates of d match to cm accuracy. The lateral controller drives d to zero in approximately 10 s. The second left figure shows GPS/INS/Magnetometer estimate of the velocity normal to the trajectory. The third left figure shows the GPS/INS/Magnetometer estimate of the heading error with respect to the trajectory. The bottom left figure shows the heading error rate estimate from GPS/INS/Magnetometer. The right column includes various variables related to the trajectory and the experiment. The upper right figure shows the vehicle velocity tangent to the trajectory. The second right figure shows the trajectory curvature versus time. The third right figure shows the vehicle heading versus time. The error between the vehicle heading and the trajectory heading is the heading error shown in the third left figure. The bottom right figure shows the vehicle yaw rate.

6.1.2 GPS/INS/Magnetometer based vehicle control with GPS On/Off

For this set of runs, magnetometer measurements are used whenever they are available. GPS measurements were ignored from $t = 5s$ to $t = 10s$. This situation is similar to the scenario where the vehicle passes through a tunnel, so that the GPS satellite signals are temporarily unavailable. While the GPS signals are not available, the magnetometer alone is used to aid the INS.

Figure 14 shows the position, velocity, and angle data from GPS/INS/magnetometer for trajectory following vehicle control. The top sub-figures show a north-east plot of the horizontal position data and time series plots of the position estimates. The middle sub-figures show the time series plots of the velocity estimates and acceleration measurements. The bottom sub-figures show time series plots of the attitude estimates and angular rate measurements.

Figure 15 shows the corresponding trajectory relative control state. In this figure, the GPS/INS/Magnetometer control states $(d, \dot{d}, \epsilon, \dot{\epsilon})$ are shown in the four plots of the left column. The upper left figure shows the GPS/INS/Magnetometer estimate (solid) and front magnetometer measurement (dotted) of the off trajectory distance d. The second left figure shows the GPS/INS/Magnetometer estimate of the trajectory relative normal velocity. The third left figure shows the GPS/INS/Magnetometer estimate of the trajectory relative

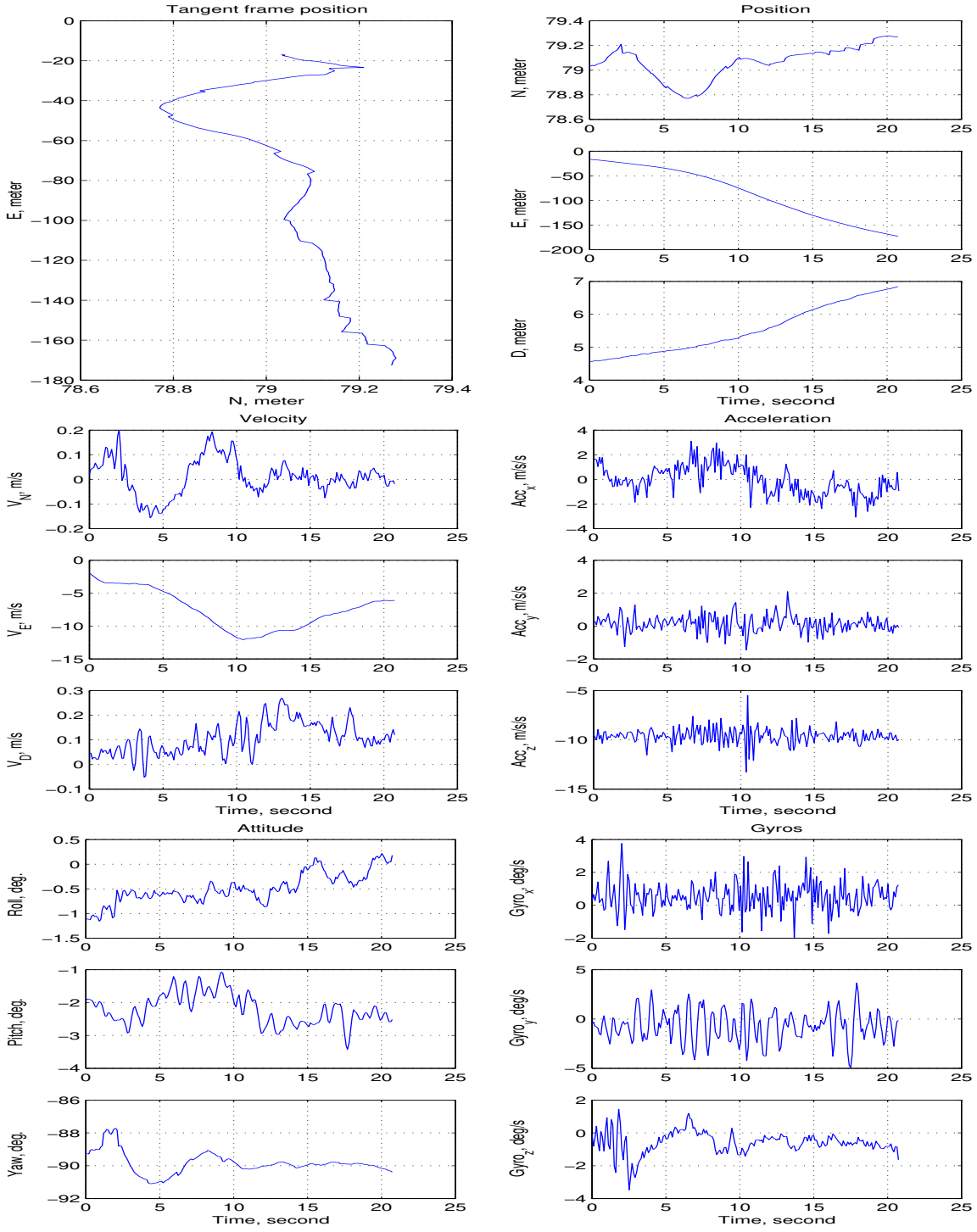

Figure 12: Position, velocity, and angle for trajectory following vehicle control data when both GPS and magnetometer measurements are used. Top: Plot of the horizontal position data and time series plots of the position estimates. Middle: Time series plots of velocity estimates and acceleration measurements. Bottom: Time series plots of attitude estimates and angular rate measurements. This figure corresponds to Figure 13.

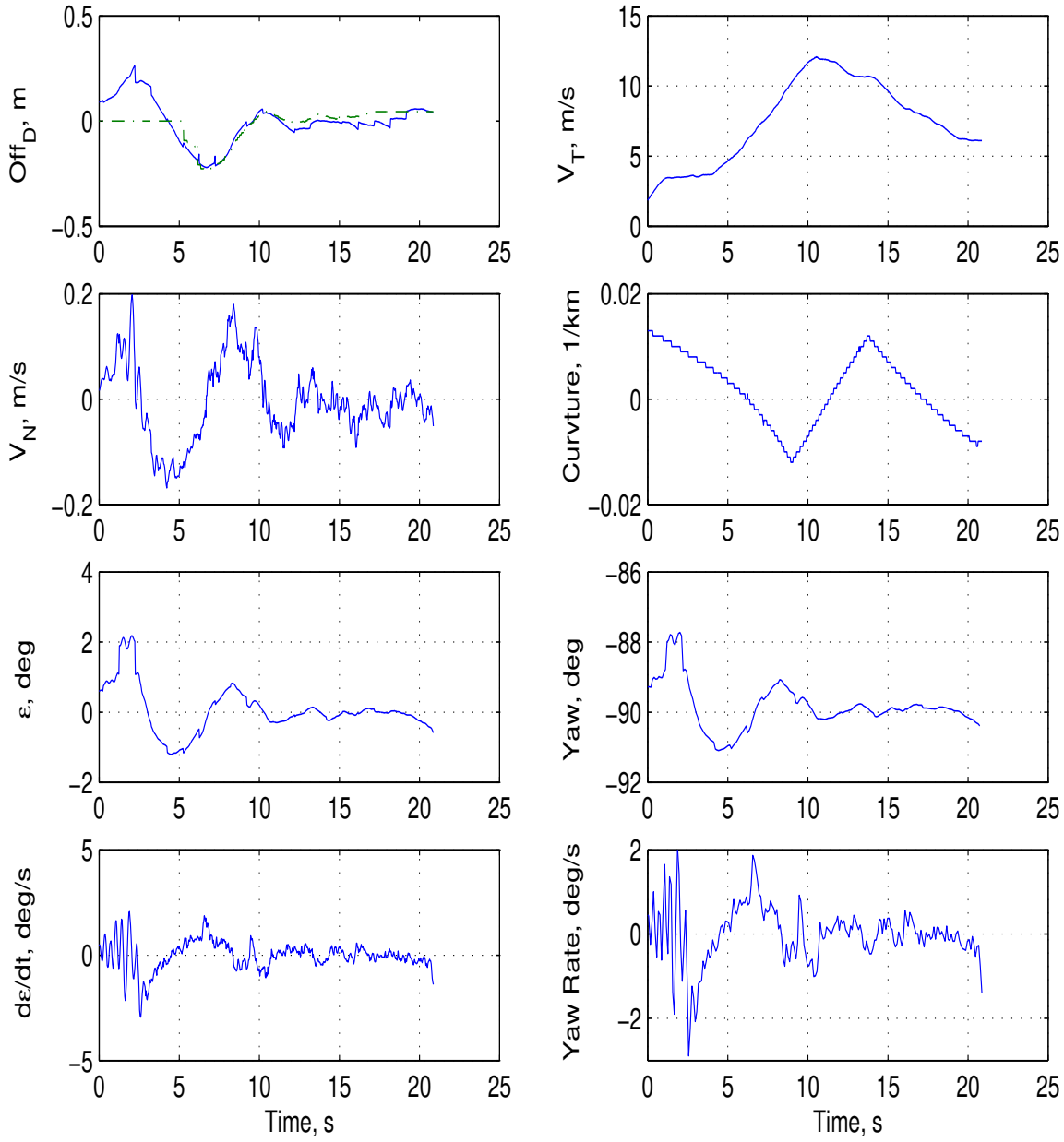

Figure 13: GPS/INS/Magnetometer control results for trajectory following. The left column of plots shows the integrated GPS/INS/Magnetometer estimate of the control state vector. The right column of plots shows trajectory relative information. Top left: Time series plot of the off-trajectory distance as determined by the GPS/INS/Magnetometer (solid) and the front magnetometer (dotted). Second left: GPS/INS/Magnetometer estimate of velocity normal to the trajectory. Third left: GPS/INS/Magnetometer estimate of the trajectory relative heading error. Bottom left: Trajectory relative heading error rate estimate from GPS/INS/Magnetometer. Top right: GPS/INS/Magnetometer estimate of the velocity tangent to the trajectory. Second right: The trajectory curvature. Third right: The vehicle heading. Bottom right: The vehicle yaw rate. This figure corresponds to Figure 12.

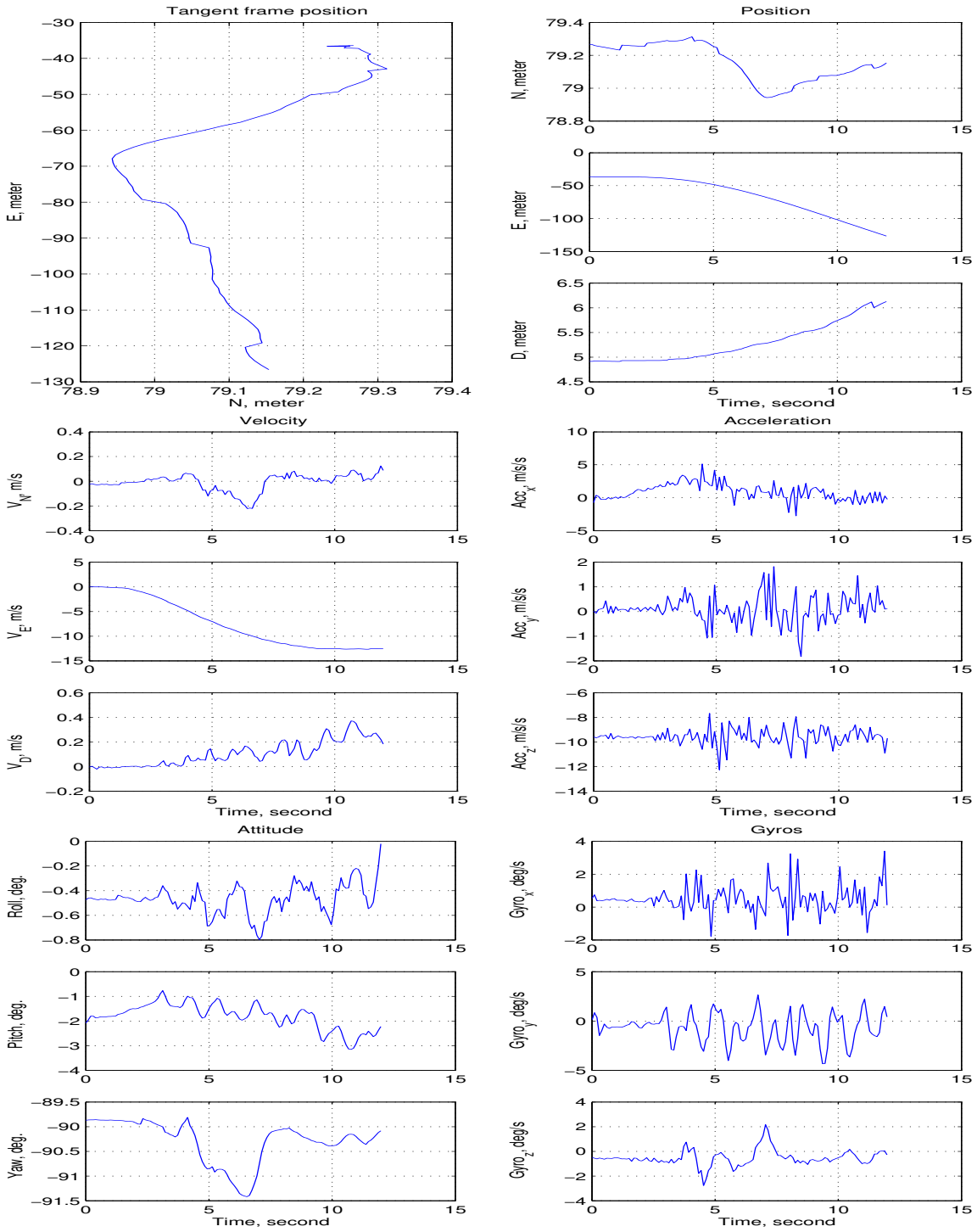

Figure 14: Position, velocity, and angle for trajectory following vehicle control data using GPS/INS /Magnetometer when GPS is switched between on and off. Top: Plot of the horizontal position data and time series plots of the position estimates. Middle: Time series plots of velocity estimates and acceleration measurements. Bottom: Time series plots of attitude estimates and angular rate measurements. This figure corresponds to Figure 15.

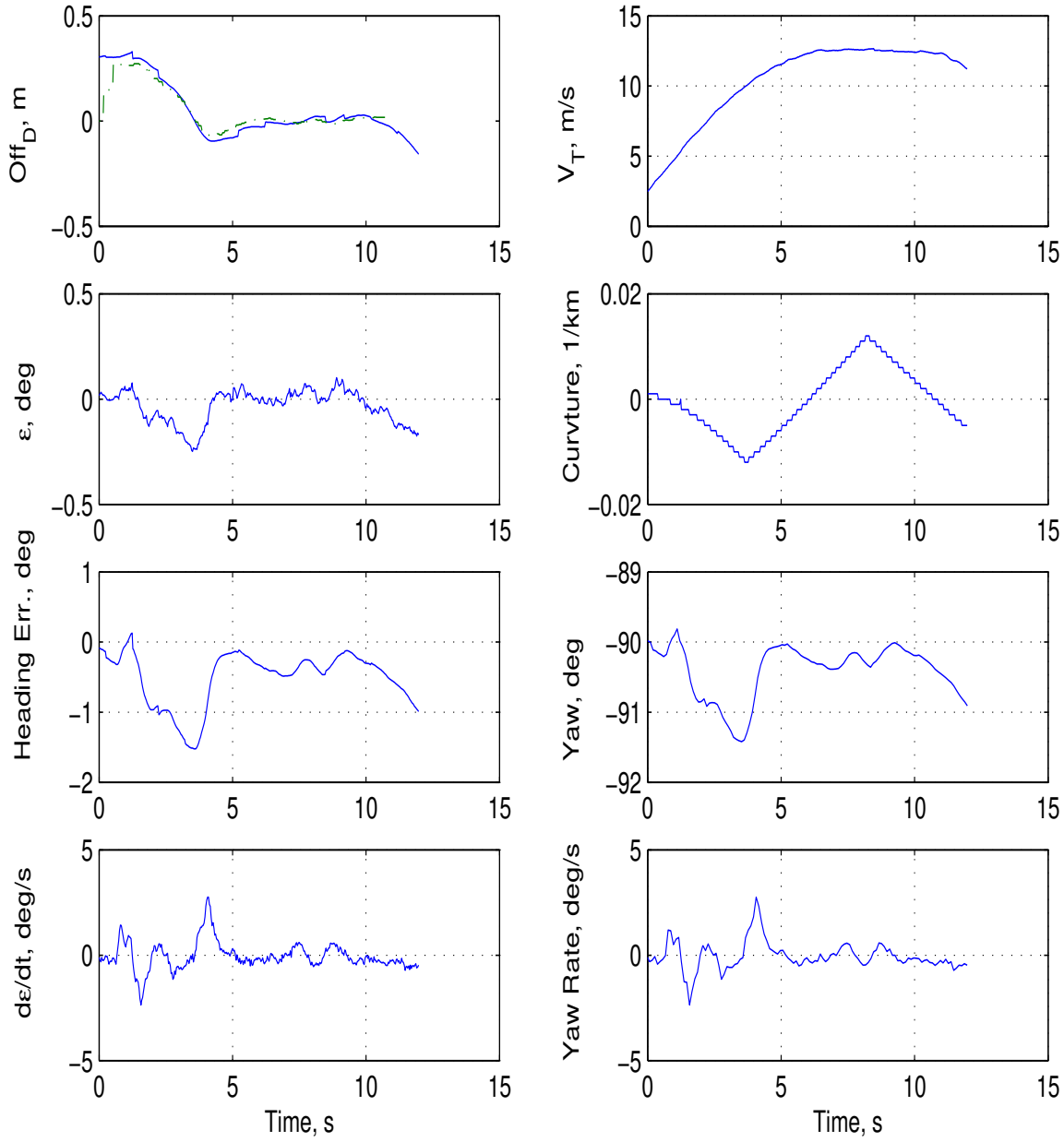

Figure 15: GPS/INS/Magnetometer based control for trajectory following. GPS is off for $t \in [5, 10]s$. The left column of plots shows the integrated GPS/INS/Magnetometer estimate of the control state vector. The right column of plots shows trajectory relative information. Top left: Time series plot of the off-trajectory distance as determined by the GPS/INS/Magnetometer (solid) and the front magnetometer (dotted). Second left: GPS/INS/Magnetometer estimate of velocity normal to the trajectory. Third left: GPS/INS/Magnetometer estimate of the trajectory relative heading error. Bottom left: Trajectory relative heading error rate estimate from GPS/INS/Magnetometer. Top right: GPS/INS/Magnetometer estimate of the velocity tangent to the trajectory. Second right: The trajectory curvature. Third right: The vehicle heading. Bottom right: The vehicle yaw rate. This figure corresponds to Figure 14.

heading error. The bottom left figure shows the trajectory relative heading error rate. The right column includes various variables related to the trajectory and the experiment. The upper right figure shows the vehicle velocity tangent to the trajectory. The second right figure shows the trajectory curvature. The third right figure shows the vehicle heading versus time. The error between the vehicle heading and the trajectory heading is the heading error shown in the third left figure. The heading error is nonzero between $t = [3, 10]s$, since the controller is driving d to zero. The bottom right figure shows the vehicle yaw rate.

In the first two seconds, only the GPS measurement was used for system integration. For $t \in [2, 4]$s, both GPS and magnetometer measurements were used. For $t \in [5, 10]$s, only magnetometer measurements were used. For $t > 10$s, magnetometer measurements were not available and only GPS measurements were used. After the $t = 10$s, the vehicle was switched to manual control and driven away from the trajectory. Figure 15 shows the control and navigation performance is the same (i.e., centimeter accuracy) during the 5.0 s interval when GPS data is not available. Also, due to the EKF integration approach, the transitions between the available measurements are smooth.

6.1.3 GPS/INS/Magnetometer based vehicle control with GPS Off

In this experiment, only magnetometer measurements were used to aid the INS for the entire period of time when the vehicle is on the trajectory formed by the magnets. This situation is similar to the scenario that the vehicle passes a tunnel or bridge that blocks all the GPS satellite signals.

Figure 16 shows the position, velocity, and angle data from GPS/INS/magnetometer for trajectory following vehicle control. The top sub-figures show a north-east plot of the horizontal position data and time series plots of the position estimates. The middle sub-figures show the time series plots of the velocity estimates and acceleration measurements. The bottom sub-figures show time series plots of the attitude estimates and angular rate measurements.

Figure 17 shows the control results with GPS/INS/Magnetometer based vehicle trajectory following when only magnetometer measurements were used. In this figure, the GPS/INS/Magnetometer control state vector ($[d, \dot{d}, \epsilon, \dot{\epsilon}]$) is shown in the four plots of the left column. The upper left figure shows the GPS/INS/Magnetometer estimate (solid) and the front magnetometer measurement of th off-trajectory distance d. The second left figure shows GPS/INS/Magnetometer estimate of the velocity normal to the trajectory. The third left figure shows the GPS/INS/Magnetometer estimate of the trajectory relative heading error. The bottom left figure shows the GPS/INS/Magnetometer estimate of the trajectory relative heading error rate. The right column includes various variables related to the trajectory and the experiment. The upper right figure shows the vehicle tangent velocity along the trajectory. The second right figure shows the trajectory curvature. The third right figure shows the vehicle heading. The error between the vehicle heading and the trajectory heading is the heading error shown in the third left figure. The bottom right figure shows the vehicle yaw rate.

For the scenario of this experiment, the INS/Magnetometer is expected to be able to maintain an accurate estimate of position lateral to the trajectory, but the longitudinal position (slowly) may diverge. From Figure 17, the off-trajectory distance calculated by INS/Magnetometer matches the magnetometer measured off-trajectory distance quite well with centimeter lateral accuracy. This illustrates the fact that the magnetometer aided INS can maintain lateral position accuracy as required for lane-keeping control or lane departure warning.

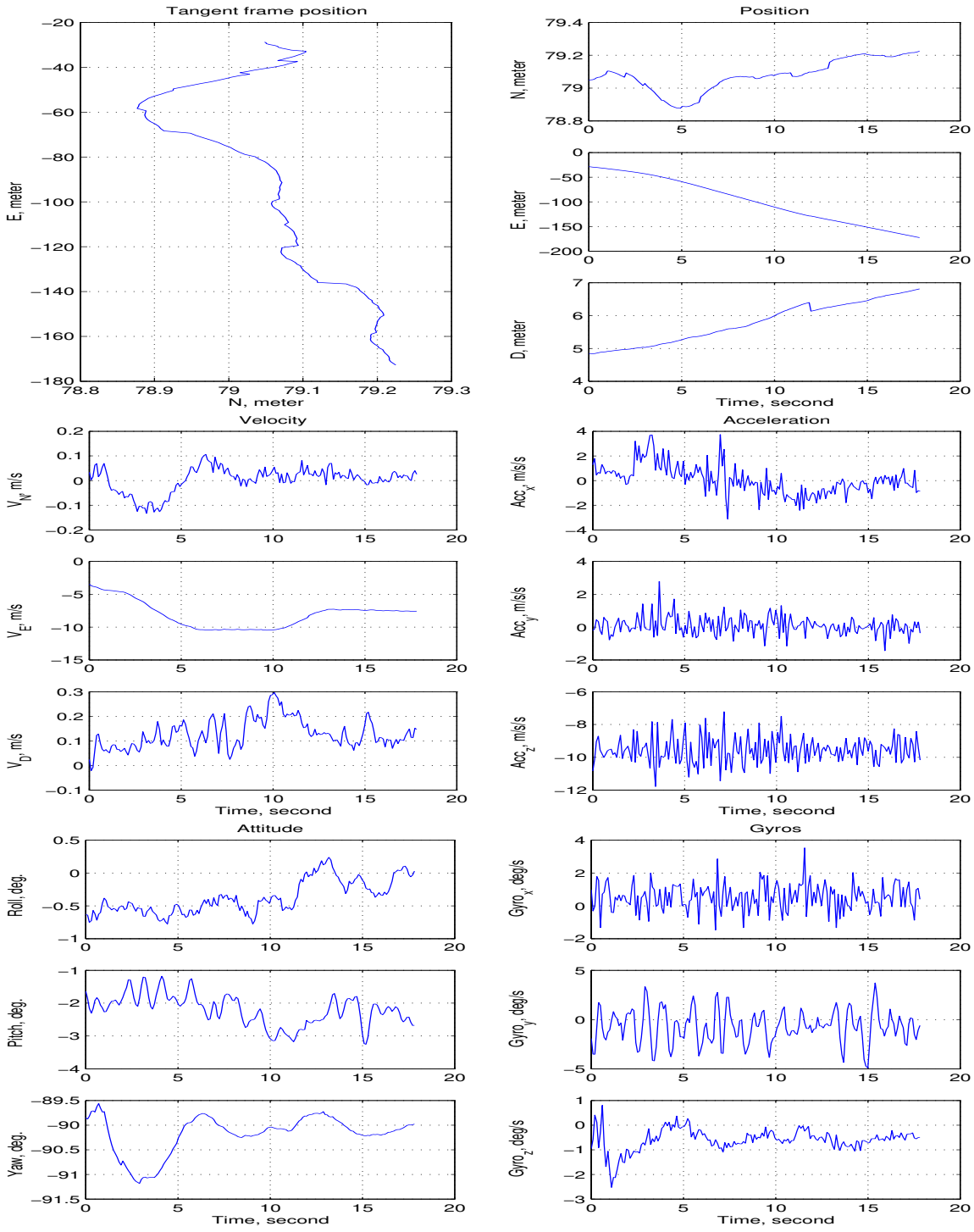

Figure 16: Position, velocity, and angle for trajectory following vehicle control data with GPS/INS /Magnetometer when only magnetometer measurement was used. Top: Plot of the horizontal position data and time series plots of the position estimates. Middle: Time series plots of velocity estimates and acceleration measurements. Bottom: Time series plots of attitude estimates and angular rate measurements. This figure corresponds to Figure 17.

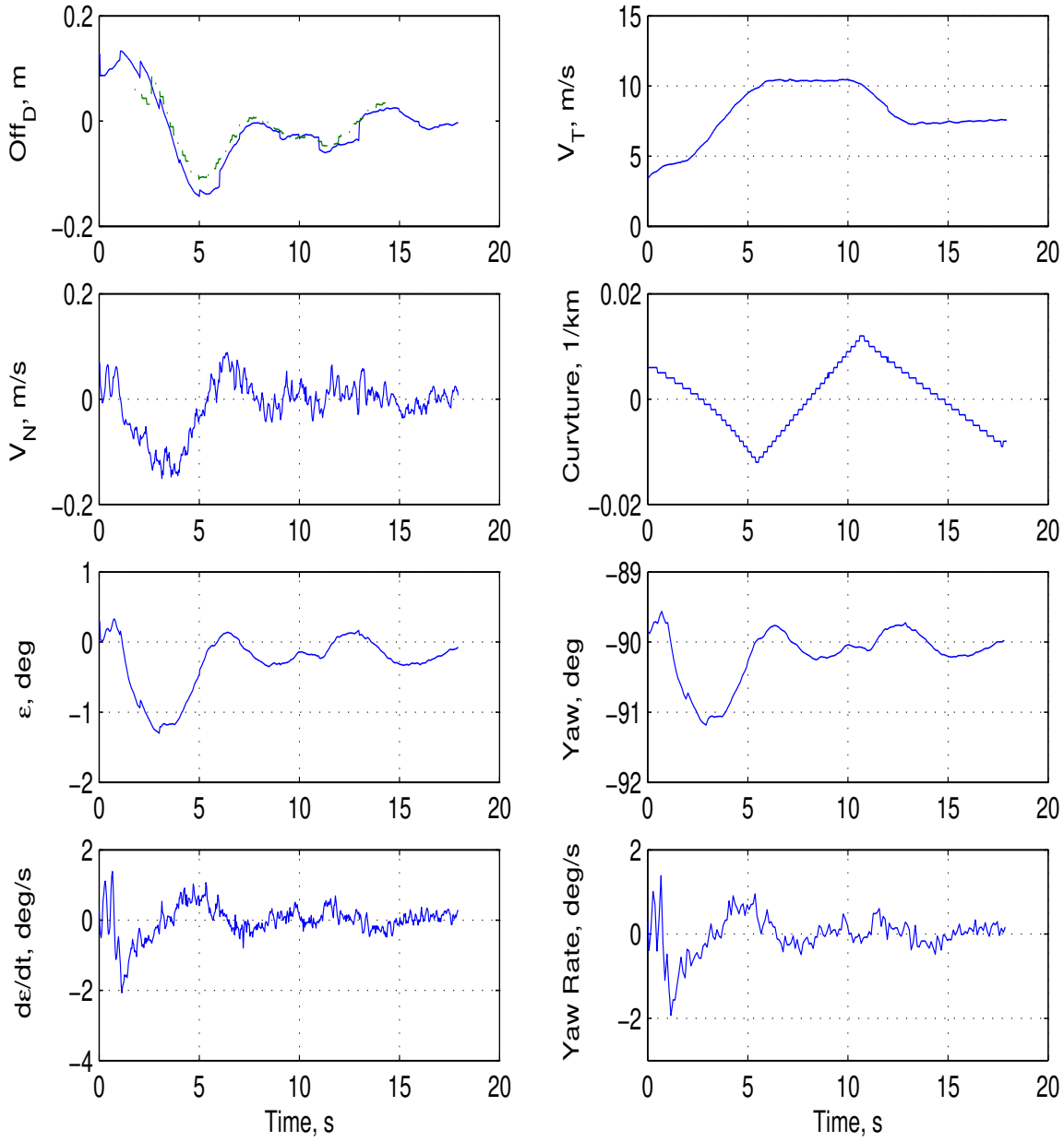

Figure 17: GPS/INS/Magnetometer trajectory following control results. GPS is off for $t > 2s$. The left column of plots shows the integrated GPS/INS/Magnetometer estimate of the control state vector. The right column of plots shows trajectory relative information. Top left: Time series plot of the off-trajectory distance as determined by the GPS/INS/Magnetometer (solid) and the front magnetometer (dotted). Second left: GPS/INS/Magnetometer estimate of velocity normal to the trajectory. Third left: GPS/INS/Magnetometer estimate of the trajectory relative heading error. Bottom left: Trajectory relative heading error rate estimate from GPS/INS/Magnetometer. Top right: GPS/INS/Magnetometer estimate of the velocity tangent to the trajectory. Second right: The trajectory curvature. Third right: The vehicle heading. Bottom right: The vehicle yaw rate. This figure corresponds to Figure 16.

Data	N	E	D	V_N	V_E	V_D	ϕ	θ	ψ
1	60.477	-293.248	8.608	0.003	-0.007	-0.014	1.007	-0.019	-179.366
2	60.468	-293.239	8.619	-0.000	-0.005	-0.003	0.972	-2.503	-179.365

Table 1: Mean value of estimated position, velocity, and attitude for two stationary experiments. Position units are meters, velocity units are m/s, and attitude units are degrees.

Data	N	E	D	V_N	V_E	V_D	ϕ	θ	ψ
1	0.0087	0.0081	0.0131	0.0069	0.0066	0.0062	0.020	0.024	0.050
2	0.0084	0.0079	0.0119	0.0068	0.0064	0.0072	0.025	0.026	0.082

Table 2: Standard deviation of estimated position, velocity, and attitude for two stationary experiments. Position units are meters, velocity units are m/s, and attitude units are degrees.

6.2 Two Antenna GPS aided INS

This section presents the results of the vehicle testing with Two-Antenna GPS/INS. All the results were obtained after the integrated system had resolved the GPS integer ambiguities.

6.2.1 Stationary Experimental Results

Table 1, Table 2, Figure 18, and Figure 19 show data acquired while the vehicle was stationary. Although the objective of this research project is to achieve the accurate navigation and automatic vehicle control while the vehicle is in motion, the stationary results are useful for analyzing the accuracy of the vehicle heading estimate in non-accelerating conditions. The stationary vehicle data also valuable for overall evaluation of system performance since certain characteristics are more clearly observed in static mode than in dynamic mode. The positions shown in Table 1, Figure 18, and Figure 19 correspond to a random location where the vehicle stopped during testing. These two sets of data are two successive log files while the vehicle was stationary. The only difference in the vehicle state for these two data files is that one of the authors was in the back seat of the vehicle while logging file one, but left the vehicle after file two began to log[4].

The Two-Antenna GPS/INS integrated navigation system accurately estimates (see Table 2) the horizontal positions with standard deviation less than 1 centimeter, vertical position with standard deviation less than 1.5 centimeters, velocities with standard deviation less than 0.008 m/s, pitch and roll angles with standard deviation less than 0.03 degrees, and heading with standard deviation less than 0.1 degrees. This demonstrated accuracy matches well the goal of the research project and system design.

It is worth mentioning that when the latency of the integrated navigation system is well compensated, the navigation accuracy is essentially independent of velocity. Hence, the quantitative measures of performance determined in this section are indicative of the performance expected in the later sub-sections.

6.2.2 Dynamic Experimental Results for Vehicle Control

This section presents the experimental results for vehicle control based on the Two-Antenna GPS/INS integrated navigation system. The control states calculation algorithm is presented in [14, 35]. Results of various maneuvering modes are shown below.

Basic Maneuvering. In this maneuvering mode, the vehicle lateral position was controlled using the trajectory relative control state calculated based on the two-antenna GPS/INS vehicle state vector. The block diagram is shown in Figure 2. During this basic maneuver, the control objective is to force the off-trajectory distance d and trajectory relative heading error ϵ to zero. Figure 20 shows the vehicle state data from the two-antenna GPS/INS. The top sub-figures show the horizontal position data and their time series plots. The middle sub-figures show the velocity estimates and acceleration measurements. The bottom sub-figures show attitude estimates and angular rate measurements.

Figure 21 shows the control state vector $[d, \dot{d}, \epsilon, \dot{\epsilon}]$ in the four plots of the left column. For these experiments, the desired trajectory is defined by a strip of magnets laid out in a parking lot and a magnetometer system onboard the vehicle was available for establishing ground truth relative to the magnet trajectory. The magnetometer measurements are not used by the control or navigation algorithms. The upper left figure

[4]Note the change in pitch near the beginning of Figure 19.

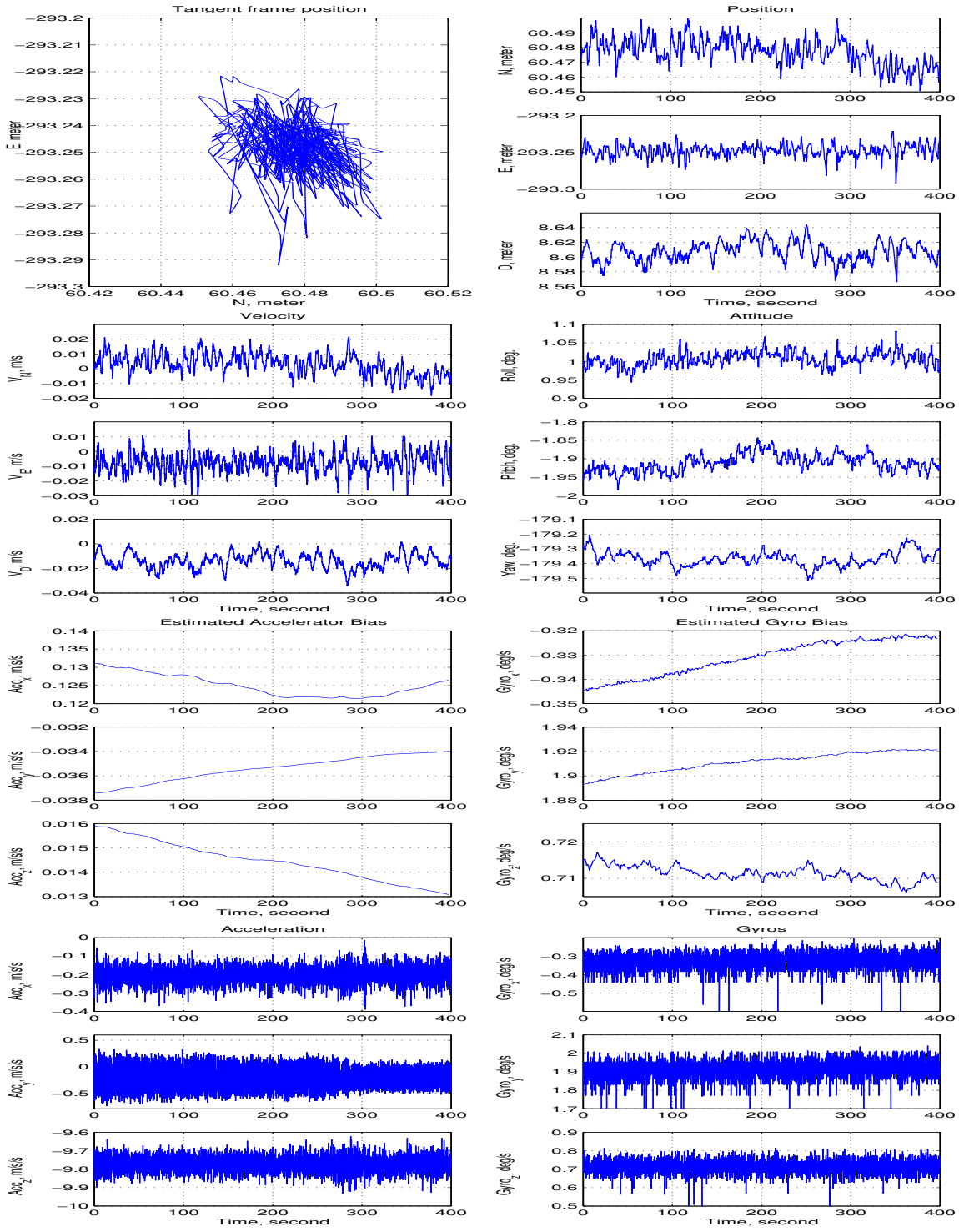

Figure 18: Position, velocity, and angle using two-antenna integer-resolved DGPS/INS for a stationary vehicle. Top: Plot of the horizontal position data and time series plots of the position estimates. Top second: Time series plots of the velocity estimates and attitude estimates. Top third: Time series plots of the acceleration and angular rate bias estimates. Bottom: Time series plots of the uncompensated acceleration and angular rate measurement.

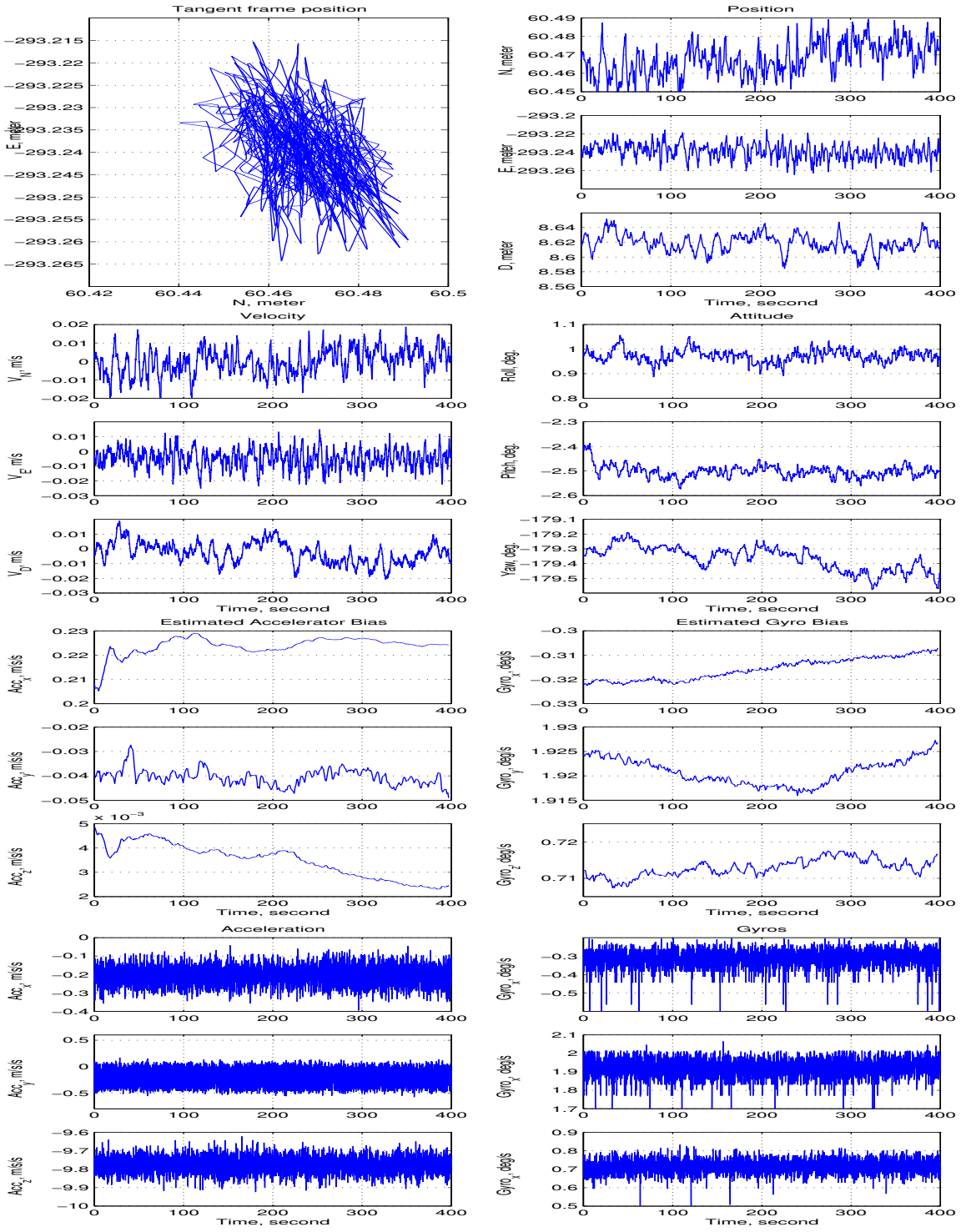

Figure 19: Position, velocity, and angle using the two-antenna integer-resolved DGPS/INS for a stationary vehicle. Top: Plot of the horizontal position data and time series plots of the position estimates. Top second: Time series plots of the velocity estimates and attitude estimates. Top third: Time series plots of the acceleration and angular rate bias estimates. Bottom: Time series plots of the uncompensated acceleration and angular rate measurement.

compares the Two-Antenna GPS/INS (solid) estimate of d with the magnetometer measurement (dotted) of d. The magnetometer measurement is available from the 4th second to the 25th second. At the beginning of the trajectory, there is a transition error between the trajectory formed by the magnetic bars and the curve fit trajectory used by the GPS/INS to calculate d. The magnetometer and GPS/INS estimates of d match to centimeter accuracy and have consistent dynamic characteristics. The second left figure shows the two-antenna GPS/INS estimate of velocity normal to the trajectory. The third left figure shows the two-antenna GPS/INS estimate of trajectory relative heading error. The bottom left figure shows the trajectory relative heading error rate estimate from two-antenna GPS/INS.

The right column includes various variables related to the trajectory and the experiment that are useful for interpreting the results in the left column. The upper right figure shows the vehicle velocity tangent to the trajectory. The second right figure shows the trajectory curvature versus time. The curve fit trajectory is formed by four segments of a fourth order B-spline. The change in curvature indicated in this figure is due to the spline fit, not the trajectory. The third right figure shows the vehicle heading versus time, which shows the vehicle is pointing west. The error between the vehicle heading and the trajectory heading is the heading error shown in the third left figure. The bottom right figure shows the vehicle yaw rate.

Throughout, the transients in the control states have consistent dynamic characteristics. For instance, at any time when $\dot{d} = 0$, the variable d is at an extreme value; and at any time when $\dot{\epsilon} = 0$, the variable ϵ is at an extreme value. The centimeter accuracy comparison between the magnetometer measurement and the Two-Antenna GPS/INS estimate of d and the consistency of the control states demonstrate the accuracy of the Two-Antenna GPS/INS system.

Advanced Maneuvering–Lane Change. The trajectory used in the experiments of the previous section had obstacles too close to allow safe trajectory relative maneuvering; therefore, the trajectory was shifted south by 13 meters before completing the advanced maneuvers described in this section. Due to this relocation of the trajectory, magnetometer ground truth measurements are not available.

A lane-change is implemented by adding perturbations, as disturbances (see Section **??**), to the control state. If the controller rejects these added disturbances, then the vehicle has performed the desired maneuver. The lane change perturbation:

- was 0.0 for 20 meters of path length;
- changed smoothly from 0.0 to -3.6 m over the next 50 meters of path length;
- stayed at -3.6 m for 50 meters;
- changed smoothly from -3.6 m to 0.0 m over the next 50 meters of path length.

Throughout this maneuver, the perturbation was twice differentiable.

Figure 22 shows the position, velocity, and angle data from two-antenna GPS/INS during the lane-change maneuver. The top sub-figures show the plot of the horizontal position data and time series plots of the position estimates. The second top sub-figures show the time series plots of the velocity and attitude estimates. The third top sub-figures show the time series plots of the accelerometer and gyro bias estimates. The bottom sub-figures show time series plots of the acceleration and angular rate measurements.

Figure 23 shows the control results during lane-change maneuvering. Note that the controller driving the control state plus perturbations to zero causes the control state to follow the opposite of the perturbation. In this figure, the two-antenna GPS/INS control states $(d, \dot{d}, \epsilon, \dot{\epsilon})$ are shown in the four plots of the left column. The right column includes various variables related to the trajectory and the experiment.

Advanced Maneuvering–Sinusoids. This section presents results for following a perturbation to the trajectory. The perturbation function did following:

- was 0.0 for 20 meters of path length;
- was a 1.0 m amplitude sine-wave with 100 meters wave length for two cycles;
- was 0.0 for the duration of the run.

Figure 24 shows the position, velocity, and angle data from the two-antenna GPS/INS during the tracking of this sinusoidal maneuver. Figure 25 shows the control state during the same maneuvering.

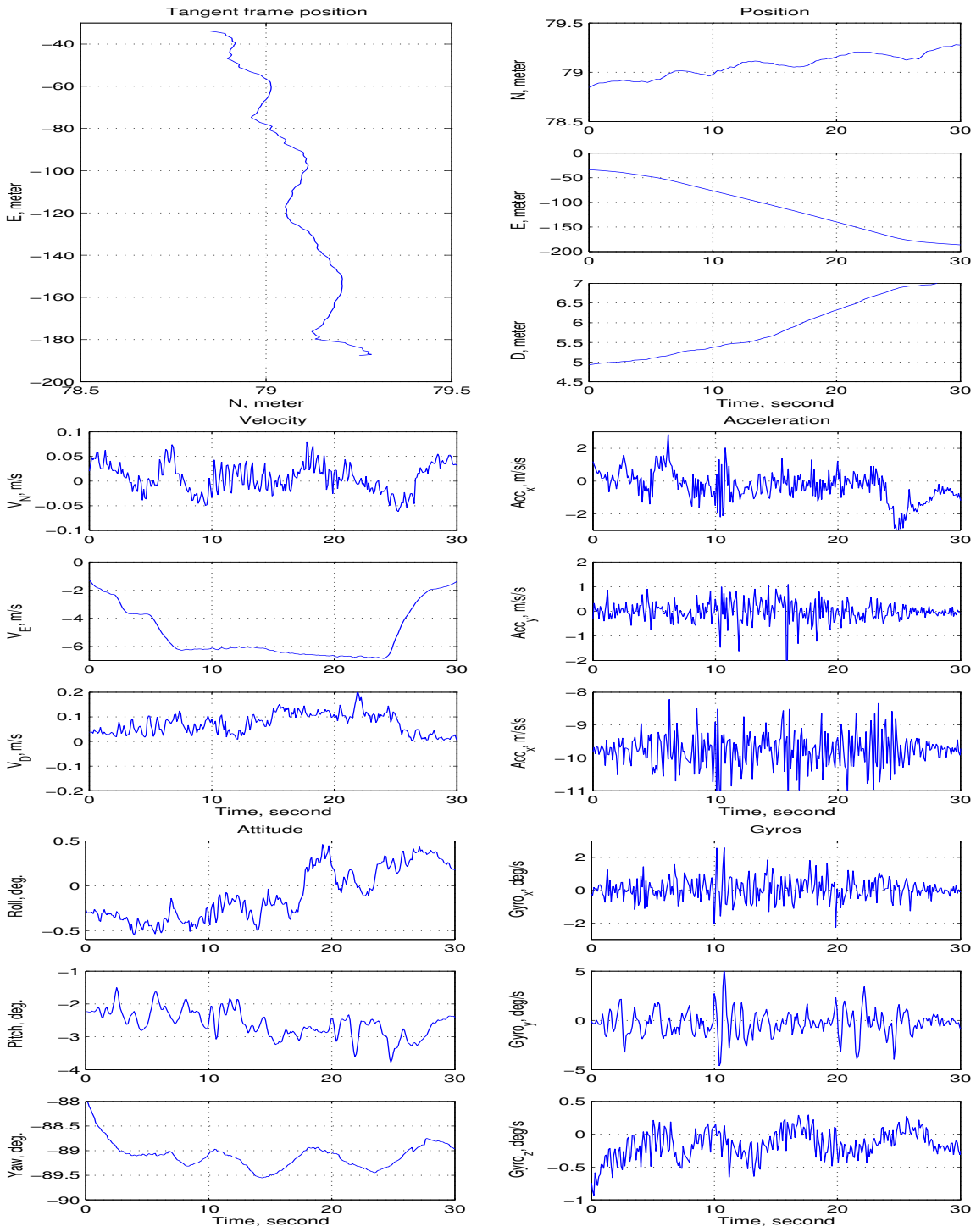

Figure 20: Absolute position, velocity, and angle for basic trajectory following using data from the two-antenna integer-resolved DGPS/INS. Top: Plot of the horizontal position data and time series plots of the position estimates. Middle: Time series plots of the velocity estimates and acceleration measurements. Bottom: Time series plots of the attitude estimates and angular rate measurements. This figure corresponds to Figure 21.

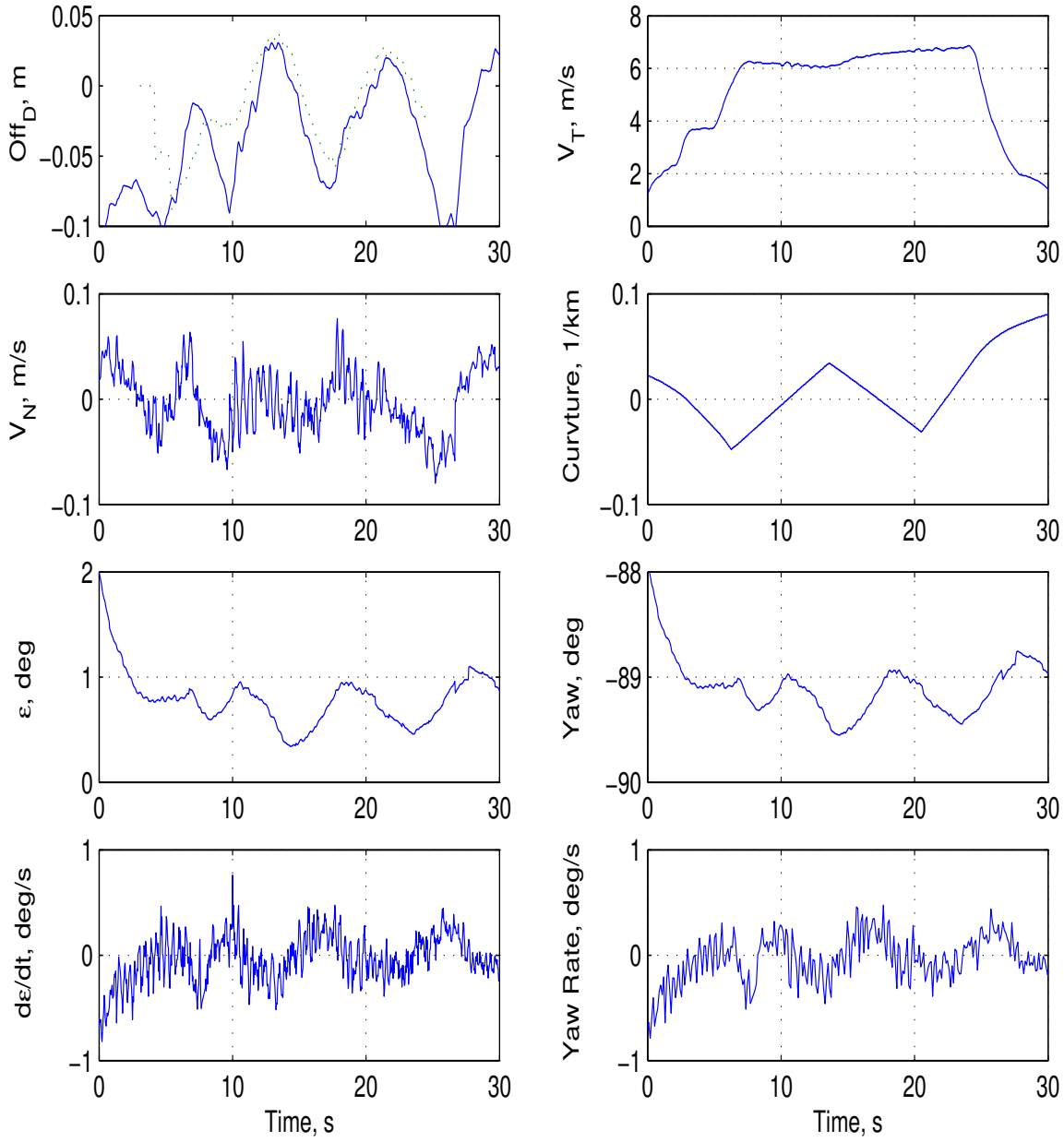

Figure 21: Results with two-antenna integer-resolved DGPS/INS based vehicle lateral control. The left column of plots shows the calculated trajectory relative control states from the two-antenna GPS/INS. The right column of plots shows related trajectory information. Top left: Time series plot of the off-trajectory distance as determined by two-antenna GPS/INS (solid) and the front magnetometer (dotted). Second left: two-antenna GPS/INS estimate of the velocity normal to the trajectory. Third left: two-antenna GPS/INS estimate of the heading error relative to the trajectory. Bottom left: Trajectory relative heading error rate estimate from two-antenna GPS/INS. Top right: two-antenna GPS/INS estimate of the velocity tangent to the trajectory. Second right: The trajectory curvature. Third right: The vehicle heading. Bottom right: The vehicle yaw rate. This figure corresponds to Figure 20.

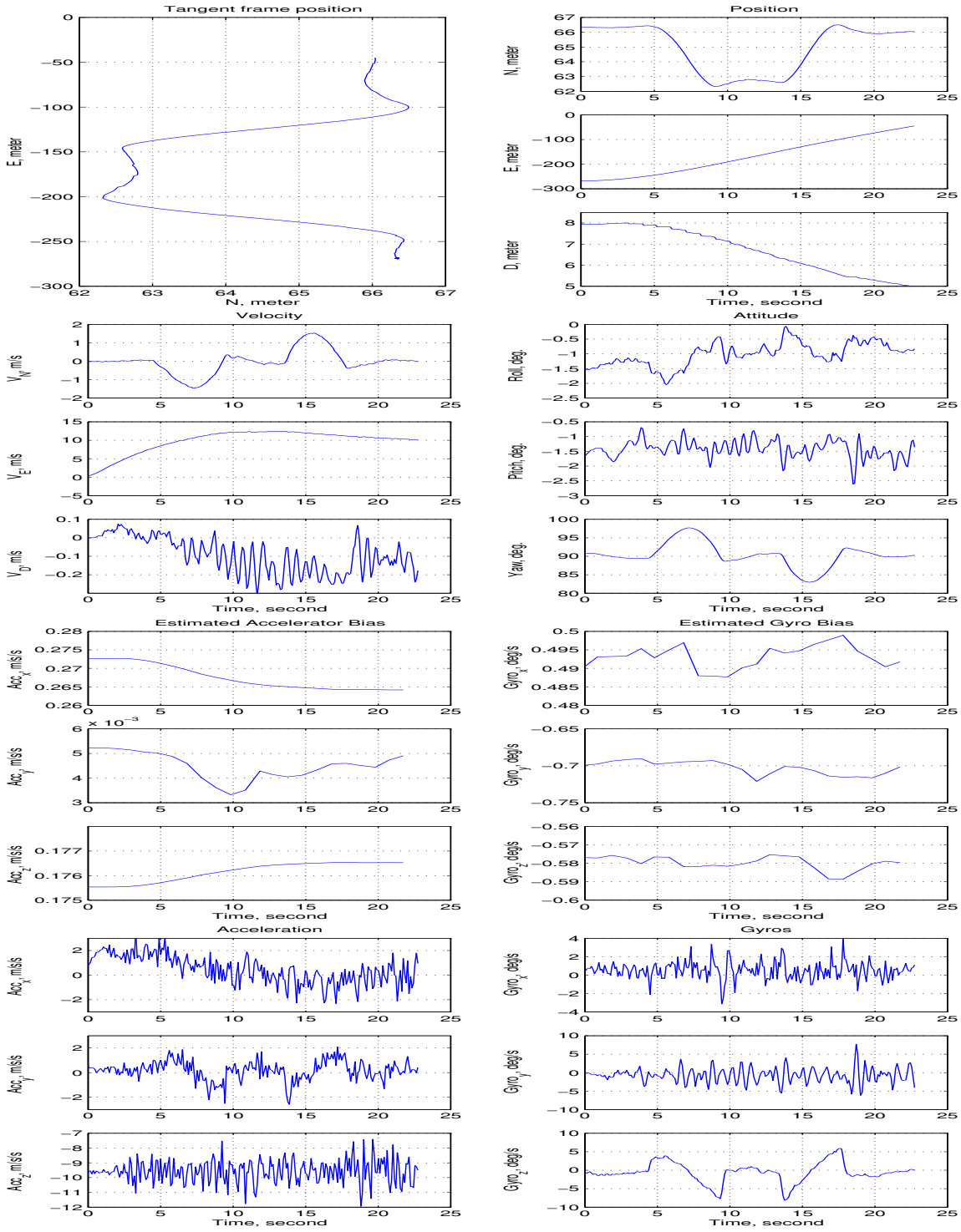

Figure 22: Absolute position, velocity, and angle for the lane-change maneuver using two-antenna integer-resolved DGPS/INS. Top: Plot of the horizontal position data and time series plots of the position estimates. Top second: Time series plots of the velocity estimates and attitude estimates. Top third: Time series plots of the acceleration and angular rate bias estimates. Bottom: Time series plots of the acceleration and angular rate measurement.

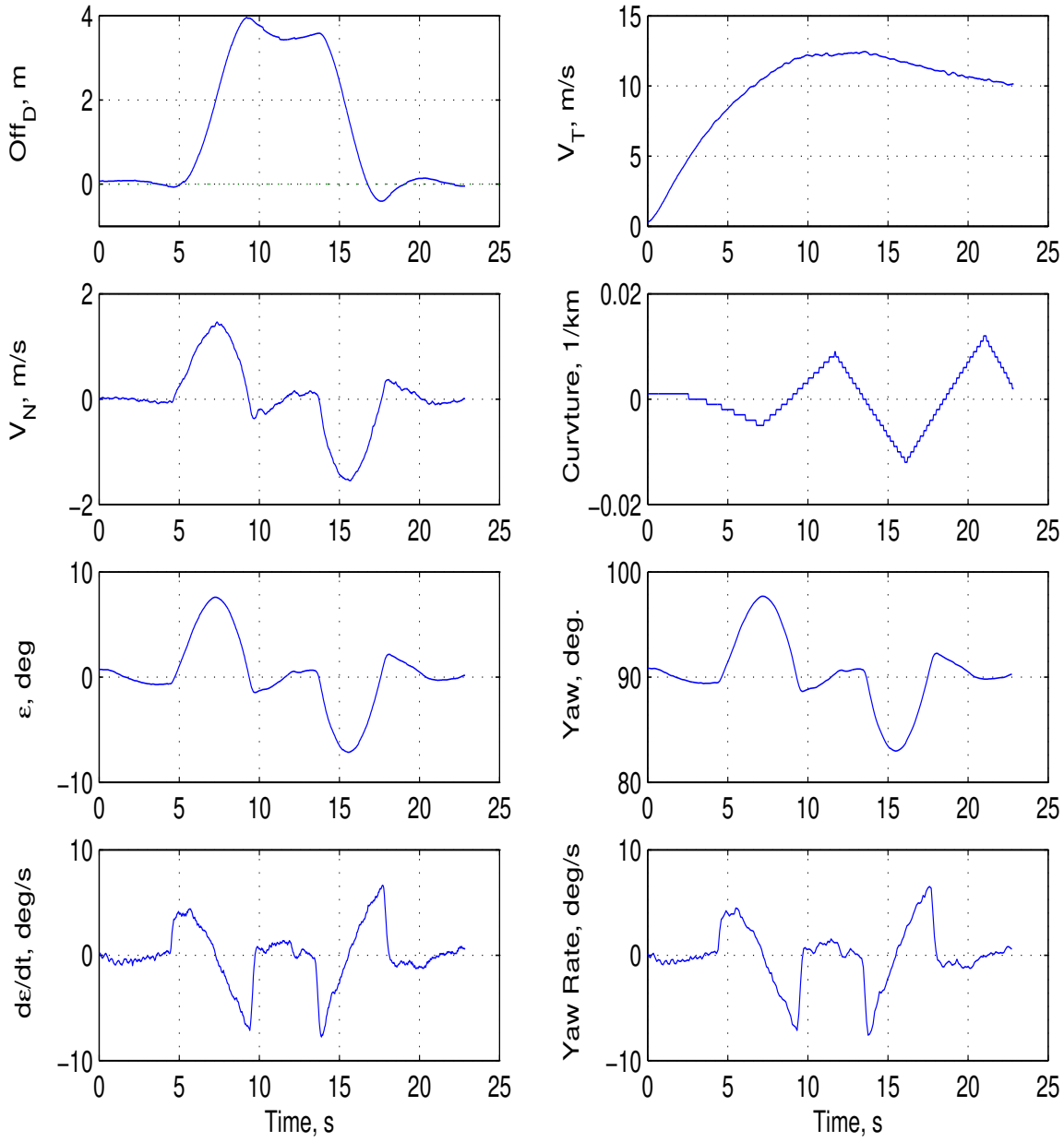

Figure 23: Trajectory relative control results with two-antenna integer-resolved DGPS/INS for a lane-change maneuver. The left column of plots shows the control states. The right column of plots shows related trajectory information. Top left: Time series plot of the off-trajectory distance as determined by two-antenna GPS/INS (solid) and the front magnetometer (dotted). Second left: two-antenna GPS/INS estimate of the velocity normal to the trajectory. Third left: two-antenna GPS/INS estimate of the heading error with respect to the trajectory. Bottom left: Heading error rate estimate from two-antenna GPS/INS. Top right: two-antenna GPS/INS estimate of the velocity tangent to the trajectory. Second right: The trajectory curvature. Third right: The vehicle heading. Bottom right: The vehicle yaw rate. This figure corresponds to Figure 22.

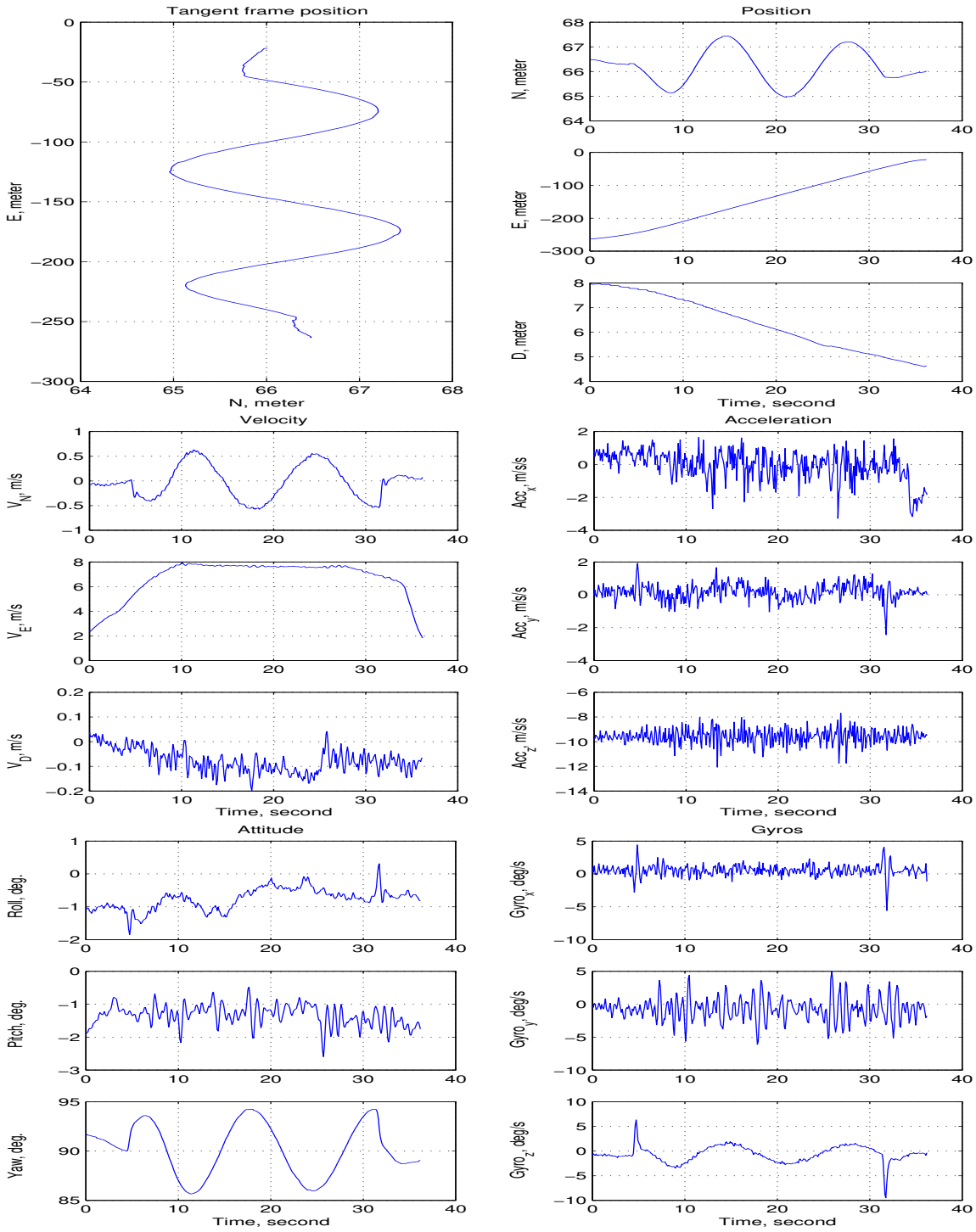

Figure 24: Absolute position, velocity, and angle for a sine-wave maneuver using two-antenna integer-resolved DGPS/INS. Top: Plot of the horizontal position data and time series plots of the position estimates. Middle: Time series plots of the velocity estimates and acceleration measurements. Bottom: Time series plots of the attitude estimates and angular rate measurements. This figure corresponds to Figure 25.

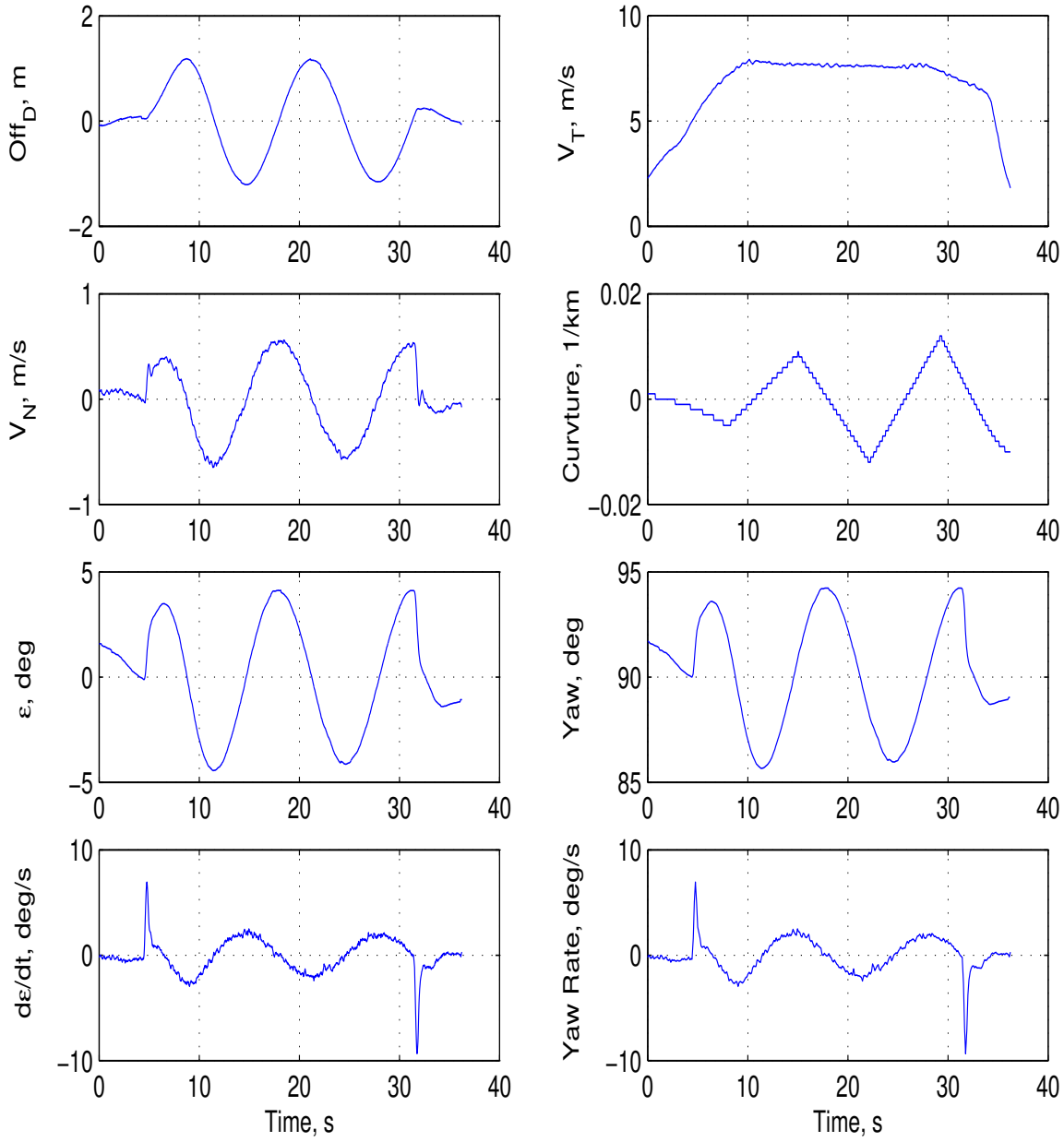

Figure 25: Trajectory relative control results for a two-antenna integer-resolved DGPS/INS based sine wave maneuver. The left column of plots shows the calculated control states from two-antenna GPS/INS. The right column of plots shows trajectory relative information. Top left: Time series plot of the off-trajectory distance as determined by two-antenna GPS/INS (solid) and the front magnetometer (dotted). Second left: two-antenna GPS/INS estimate of the velocity normal to the trajectory. Third left: two-antenna GPS/INS estimate of the heading error with respect to the trajectory. Bottom left: Heading error rate estimate from two-antenna GPS/INS. Top right: two-antenna GPS/INS estimate of the velocity tangent to the trajectory. Second right: The trajectory curvature. Third right: The vehicle heading. Bottom right: The vehicle yaw rate. This figure corresponds to Figure 24.

7 Conclusions

7.1 Magnetometer/GPS/INS

GPS/INS/Magnetometer attitude determination and navigation system was analyzed, designed, built and tested. This system used three different types of sensors to obtain observability of the full navigation state and triplicate sensor redundancy. The experimental results show that the accuracy of the position is at the centimeter level, the accuracy of the velocity is at the centimeter per second level, and the accuracy of the heading is at the tenth of a degree level as long as the vehicle is moving. Acceleration is *not* required for observability.

7.2 Two antenna/GPS/INS

The main contribution of this portion of the project is the design and analysis of a new method for determining vehicle attitude using only two GPS antennae and an INS. Previous methods for GPS based attitude determination required at least three antennae. In addition, to the theoretical analysis and design, this article has described a system integration and related vehicle control experiments.

The two-antenna GPS/INS attitude determination and navigation system was designed to achieve high performance at low cost. For example, the second GPS can be single frequency and the IMU is a low cost solid state instrument. The experimental results show that the accuracy of the position is 0.015 m (1 standard deviation). The accuracy of the velocity is 0.01 m/s (1 standard deviation). The accuracy of the attitude is 0.03 degree for the roll and pitch angles and 0.1 degree for the heading angle (1 standard deviation).

8 Future Research

The magnetometer/GPS/INS navigation system has been demonstrated several times to reliably perform lateral vehicle control. The control system used in these demonstrations is the controller originally designed to use the d and ϵ calculated by the magnetometer system, only the parameters were tuned. Improved performance could be obtained by modifying the control system to take advantage of the $\dot{d}$, $\dot{\epsilon}$, and accurate trajectory preview information available from the integated magnetometer/DCPGPS/INS system. The system also already provides the vehicle state information (i.e., the vehicle tangential velocity v_T see Appendix C) that is required to perform vehicle longitudinal control. It would be interesting to perform such a longitudinal control demonstration.

Path has also stated an interest in relative vehicle control. Control of the relative positions of vehicles requires accurate and reliable knowledge of relative vehicle position and velocity. The system described herein reliably provides *absolute* vehicle state information. Each vehicle in a platoon of vehicles equipped with the magnetometer, GPS, INS navigation system can determine its position *relative* to any other vehicles in the platoon by simple subtraction of the two vehicles' absolute state information. This process provides the full relative vehicle state (i.e., relative position, relative velocity, relative acceleration, relative attitude and heading, and relative angular rates). The use of the navigation system described herein for relative vehicle control would be an interesting project.

The analysis in [15] shows an INS built using a calibrated, but unaided solid state IMU similar to that used herein, can maintain 0.4 m position accuracy for approximately 15 seconds. The dominant source of this position error growth is integration of IMU measurement noise. As the analysis of Section 4.1 and experimental results of Section 6.1 show that the magnetometer measurements accurately compensate the INS position (to cm accuracy) and velocity in the (critically important) lateral direction. Therefore, the magnetometer aided INS would accurately maintain the vehicle lateral position even in tunnel or urban canyon situations when GPS satellites in the direction normal to the trajectory are temporarily unavailable. In such situations, it is interesting to analyze, develop, and test a system that feeds the magnetometer aided INS state to the GPS receiver to help it maintain phase lock to the satellite signals during temporary periods of satellite signal interruption. Such a project is currently starting at UCR with support from PATH.

9 Publications Resulting from this Project

The following articles have been published:

- Yang, Y. and Farrell, J. A., "Magnetometer and Carrier Phase DGPS aided INS," Institute of Navigation, National Technical Meeting 2001, Long Beach, 22-24 Jan. 2001.
- Yang, Y., Farrell, J. A., and Tan, H.-S. "Carrier Phase Differential GPS-aided INS based Vehicle Control," Institute of Navigation, National Technical Meeting 2001, Long Beach, 22-24 Jan. 2001.
- Yang, Y., Farrell, J. A., and Tan, H.-S., "GPS-aided INS based Control State Calculation for AHS," IEEE 2001 American Control Conference, June 2001.
- Yang, Y. "Tightly Integrated Attitude Determination Methods for Low-Cost Inertial Navigation: Two-Antenna GPS and GPS/Magnetometer," Ph.D. Dissertation, June 2001.

The following articles have been accepted for publication:

- Yang, Y., Farrell, J. A., "Two Antennae GPS and Low Cost INS Tight Integration for Attitude Determination", Institute of Navigation – GPS 2001, Salt Lake City, September 11-14.
- Yang, Y., Farrell, J. A., "Fast Ambiguity Resolution for GPS/IMU Attitude Determination", Institute of Navigation – GPS 2001, Salt Lake City, September 11–14.

The following articles have been submitted for review:

- Farrell, J., Tan, H.-S. and Yang, Y, "Carrier Phase GPS-aided INS based Vehicle Lateral Control," submitted ASME Journal of Dynamics Systems, Measurement, and Control, May 7, 2001, 39 m.s.
- Farrell, J., "State Estimation," submitted to the Electrical Engineering Handbook (Ed. W.-K. Chen), April 2001,20 m.s., Academic Press.

The following articles are in preparation:

- Yang, Y., Farrell, J. A., "Tightly Integrated Two-Antenna Carrier Phase GPS/INS Navigation System".
- Yang, Y., Farrell, J. A., "Carrier Phase GPS/INS/Magnetometer Tightly Integrated Navigation System".

References

[1] Britting, K. R., *Inertial Navigation Systems Analysis*, Wiley-Interscience, New York, 1971.

[2] Brown, R. G., "Integerated Navigation Systems and Kalman Filter: A Perspective," Journal of the institute of Navigation, Vol. 19(1), Winter 1972 – 1973, pp. 355-362.

[3] Brown, R. G., "Integrated Navigation Systems and Kalman Filtering: A Perspective," *Navigation: Journal of the Institute of Navigation*, Vol. 19 (1), Winter 1972-1973, pp. 355-362.

[4] Brown, R. G. and Y.C. Hwang, *Introduction to Random Signals and Applied Kalman Filtering*, 3rd ed. New York : J. Wiley, 1997.

[5] Cohen, C. E., *Attitude Determination Using GPS*, Ph.D. Dissertation, Dept. of Aeronautics and Astonautics, Standford Univ., Standford, CA, Dec. 1992.

[6] Cohen, C.E., Parkinson, B.W., and McNally, B.D., "Flight tests of attitude determination using GPS compared against an inertial navigation unit," Navigation. Journal of the Institute of Navigation, vol. 41, (no.1), Spring 1994. pp. 83-97.

[7] W. Cormier and R. Fenton, "On the Steering of Automated VehiclesA Velocity Adaptive Controller," *IEEE Trans. on Vehicular Technology*, Vol. 29, no.4, pp. 375-385, 1980.

[8] E. Dickmanns and B. Mysliwetz, "Recursive 3-D road and relative ego-state recognition," *IEEE Transactions on Pattern Analysis and Machine Intelligence*, Vol. 14, pp. 199-213, 1992.

[9] R. T. Dunlay, "Obstacle avoidance perception processing for the autonomous land vehicle," in Proceedings of the IEEE International Conference on Robotics and Automation, pp. 912-917, 1987.

[10] Farrell, J. A. and Barth, M., *The Global Positioning System and Inertial Navigation*, McGraw-Hill (ISBN-0-07-022045-X), 1999.

[11] Farrell, J. A. and Barth, M., "Integration of GPS-aided INS into AVCSS", California Path Research Report UCB-ITS-PRR-2000-22. August, 2000.

[12] Farrell, J. A. and Givargis. T., "Differential GPS Reference Station Algorithm: Design and Analysis" IEEE Transactions on Control Systems Technology. Vol. 8 (3), May 2000, pp. 519-531.

[13] Farrell, J. A. , Givargis., T. and Barth, M.,"Real-time Differential Carrier Phase GPS-Aided INS," IEEE Transactions on Control Systems Technology. Vol. 8 (4), July 2000, pp. 709-721.

[14] Farrell, J. A., Tan, H.-S. and Yang, Y, "Carrier Phase GPS-aided INS based Vehicle Lateral Control," submitted ASME Journal of Dynamics Systems, Measurement, and Control, May 7, 2001, 39 m.s.

[15] Farrell, J. A., "State Estimation," submitted to the Electrical Engineering Handbook (Ed. W.-K. Chen), , April 2001, 20 m.s., Academic Press.

[16] Farrell, J. L., *Integrated Aircraft Navigation*, Academic Press: New York, 1976.

[17] R. Fenton, G. Melocik, and K. Olson, "On the Steering of Automated Vehicles: Theory and Experiment," *IEEE Transactions of Automatic Control*, Vol. 21, no.3, pp. 306-315, 1976.

[18] R. Fenton and R. Mayhan, "Automated Highway Studies at The Ohio State UniversityAn Overview," *IEEE Trans. on Vehicular Technology*, Vol. 40, no.1, pp. 100-113, 1991.

[19] GPS Joint Program Office, *ICD-GPS-200: GPS Interface Control Document*, ARINC Research, 1997.

[20] A. Hanson, E. Riseman, and C. Weems, "Progress in computer vision at the University of Massachusetts," in DARPA Image Understanding Workshop, pp. 39-47, 1993.

[21] Hatch, R., "Instantaneous Ambiguity Resolution," Symposium No. 107, Kinematic Systems in Geodesy, Surveying and Remote Sensing, Banff, Canada, September 10–13, 1990, pp. 299–308, Springer–Verlag, New York, 1990.

[22] Hoffmann-Wellenhof, B., Lichtenegger, H. and Collins, J., *GPS: Theory and Practice*, 4rd ed.New York: Springer-Verlag, 1997.

[23] Kaplan, E. D. (ed.), *Understanding GPS, Principles and Applications*, Artech House Publishers (ISBN 0-89006-793-7), 1995.

[24] Kuan, Phipps, and Hsueh, "Autonomous Robotic Vehicle Road Following," *IEEE Transactions on Pattern Analysis and Machine Intelligence*, Vol. 10, pp. 648-658, 1988.

[25] Lefferts, E. J., Markley, F. L. and Dhuster, M. D., "Kalman Filtering for Spacecraft Attitude Estimation," Journal of Guidance, Control, and Dynamics, Vol. 5, 1982, pp. 417-429.

[26] R. Mayhan and R. Bishel, "A Two-Frequency Radar for Vehicle Automatic Lateral Control," *IEEE Trans. on Vehicular Technology*, Vol. 31, no.1, pp. 32-39, 1982.

[27] I. Masaki, Vision-Based Vehicle Guidance, New York: Springer-Verlag, 1992.

[28] Parkinson, B. and Spilker J. (ed.), *Global Positioning System: Theory and Practice*, Volumes I and II. Washington, DC: American Institute of Aeronautics and Astronautics, Inc., 1996.

[29] H. Schneidermann and M. Nashman, "Visual processing for autonomous driving," in IEEE Workshop on Applications of Computer Vision, Palm Springs, CA, pp. 164-171, 1992.

[30] S. Shladover, et al., "Automatic Vehicle Control Developments in the PATH Program," *IEEE Trans. on Vehicular Technology*, Vol. 40, no.1, pp. 114-130, 1991.

[31] C. Thorpe, et al, "Toward autonomous driving: the CMU Navlab", Part 1-Perception, *IEEE Expert*, Vol. 6, pp. 31-42, 1991.

[32] Titterton, D.H. and Weston, J.L., *Title Strapdown inertial navigation technology.* Peter Peregrinis Ltd. on behalf of the Institution of Electrical Engineers, c1997.

[33] Yang, Y., Farrell, J. A., and Barth, M., "High-Accuracy, High-Frequency Differential Carrier Phase GPS Aided Low-Cost INS " Proceeding of IEEE 2000 Position Location and Navigation Symposium, San Diego, CA, USA, 13-16 March 2000.

[34] Yang, Y., Farrell, J. A., and Tan, H.-S., "Carrier Phase Differential GPS-aided INS based Vehicle Control: Experiement Results," Institue of Navigation, NTM 2001, Long Beach, 22-24 Jan. 2001.

[35] Yang, Y., Farrell, J. A., and Tan, H.-S., "GPS-aided INS based Control State Calculation for AHS," IEEE 2001 American Control Conference, June 2001.

[36] Yang, Y., and Farrell, J. A., "Fast Ambiguity Resolution for GPS/IMU Attitude Determination", Institute of Navigation – GPS 2001, Salt Lake City, September 11–14.

[37] Yang, Y. "Tightly Integrated Attitude Determination Methods for Low-Cost Inertial Navigation: Two-Antenna GPS and GPS/Magnetometer," Ph.D. Dissertation, June 2001.

[38] Zhang, W., Parsons, R. E., and West, T.,"An Intelligent Roadway Reference System for Vehicle Lateral Guidance/Control," Proceeding of the 1990 American Control Conference, San Diegp, CA, USA, 23-25 May 1990, pp.281-286.

A Global Position System

The NAVSTAR (NAVigation System with Timing And Range) Global Positioning System (GPS) is a space-based, all-time, all-weather navigation system developed by the Department of Defense (DOD) to determine position, velocity, and time for a user that is on (or near) the earth [19, 22, 23, 28].

A.1 GPS Measurement Model

For civilian GPS receivers, three types of GPS measurements are available for each correlator channel with a locked GPS satellite signal. They are pseudorange and integrated carrier phase for L1 and L2, and Doppler. The pseudorange and carrier phase model equations are (from [10]):

$$\begin{aligned}\tilde{\rho}^{(i)} &= ((X^{(i)}-x)^2+(Y^{(i)}-y)^2+(Z^{(i)}-z)^2)^{0.5}+c\Delta t_r \\ &\quad +c\Delta t_{sv}^{(i)}+c\Delta t_{trop}^{(i)}+c\Delta t_{ion}^{(i)}+E^{(i)}+MP^{(i)}+\eta^{(i)} \end{aligned} \tag{73}$$

$$\begin{aligned}\tilde{\phi}^{(i)} &= \frac{1}{\lambda}\Big[((X^{(i)}-x)^2+(Y^{(i)}-y)^2+(Z^{(i)}-z)^2)^{0.5}+c\Delta t_r \\ &\quad +c\Delta t_{sv}^{(i)}+c\Delta t_{trop}^{(i)}-c\Delta t_{ion}^{(i)}+E^{(i)}+mp^{(i)}+\beta^{(i)}\Big]-N^{(i)} \end{aligned} \tag{74}$$

and the Doppler measurement (the carrier phase time differential) is

$$\tilde{D}^{(i)}(t)=\frac{d\tilde{\phi}^{(i)}(t)}{dt} \tag{75}$$

where $\tilde{\rho}$ is the measured pseudorange in meters, $\tilde{\phi}$ is the measured carrier phase in cycles, $\tilde{D}(t)$ is the measured Doppler velocity at time t, (X,Y,Z) is the position of a satellite in ECEF coordinates, (x,y,z) is the position of the GPS receiver antenna in ECEF coordinates, Δt_r is the receiver clock bias, Δt_{sv} is the clock bias of the satellite, Δt_{trop} is a measure of the tropospheric delay, Δt_{ion} is a measure of the ionospheric delay with different sign for pseudorange and carrier phase, E represents error in the broadcast ephemeris data, MP represents multipath error on the pseudorange signal, mp represents phase multipath error, η represents receiver range tracking error, β represents receiver phase tracking error, N is the integer ambiguity of carrier phase, $\lambda=\frac{c}{f}$, c is the speed of light and f is the carrier microwave frequency of L1 or L2. The $()^{(i)}$ notation refers the quantity in parenthesis to satellite i. The Navigation Ephemeris data, defined in [19], is used to calculate GPS satellite orbits, clock corrections, and determine the satellite position in ECEF coordinates.

The error terms $c\Delta t_{sv}^{(i)}$, $c\Delta t_{trop}^{(i)}$, $c\Delta t_{ion}^{(i)}$ and $E^{(i)}$ can be canceled, for users in a local area, by differential operation as described in Section A.3. The multipath error and GPS receiver noise of carrier phase are much smaller (cm's and mm's, respectively) than those of the pseudorange (m's and decimeters, respectively).

Therefore, there the phase measurement is a much cleaner measurement than the pseudorange. However, for the phase measurement, there is a unknown (usually large) integer constant bias N. This integer phase ambiguity is the whole number of carrier phase cycles between the receiver and the satellite at an initial measurement time. To make use of carrier phase measurement as a range estimate, this integer ambiguity must be correctly estimated and removed. The details of this integer ambiguity resolution algorithm are described in [10, 36, 37].

A.2 Linearized measurement equation

If an estimate of the GPS receiver position $\hat{\mathbf{x}}=(\hat{x},\hat{y},\hat{z})$ is available, then the corresponding estimated range between the GPS receiver and the i-th satellite is calculated by $\hat{R}^{(i)}=((X^{(i)}-\hat{x})^2+(Y^{(i)}-\hat{y})^2+(Z^{(i)}-\hat{z})^2)^{0.5}$, where the satellite position $(X^{(i)},Y^{(i)},Z^{(i)})$ is calculated using the navigation ephemeris data. Linearizing the GPS measurement eqns. (73–75) yields:

$$\tilde{\rho}^{(i)}-\hat{R}^{(i)} = \mathbf{h}^{(i)}(\mathbf{x}-\hat{\mathbf{x}})+c\Delta t_r+\chi^{(i)}+c\Delta t_{ion}^{(i)}+MP^{(i)}+\eta^{(i)}+h.o.t.'s \tag{76}$$

$$\tilde{\phi}^{(i)}\lambda-\hat{R}^{(i)} = \mathbf{h}^{(i)}(\mathbf{x}-\hat{\mathbf{x}})+c\Delta t_r+\chi^{(i)}-c\Delta t_{ion}^{(i)}+mp^{(i)}+\beta^{(i)}-N^{(i)}\lambda+h.o.t.'s \tag{77}$$

and the derivative of eqn. (77) with respect to t is (with assumption $\frac{\partial \mathbf{h}^{(i)}}{\partial t}\approx 0$):

$$\tilde{D}^{(i)}(t)\lambda-\mathbf{h}^{(i)}(\hat{\mathbf{v}}_r-\hat{\mathbf{v}}_{sv}^{(i)}) = \mathbf{h}^{(i)}(\mathbf{v}_r-\hat{\mathbf{v}}_r^{(i)})+\frac{\partial(c\Delta t_r)}{\partial t}+\frac{\partial\chi^{(i)}}{\partial t}-\frac{\partial(c\Delta t_{ion}^{(i)})}{\partial t}$$

$$+\frac{\partial mp^{(i)}}{\partial t}+\frac{\partial \beta^{(i)}}{\partial t}+h.o.t.'s \tag{78}$$

where $\mathbf{x}$ is the actual position of then GPS receiver, $\mathbf{v}_r$ is the true velocity of the GPS receiver, $\hat{\mathbf{v}}_r$ is the calculated velocity of the GPS receiver, $\hat{\mathbf{v}}_{sv}^{(i)}$ is the calculated velocity of satellite i, $h.o.t.'s$ represents higher order terms in the expansion,

$$\chi^{(i)}=c\Delta t_{sv}^{(i)}+c\Delta t_{trop}^{(i)}+E^{(i)} \tag{79}$$

is the common error that can be canceled in a local region by Differential GPS,

$$\mathbf{h}^{(i)}=\left[\begin{array}{ccc}\frac{\partial\rho^{(i)}}{\partial x} & \frac{\partial\rho^{(i)}}{\partial y} & \frac{\partial\rho^{(i)}}{\partial z}\end{array}\right]\Big|_{(\hat{x},\hat{y},\hat{z})} \tag{80}$$

is the unit vector from the satellite to the GPS receiver:

$$\begin{aligned}\frac{\partial\rho^{(i)}}{\partial x} &= \frac{-(X^{(i)}-x)}{((X^{(i)}-x)^2+(Y^{(i)}-y)^2+(Z^{(i)}-z)^2)^{0.5}}\\ \frac{\partial\rho^{(i)}}{\partial y} &= \frac{-(Y^{(i)}-y)}{((X^{(i)}-x)^2+(Y^{(i)}-y)^2+(Z^{(i)}-z)^2)^{0.5}}\\ \frac{\partial\rho^{(i)}}{\partial z} &= \frac{-(Z^{(i)}-z)}{((X^{(i)}-x)^2+(Y^{(i)}-y)^2+(Z^{(i)}-z)^2)^{0.5}}.\end{aligned}$$

A.3 GPS Differential Operation

To achieve significant accuracy improvements, differential operation can be used to cancel the errors between GPS receivers. For differential GPS with a short baseline (within 20 miles), especially for attitude determination with baseline length within several meters, $c\Delta t_{sv}^{(i)}$, $c\Delta t_{trop}^{(i)}$, $c\Delta t_{ion}^{(i)}$ and $E^{(i)}$ are nearly the same between the two receivers. These errors comprise the common-mode error. For differential GPS with long baseline or at a different altitude, $c\Delta t_{trop}^{(i)}$, $c\Delta t_{ion}^{(i)}$, and $E^{(i)}$ need to be modeled and estimated [10, 28]. The details are not described here.

Differential GPS involves a reference GPS receiver, rover GPS receivers, and a communication mechanism between the reference GPS receiver to the rover GPS receivers. The vector between two GPS antennae is called the **baseline** formed by these two GPS antennae.

GPS differential operation can be divided in two cases based on the characteristics of the reference receiver antenna. The reference receiver (and antenna) will be referred to in the following as the **base** or $\mathbf{GPS_2}$. Other receiver/antenna pairs, possibly moving with respect to the base will be referred to as **rovers** or $\mathbf{GPS_1}$.

1. **The base location is accurately known**[5]: In this situation, the known position and velocity of the **base** can be used to calculate the error corrections of each satellite. These corrections are broadcast to **rovers**. The rover receivers use the broadcast corrections to remove common mode errors from each satellite measurement.

   The GPS pseudorange, carrier phase, and Doppler corrections calculated at the base using eqns. (76 – 78) are

$$\Delta_{\rho}^{(i)} = c\Delta t_{r_B}+\chi_B^{(i)}+c\Delta t_{ion}^{(i)}+MP_B^{(i)}+\eta_B^{(i)} \tag{81}$$

$$\Delta_{\phi}^{(i)} = c\Delta t_{r_B}+\chi_B^{(i)}-c\Delta t_{ion}^{(i)}+n_{\phi_B}^{(i)}-N_B^{(i)}\lambda \tag{82}$$

$$\Delta_{D(t)}^{(i)} = -\mathbf{h}^{(i)}\mathbf{v}^{(i)}{}_{sv}+\frac{\partial(c\Delta t_{r_B})}{\partial t}+\frac{\partial\chi^{(i)}}{\partial t}-\frac{\partial(c\Delta t_{ion}^{(i)})}{\partial t}+\frac{\partial n_{\phi_B}^{(i)}}{\partial t}. \tag{83}$$

   where the notation $()_B$ refers the quantity in the parenthesis to the base station receiver. These quantities are the basic calculated correction results for the differential GPS reference stations that are widely used in applications, such as the single GPS base station, the Local Area Augmentation System (LAAS), and the Wide Area Augmentation System (WAAS). The calculation approaches are not necessarily the same. The details of the base station design and implementation for this project are discussed in [12].

   The single and double difference DGPS approaches are reviewed below.

[5] In this approach, the base location is usually fixed. However, this is not a requirement of the method. Instead, the base station is typically fixed as this simplifies the problem of accurately determining the base location (e.g., by surveying).

(a) **Single Difference.** Using the results of eqns. (81–83) as corrections and substituting them into eqns. (76–78) yields the linearized single difference GPS measurements at the rover as:

$$\begin{aligned}
\triangle\rho^{(i)} - \hat{R}^{(i)} &= \mathbf{h}^{(i)}\Delta\mathbf{x} + c\Delta t_{r_{RB}} + MP_{RB}^{(i)} + n_{\rho_{RB}}^{(i)} && (84)\\
\triangle\phi^{(i)}\lambda - \hat{R}^{(i)} &= \mathbf{h}^{(i)}\Delta\mathbf{x} + c\Delta t_{r_{RB}} + n_{\phi_{RB}}^{(i)} - N_{RB}^{(i)}\lambda && (85)\\
\triangle D^{(i)}\lambda - \mathbf{h}^{(i)}\hat{\mathbf{v}}_r &= \mathbf{h}^{(i)}\Delta\mathbf{v} + \frac{\partial(c\Delta t_{r_{RB}})}{\partial t} + n_{D_{RB}}^{(i)} && (86)
\end{aligned}$$

where

$$\begin{aligned}
\triangle\rho^{(i)} &= \tilde{\rho}_R^{(i)} - \Delta_\rho^{(i)},\\
\triangle\phi^{(i)} &= \tilde{\phi}_R^{(i)} - \Delta_\phi^{(i)}/\lambda,\\
\triangle D^{(i)}\lambda &= \tilde{D}_R^{(i)}(t)\lambda - \Delta_{D(t)}^{(i)},
\end{aligned}$$

with $\Delta\mathbf{x} = \mathbf{x} - \hat{\mathbf{x}}$, $\Delta\mathbf{v} = \mathbf{v}_r - \hat{\mathbf{v}}_r$, the notation $()_R$ refers the quantity in the parenthesis to the rover GPS receiver, the notation $()_{RB}$ refers the quantity in the parenthesis to the difference between the base and the rover GPS receivers, $n_{\rho_{RB}}^{(i)}$ is the single difference pseudorange noise and high order expansion term error, $n_{\phi_{RB}}^{(i)}$ is the single difference carrier phase noise, multipath error, and high order expansion terms error, and $n_{D_{RB}}^{(i)}$ is the single difference velocity error including the GPS receiver noise, multipath error, and the high order expansion terms. Eqn. (84) to eqn. (86) can be used to calculate $\mathbf{\Delta x}$ and $\mathbf{\Delta v}$. This requires estimation of the receiver clock bias and drift rate. Note that $\mathbf{\Delta x}$ and $\mathbf{\Delta v}$ can be used to correct $\mathbf{x} = \hat{\mathbf{x}} - \Delta\mathbf{x}$ and $\mathbf{v} = \hat{\mathbf{v}} - \Delta\mathbf{v}$, which are the *absolute* position and velocity of the rover.

(b) **Double Difference.** To implement the double difference approach, the rover selects a common satellite[6] j and subtracts satellite j's single difference GPS measurements from the measurements of all the other satellites. Therefore, the double difference measurements at the rover are calculated as:

$$\begin{aligned}
\nabla\triangle\rho^{(ij)} - \nabla\hat{R}^{(ij)} &= \mathbf{h}^{(ij)}\Delta\mathbf{x} + MP_{RB}^{(ij)} + n_{\rho_{RB}}^{(ij)} && (87)\\
\nabla\triangle\phi^{(ij)}\lambda - \nabla\hat{R}^{(ij)} &= -N_{RB}^{(ij)}\lambda + \mathbf{h}^{(ij)}\Delta\mathbf{x} + n_{\phi_{RB}}^{(ij)} && (88)\\
\nabla\triangle D^{(ij)}\lambda &= \mathbf{h}^{(ij)}\mathbf{v}_r + n_{D_{RB}}^{(ij)} && (89)
\end{aligned}$$

where

$$\begin{aligned}
\nabla\triangle\rho^{(ij)} &= (\tilde{\rho}_R^{(i)} - \Delta_\rho^{(i)}) - (\tilde{\rho}_R^{(j)} - \Delta_\rho^{(j)}),\\
\nabla\triangle\phi^{(ij)} &= (\tilde{\phi}_R^{(i)} - \Delta_\phi^{(i)}/\lambda) - (\tilde{\phi}_R^{(j)} - \Delta_\phi^{(j)}/\lambda),\\
\nabla\triangle D^{(ij)}\lambda &= (\tilde{D}_R^{(i)}(t)\lambda - \Delta_{D(t)}^{(i)}) - (\tilde{D}_R^{(j)}(t)\lambda - \Delta_{D(t)}^{(j)}),\\
\nabla\hat{R}^{(ij)} &= \hat{R}^{(i)} - \hat{R}^{(j)},
\end{aligned}$$

with $\mathbf{h}^{(ij)} = \mathbf{h}^{(i)} - \mathbf{h}^{(j)}$, the notation $()^{(ij)}$ refers to the quantity in parenthesis to the difference between the satellite i and j.

The advantage of double differential GPS is that the base and rover clock bias and drift rates have been removed. Therefore, these terms need not be estimated. The disadvantage is that the multipath error and the GPS receiver noise between different measurements are now correlated. Note that $\mathbf{\Delta x}$ and $\mathbf{\Delta v}$ can be used to correct $\mathbf{x} = \hat{\mathbf{x}} - \Delta\mathbf{x}$ and $\mathbf{v} = \hat{\mathbf{v}} - \Delta\mathbf{v}$, which are the *absolute* position and velocity of the rover.

2. **The reference location is unknown**[7]: In this situation, the vector of the baseline formed by the antenna of $\mathbf{GPS_1}$ and $\mathbf{GPS_2}$ is calculated. When $\mathbf{GPS_1}$ and $\mathbf{GPS_2}$ are mounted on different vehicles, this baseline represents the relative position between the vehicles. When $\mathbf{GPS_1}$ and $\mathbf{GPS_2}$ are rigidly mounted to a single vehicle, the baseline can be used to determine the vehicle attitude.

[6] To achieve small multipath error, the common satellite is usually selected to have high elevation angle.
[7] The reference location may not be accurately known, for example, because it is moving.

Differencing measurements between $\mathbf{GPS_1}$ and $\mathbf{GPS_2}$ yields

$$\begin{aligned}
\triangle\rho_{12}^{(i)} &= \mathbf{h}^{(i)}\mathbf{x}_{12} + c\Delta t_{r_{12}} + MP_{12}^{(i)} + n_{\rho_{12}}^{(i)} && (90)\\
\triangle\phi_{12}^{(i)}\lambda &= \mathbf{h}^{(i)}\mathbf{x}_{12} + c\Delta t_{r_{12}} + n_{\phi_{12}}^{(i)} - N_{12}^{(i)}\lambda && (91)\\
\triangle D_{12}^{(i)}\lambda &= \mathbf{h}^{(i)}\mathbf{v}_{r_{12}} + \frac{\partial(c\Delta t_{r_{12}})}{\partial t} + n_{D_{12}}^{(i)} && (92)
\end{aligned}$$

where

$$\begin{aligned}
\triangle\rho_{12}^{(i)} &= \tilde{\rho}_1^{(i)} - \tilde{\rho}_2^{(i)},\\
\triangle\phi_{12}^{(i)} &= \tilde{\phi}_1^{(i)} - \tilde{\phi}_2^{(i)},\\
\triangle D_{12}^{(i)} &= \tilde{D}_1^{(i)}(t) - \tilde{D}_2^{(i)}(t),
\end{aligned}$$

with $\mathbf{x}_{12} = \mathbf{x}_1 - \mathbf{x}_2$, the notation $()_{12}$ refers the quantity in the parenthesis to the difference between the $\mathbf{GPS_1}$ and the reference $\mathbf{GPS_2}$. Note that all common mode errors have been removed.

Subtracting the measurements of a common satellite from all other satellites yields the double difference measurements:

$$\begin{aligned}
\nabla\triangle\rho_{12}^{(ij)} &= \mathbf{h}^{(ij)}\mathbf{x}_{12} + MP_{12}^{(ij)} + n_{\rho_{12}}^{(ij)} && (93)\\
\nabla\triangle\phi_{12}^{(ij)}\lambda &= \mathbf{h}^{(ij)}\mathbf{x}_{12} + n_{\phi_{12}}^{(ij)} - N_{12}^{(ij)}\lambda && (94)\\
\nabla\triangle D_{12}^{(ij)}\lambda &= \mathbf{h}^{(ij)}\mathbf{v}_{r_{12}} + n_{D_{12}}^{(ij)} && (95)
\end{aligned}$$

where

$$\begin{aligned}
\nabla\triangle\rho_{12}^{(ij)} &= \Delta\rho_{12}^{(i)} - \Delta\rho_{12}^{(j)},\\
\nabla\triangle\phi_{12}^{(ij)} &= \Delta\phi_{12}^{(i)} - \Delta\phi_{12}^{(j)},\\
\nabla\triangle D_{12}^{(ij)} &= \Delta D_{12}^{(i)}(t) - \Delta D_{12}^{(j)}(t).
\end{aligned}$$

The advantage of double differential GPS is that the clock bias and drift of both receivers is canceled. The disadvantage is that the double difference measurement noise are larger than those of single difference GPS and these errors are is now correlated between measurements.

If $\mathbf{x_1}$ and $\mathbf{x_2}$ can both change freely (i.e. two vehicles), this approach allows calculation of their *relative* position and velocity. If the two antennae are rigidly attached to a vehicle, then $\mathbf{x_1} - \mathbf{x_2}$ can only change orientation. Therefore, this approach allows attitude determination.

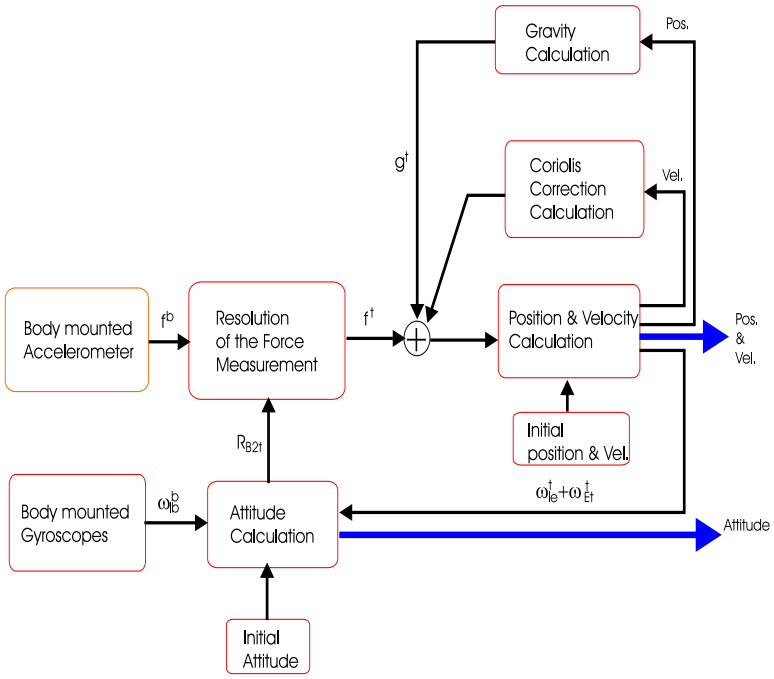

Figure 26: Strapdown Inertial Navigation System in the Tangent Frame

B Inertial Navigation System

Inertial Navigation Systems (INS) [1, 10, 16] have been developed and are used in many applications for control, guidance, and navigation. Such systems are capable of providing the vehicle state (i.e., position, velocity, acceleration, attitude, angular rate) at high rates suitable for real-time applications (e.g., control). An INS system integrates the differential equations describing the system dynamics for a short period of time by using high rate data from a set of inertial instruments. During this integration process, the error variance of the navigation states increases primarily due to the sensor noise and from sensor calibration and alignment errors.

There are two categories of INS: stabilized platform and the strapdown. A strapdown INS in the tangent frame was developed for this project due to its lower size, power, and cost requirements relative to a stabilized platform approach. This section summarizes the strapdown tangent plane INS which is used for both INS processing and GPS/INS integration.

B.1 INS Processing

The strapdown INS tangent frame mechanization is shown in Figure 26. The algorithms of the strapdown INS are attitude calculation, force transformation, gravity calculation, Coriolis correction calculation, and tangent frame position and velocity integration. These algorithms are described below using the variable definitions specified in Table 3.

The basic equation for attitude integration is

$$\dot{\mathbf{R}}_{\mathbf{b2t}} = \mathbf{R}_{\mathbf{b2t}} \Omega^b_{tb} \tag{96}$$

where $\mathbf{R_{b2t}}$ is the rotation matrix from body frame to tangent frame and Ω^b_{tb} is the skew symmetric matrix representation of $\omega^{\mathbf{b}}_{\mathbf{tb}} = [\omega_x, \omega_y, \omega_z]^T$, which is the body rotation rate vector with respect to the tangent frame expressed in the body frame. Two alternative approaches to integrating the attitute, Euler angles and quaternions, are discussed in [10].

The accelerometers measure the body frame acceleration with respect to the inertial frame represented in the body frame. The tangent plane specific force vector is calculated from accelerometer measurements as:

$$\begin{bmatrix} f_N \\ f_E \\ f_D \end{bmatrix} = \mathbf{R}_{b2t} \left(\begin{bmatrix} f_u \\ f_v \\ f_w \end{bmatrix} - \begin{bmatrix} b_u \\ b_v \\ b_w \end{bmatrix} \right)$$

Variable	Definition
(n, e, d)	North, east, and down position
(v_N, v_E, v_D)	North, east, and down velocity
(u, v, w)	Vehicle frame velocity
(f_N, f_E, f_D)	North, east, and down force
(f_u, f_v, f_w)	Vehicle frame specific force
g	Local vertical component gravity
ω_{ie}	Earth inertial angular rate
λ	Latitude
Φ	Longitude
(ϕ, θ, ψ)	Tangent plane vehicle attitude
	ϕ = roll, θ = pitch, ψ = yaw
(p, q, r)	Vehicle frame inertial rotation rate
(b_u, b_v, b_w)	Vehicle frame accelerometer bias
(b_p, b_q, b_r)	Vehicle frame gyro bias

Table 3: Variable Definitions

where $\mathbf{R}_{b2t}$ is the solution of eqn. (96) and $[b_u, b_v, b_w]$ is the estimated accelerometer bias vector. The time derivative of the velocity in the tangent frame has the relationship [1, 10]:

$$\begin{bmatrix} \dot{v}_N \\ \dot{v}_E \\ \dot{v}_D \end{bmatrix} = \begin{bmatrix} 0 & -2(\omega_{ie}\sin\lambda) & 0 \\ 2\omega_{ie}\sin\lambda & 0 & 2\omega_{ie}\cos\lambda \\ 0 & -2\omega_{ie}\cos\hat{\lambda} & 0 \end{bmatrix} \begin{bmatrix} v_N \\ v_E \\ v_D \end{bmatrix} + \begin{bmatrix} f_N \\ f_E \\ f_D \end{bmatrix} + \begin{bmatrix} g_x \\ g_y \\ g_z \end{bmatrix} + \begin{bmatrix} \frac{1}{R_\lambda + h} v_N v_D - \frac{\tan\lambda}{(R_\Phi + h)} v_E^2 \\ \frac{\tan\lambda}{(R_\Phi + h)} v_N v_E + \frac{1}{(R_\Phi + h)} v_E v_D \\ -\frac{1}{(R_\Phi + h)} v_E^2 - \frac{1}{R_\lambda + h} v_D^2 \end{bmatrix}. \quad (97)$$

Eqn. (97) is the basic equation for the tangent plane velocity integration. Position in the tangent frame is calculated by integrating the velocity with respect to time.

B.2 Tangent Plane INS Error Equations

For error analysis and online error estimation via Kalman filtering aided by differential GPS, it is necessary to linearize the INS equations along the vehicle trajectory. The linearized error equations derived in [1, 10] are summarized below.

The linearized dynamic INS error equation is:

$$\begin{bmatrix} \delta\dot{\mathbf{p}} \\ \delta\dot{\mathbf{v}} \\ \delta\dot{\rho} \end{bmatrix} = \begin{bmatrix} \mathbf{F_{pp}} & \mathbf{F_{pv}} & \mathbf{F_{p\rho}} \\ \mathbf{F_{vp}} & \mathbf{F_{vv}} & \mathbf{F_{v\rho}} \\ \mathbf{F_{\rho p}} & \mathbf{F_{\rho v}} & \mathbf{F_{\rho\rho}} \end{bmatrix} \begin{bmatrix} \delta\mathbf{p} \\ \delta\mathbf{v} \\ \delta\rho \end{bmatrix} + \begin{bmatrix} e_{\mathbf{p}} \\ e_{\mathbf{v}} \\ e_\rho \end{bmatrix} + \begin{bmatrix} \omega_{\mathbf{p}} \\ \omega_{\mathbf{v}} \\ \omega_\rho \end{bmatrix}. \quad (98)$$

All error quantities are defined to be the actual values minus the calculated (or measured) values (i.e., $\delta x = x - \hat{x}$).

For the tangent plane implementation, three components of the nominal error states are defined as:

$$\begin{array}{lll} \delta\mathbf{p} & = [\delta n, \delta e, \delta d]^T & \text{is the tangent frame position error,} \\ \delta\mathbf{v}^n & = [\delta v_N, \delta v_E, \delta v_D]^T & \text{is the tangent frame velocity error} \\ \delta\rho^n & = [\delta\epsilon_N, \delta\epsilon_E, \delta\epsilon_D]^T & \text{is the small attitude angle error.} \end{array}$$

The matrix F of eqn. (98) is

$$\mathbf{F} = \begin{bmatrix} 0 & 0 & 0 & 1 & 0 & 0 & 0 & 0 & 0 \\ 0 & 0 & 0 & 0 & 1 & 0 & 0 & 0 & 0 \\ 0 & 0 & 0 & 0 & 0 & 1 & 0 & 0 & 0 \\ \frac{-2\omega_n v_E}{R} & 0 & 0 & 0 & 2\omega_D & 0 & 0 & f_D & -f_E \\ \frac{2}{R}(v_N\omega_N + v_D\omega_D) & 0 & 0 & -2\omega_D & 0 & 2\omega_N & -f_D & 0 & f_N \\ \frac{-2v_E\omega_D}{R} & 0 & \frac{-2\mu}{R^3} & 0 & -2\omega_N & 0 & f_E & -f_N & 0 \\ \frac{\omega_D}{R} & 0 & 0 & 0 & 0 & 0 & 0 & \omega_D & -\omega_E \\ 0 & 0 & 0 & 0 & 0 & 0 & -\omega_D & 0 & \omega_N \\ \frac{-\omega_N}{R} & 0 & 0 & 0 & 0 & 0 & \omega_E & -\omega_N & 0 \end{bmatrix} \quad (99)$$

with $\omega_N = \omega_{ie}\cos\lambda$ and $\omega_D = -\omega_{ie}\sin\lambda$. Therefore,

$$\mathbf{F_{pp}} = \mathbf{F_{p\rho}} = \mathbf{F_{\rho v}} = \mathbf{0}_{3\times 3}, \quad \mathbf{F_{pv}} = \mathbf{I}_{3\times 3},$$

$$\mathbf{F_{vp}} = \begin{bmatrix} \frac{-2\omega_n v_E}{R} & 0 & 0 \\ \frac{2}{R}(v_N\omega_N + v_D\omega_D) & 0 & 0 \\ \frac{-2v_E\omega_D}{R} & 0 & \frac{-2\mu}{R^3} \end{bmatrix},$$

$$\mathbf{F_{vv}} = \begin{bmatrix} 0 & 2\omega_D & 0 \\ -2\omega_D & 0 & 2\omega_N \\ 0 & -2\omega_N & 0 \end{bmatrix}, \quad \mathbf{F_{v\rho}} = \begin{bmatrix} 0 & f_D & -f_E \\ -f_D & 0 & f_N \\ f_E & -f_N & 0 \end{bmatrix},$$

$$\mathbf{F_{\rho p}} = \begin{bmatrix} \frac{\omega_D}{R} & 0 & 0 \\ 0 & 0 & 0 \\ \frac{-\omega_N}{R} & 0 & 0 \end{bmatrix}, \quad \mathbf{F_{\rho\rho}} = \begin{bmatrix} 0 & \omega_D & -\omega_E \\ -\omega_D & 0 & \omega_N \\ \omega_E & -\omega_N & 0 \end{bmatrix}.$$

The first column of matrix $\mathbf{F}$ is approximated as zero due to the small value of $\frac{\omega_{ie}}{R}$ with respected to v_N, v_E, and v_D.

In eqn. (98), $\mathbf{e_v}$ is the velocity error caused by accelerometer measurement and gravitational model error, and $\mathbf{e}_\rho$ is the attitude error caused by gyroscope measurement error. The quantities $\omega_\mathbf{p}$, $\omega_\mathbf{v}$, and ω_ρ are the position, velocity, and attitude process noise vectors, respectively.

B.3 INS Error State Augmentation

Eqn. (98) shows that the velocity error is driven by accelerometor error and gravitational errors and the attitude error is driven by gyro errors. These errors can be modeled by stochastic Markov processes. The state of these Markov processes is augmented to the INS state. Estimation of the augmented state vector then allows INS error correction and instrument error calibration. Let $\mathbf{x}_a$ denote the states augmented to account for the accelerometer measurement error and the gravitation error. Let $\mathbf{x}_g$ denote the states augmented to account for gyroscope measurement error. Suitable linearized error models are derived in [1, 10]. Linear error models can be defined with matrices $\mathbf{F_{vx_a}}$ and $\mathbf{F_{\rho x_g}}$, such that:

$$\mathbf{e_v} = \mathbf{F_{vx_a}}\mathbf{x}_a + \nu_a \quad (100)$$

$$\mathbf{e}_\rho = \mathbf{F_{\rho x_g}}\mathbf{x}_g + \nu_g \quad (101)$$

where ν_a and ν_g denote the accelerometer measurement noise and gyro measurement noise, respectively.

The state augmentation process leads to a higher dimension state space model, which for observability and computational reasons were reduced to 15 states: the nine error states of eqn. (98), three accelerometer error states, and three gyro error states. The resulting INS linear model is

$$\begin{bmatrix} \delta\dot{\mathbf{p}} \\ \delta\dot{\mathbf{v}} \\ \delta\dot{\rho} \\ \dot{\mathbf{x}}_a \\ \dot{\mathbf{x}}_g \end{bmatrix} = \begin{bmatrix} \mathbf{0} & \mathbf{F_{pv}} & \mathbf{0} & \mathbf{0} & \mathbf{0} \\ \mathbf{F_{vp}} & \mathbf{F_{vv}} & \mathbf{F_{v\rho}} & \mathbf{F_{vx_a}} & \mathbf{0} \\ \mathbf{0} & \mathbf{0} & \mathbf{F_{\rho\rho}} & \mathbf{0} & \mathbf{F_{\rho x_g}} \\ \mathbf{0} & \mathbf{0} & \mathbf{0} & \mathbf{F_{x_a x_a}} & \mathbf{0} \\ \mathbf{0} & \mathbf{0} & \mathbf{0} & \mathbf{0} & \mathbf{F_{x_g x_g}} \end{bmatrix} \begin{bmatrix} \delta\mathbf{p} \\ \delta\mathbf{v} \\ \delta\rho \\ \mathbf{x}_a \\ \mathbf{x}_g \end{bmatrix} + \begin{bmatrix} \omega_\mathbf{p} \\ \omega_\mathbf{v} + \nu_a \\ \omega_\rho + \nu_g \\ \omega_\mathbf{a} \\ \omega_\mathbf{g} \end{bmatrix}. \quad (102)$$

The variables $\mathbf{x}_a$ and $\mathbf{x}_g$ represent a composite of accelerometer and gyro errors, some of which are slowly time varying. For convenience, they will be referred to as accelerometer and gyro biases, respectively. These

states are modeled as random walk processes. Therefore, $\mathbf{F}_{\mathbf{x}_a\mathbf{x}_a}$ and $\mathbf{F}_{\mathbf{x}_g\mathbf{x}_g}$ are identically zero. The power spectral densities for the driving noise processes $\omega_\mathbf{a}$ and $\omega_\mathbf{g}$ were determined by analysis of the instrument biases over an extended period of time. The quantities ν_a and ν_g are the (zero mean) accelerometer and gyro measurement noise vectors. The spectral densities of the measurement noise processes ν_a and ν_g were determined by the analysis of measurement data. The matrices $\mathbf{F}_{\mathbf{v}\mathbf{x}_a}$ and $\mathbf{F}_{\rho\mathbf{x}_g}$ can be processed, by the chain rule, as:

$$\mathbf{F}_{\mathbf{v}\mathbf{x}_a} = \frac{\partial v}{\partial \mathbf{f}^b}\frac{\partial \mathbf{f}^b}{\partial \mathbf{x}_a} \tag{103}$$

$$= \mathbf{R}_{b2t}\frac{\partial \mathbf{f}^b}{\partial \mathbf{x}_a} \tag{104}$$

$$\mathbf{F}_{\rho\mathbf{x}_g} = \frac{\partial \rho}{\partial \omega_{ib}^b}\frac{\partial \omega_{ib}^b}{\partial \mathbf{x}_g} \tag{105}$$

$$= \mathbf{R}_{b2t}\frac{\partial \omega_{ib}^b}{\partial \mathbf{x}_g} \tag{106}$$

with $\frac{\partial \mathbf{f}^b}{\partial \mathbf{x}_a} = \frac{\partial \omega_{ib}^b}{\partial \mathbf{x}_g} = \mathbf{I}$. This completes the summary of the specification of the INS error dynamic model.

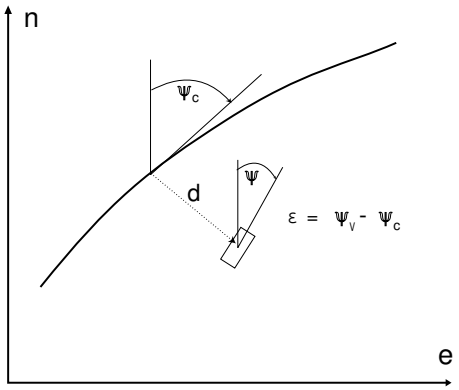

Figure 27: Control State Definition.

C Control State

The main topic of this section is presentation of the algorithm used to determine the trajectory relative control state based on the CP DGPS/magnetometer/INS navigation state information. The data flow for this calculation is shown in Figs. 1 and 2. The CP DGPS/magnetometer/INS state is an absolute quantity in the sense that it generates the absolute vehicle position in an earth relative frame. Since the control objective is to follow a trajectory, the control system utilizes a trajectory relative state vector defined in Table 4 and Fig. 27. As Figs. 1 and 2 show, a lane trajectory and the CP DGPS/magnetometer/INS state are inputs to an algorithm that computes the control state vector as required for the PATH vehicle control algorithm. The subsequent presentation uses various concepts from analytic geometry that are reviewed in Appendix D.

Symbol	Units	Description
d	m	Off-track distance
$\dot{d}$	$\frac{m}{s}$	Time derivative of d
ϵ	$rads$	Heading error ($= \psi - \psi_c$)
$\dot{\epsilon}$	$\frac{rads}{s}$	Time derivative of heading error
$\mathbf{v}_T$	$\frac{m}{s}$	Velocity tangent to trajectory
R_κ	m	Radius of curvature ($= \frac{1}{\kappa}$).

Table 4: The Control State Definition

C.1 Lane Trajectory Definition

Given a set of data $\mathcal{D} = \{t_i, n_i, e_i, v_{n_i}, v_{e_i}\}_{i=1}^N$ corresponding to the time stamp, north and east coordinates, and north and east components of the velocity acquired along a trajectory, the objective of this section is to define a twice differentiable function $\mathbf{p}(s)$ that fits the data in $\mathcal{D}$. For convenience, the parameter s is considered to be arclength.

The arclength defined by eqn. (126) can be approximated for $1 < i \leq N$ as

$$u_i = \sqrt{v_{n_i}^2 + v_{e_i}^2} \tag{107}$$

$$s_i = s_{i-1} + u_i(t_i - t_{i-1}) \tag{108}$$

where s_0 is assumed to be zero.

Let the curve fit trajectory be defined as

$$\mathbf{p}(s) = [n(s), e(s)] = \phi(s)^T [\theta_n, \theta_e] \tag{109}$$

where $\theta_n, \theta_e \in \Re^m$, $\phi(s) : \Re \mapsto \Re^m$, and m is the number of parameters in the curve fit. The vector of functions ϕ is the basis for the curve fit. This basis should be at least twice differentiable for the reasons

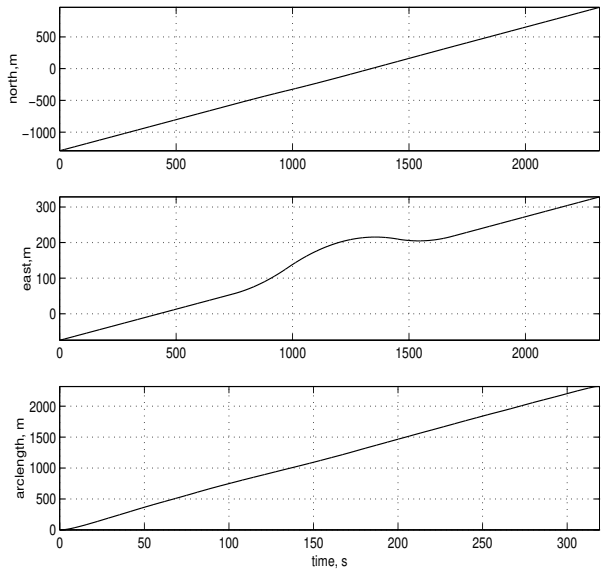

Figure 28: Horizontal position data versus arclength and arclength versus time for measured trajectory data.

discussed after eqn. (133). Let the matrix Φ be defined as

$$\Phi = \begin{bmatrix} \phi(s_1)^T \\ \vdots \\ \phi(s_N)^T \end{bmatrix}. \tag{110}$$

Then the least squares estimate of the curve fit parameters is

$$[\theta_n, \theta_e] = \left(\Phi^T \Phi\right)^{-1} \Phi^T [\mathbf{n}, \mathbf{e}] \tag{111}$$

where $\mathbf{n}$ and $\mathbf{e}$ are the column vectors containing the north and east coordinates from $\mathcal{D}$.

Figure 28 shows the GPS/INS data that is the input to the trajectory curve fitting procedure, for the Crows Landing trajectory. This data was acquired at 15 Hz while the vehicle was driven along a trajectory defined by embedded magnets. During the data acquisition, magnetometer control was used for lateral positioning. The speed was manually controlled at approximately 8 $\frac{m}{s}$, resulting in trajectory points separated by approximately 0.5 m. The trajectory starts and ends with straight segments and has three turns. Each turn has a radius of curvature of approximately 800 m. The vehicle was driven in the north bound direction. The three turns are clearly evident in the plot of the east coordinate. Figure 29 shows the curve fit trajectory on the left and the heading and curvature of the trajectory versus arclength on the right.

C.2 Control State Calculation

This subsection describes the method for calculating the control state based on the trajectory and the CP DGPS/magnetometer/INS state. The inputs to the algorithm from the navigation system are the horizontal position $[n_i, e_i]$, the horizontal velocity $[v_{n_i}, v_{e_i}]$, the heading ψ_i, and the yaw rate g_{z_i} of the vehicle at time t_i. The required control state information is defined in Table 4.

The first step of the algorithm is to find the arclength along the trajectory that produces the trajectory position nearest to the vehicle position. Given the arclength from the previous time step, the arclength for the present time step is approximately

$$s_i = s_{i-1} + \sqrt{v_{n_i}^2 + v_{e_i}^2}\, dt \tag{112}$$

where $dt = t_i - t_{i-1}$. A local search is then required to tune s_i to the required accuracy.

Define the cost function $J(s) = \|[n_i, e_i] - \mathbf{p}(s)\|$. The gradient of the cost function is

$$\frac{\partial J}{\partial s} = \left(\frac{[\tilde{n}, \tilde{e}]}{J(s)} \begin{bmatrix} \theta_n^T \\ \theta_e^T \end{bmatrix} \frac{d\phi}{ds} \right)$$

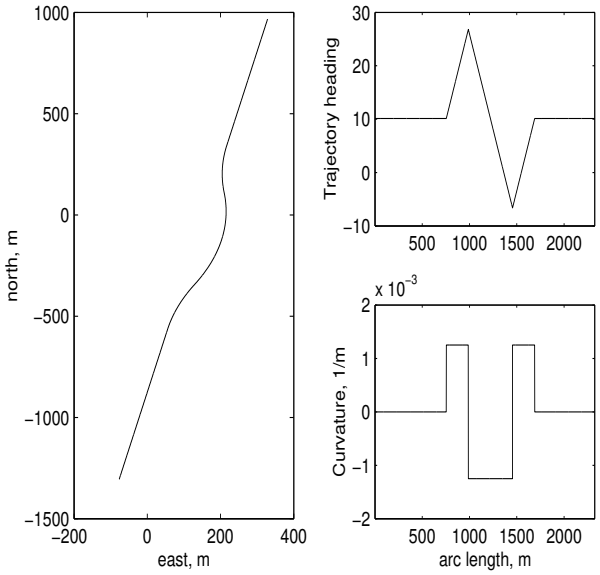

Figure 29: Curve fit trajectory and trajectory heading and curvature versus arclength.

which is a function of s. The position errors are defined as $[\tilde{n}, \tilde{e}] = [n_i, e_i] - \mathbf{p}(s)$. The gradient algorithm proceeds by initializing $\mu_0 = s_i$ and iterating

$$\mu_j = \mu_{j-1} - \alpha \left. \frac{\partial J}{\partial s} \right|_{s=\mu_{j-1}}$$

until $|\mu_j - \mu_{j-1}|$ is small. Then define $s_i = \mu_j$. Convergence usually succeeds in fewer than 6 iterations.

Given the nearest trajectory point $\mathbf{p}(s_i)$, the navigation system information $[n, e, v_n, v_e, \psi, g_z]$ and the analytic geometry relations of Appendix D, the elements of the control state are calculated as

$$\begin{aligned} d &= [\tilde{n}, \tilde{e}] \cdot \mathbf{N}(s_i) && (113) \\ \dot{d} &= [v_n, v_e] \cdot \mathbf{N}(s_i) && (114) \\ \epsilon &= \psi - \psi_c(s_i) && (115) \\ \mathbf{v}_T &= [v_n, v_e] \cdot \mathbf{T}(s_i) && (116) \\ R_\kappa &= \frac{1}{|\kappa(s_i)|} && (117) \\ \dot{\epsilon} &= g_z - r_c && (118) \end{aligned}$$

where $\psi_c, r_c, \mathbf{N}(s), \mathbf{T}(s),$ and $\kappa(s)$ are defined in Appendix D.

C.3 Trajectory Relative Maneuvers

This subsection describes the algorithms to implement a library of advanced vehicle maneuvers as a perturbation to a predefined trajectory.

Let $d = p(l)$ denote a function describing the desired of distance perturbation to a trajectory to implement a maneuver, as a function of a parameter l. Assuming pitch and roll are zero, the trajectory relative heading is small, and the side slip is zero, the kinematics of a maneuver are described by

$$\begin{bmatrix} \dot{d} \\ \dot{\epsilon} \end{bmatrix} = \begin{bmatrix} u(t)\epsilon(t) \\ u(t)\kappa(t) \end{bmatrix} \quad (119)$$

where $R = \frac{1}{\kappa}$ is the turning radius, ϵ is the trajectory relative vehicle heading, $u(t) = \frac{ds}{dt}$ is the vehicle speed, and s is the arclength.

From the functional description of the maneuver,

$$\dot{d} = \frac{dp}{dl}\frac{dl}{dt} = \frac{dp}{dl}\frac{dl}{ds}u$$

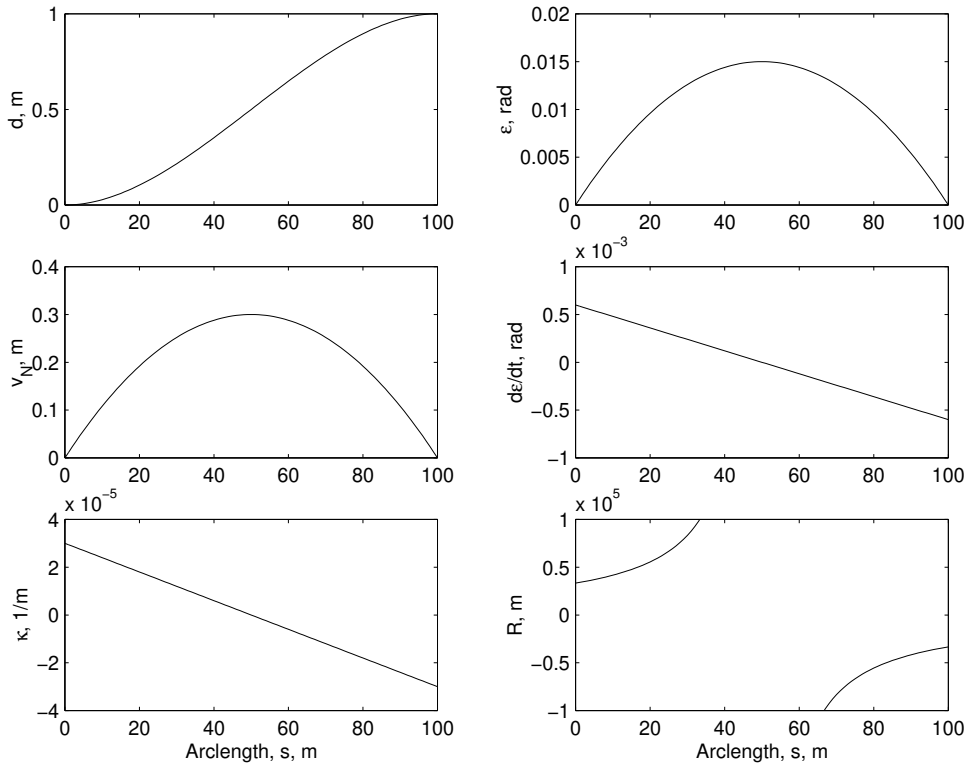

Figure 30: Example Maneuver Variables with $u = 20$ m/s.

and

$$\ddot{d} = \frac{d^2p}{dl^2}\left(\frac{dl}{dt}\right)^2 + \frac{dp}{dl}\frac{d^2l}{dt^2}$$

where the time rate of change can be selected at the time the maneuver is specified. Combining this with the kinematics yields

$$\epsilon = \frac{\dot{d}}{u} = \frac{dp}{dl}\frac{dl}{ds}.$$

Therefore,

$$\dot{\epsilon} = \frac{d^2p}{dl^2}\left(\frac{dl}{ds}\right)^2 u + \frac{dp}{dl}\frac{d^2l}{ds^2}\dot{u}.$$

Setting the above equation equal to the kinematic equation yields

$$\kappa = \frac{d^2p}{dl^2}\left(\frac{dl}{ds}\right)^2 + \frac{dp}{dl}\frac{d^2l}{ds^2}\frac{\dot{u}}{u}.$$

or

$$R = \frac{1}{\frac{d^2p}{dl^2}\left(\frac{dl}{ds}\right)^2 u + \frac{dp}{dl}\frac{d^2l}{ds^2}\dot{u}}.$$

ExampleThe polynomial $p(l) = l^2(3-2\,l)$ maps the interval $[0,1]$ to $[0,1]$ while having zero slope at both endpoints. Scaling l and the amplitude of $p(l)$ would accomplish a lane change maneuver. The derivatives of p are

$$\frac{dp}{dl} = 6l(1-l) \tag{120}$$

$$\frac{d^2p}{dl^2} = 6(1-2l). \tag{121}$$

Let $l = \frac{s}{100}$ where s is the arclength. Then, the maneuver will be complete in 100 m. Therefore,

$$\dot{d} = 6u\left(\frac{s}{100}\right)\left(1-\frac{s}{100}\right)\left(\frac{1}{100}\right) \tag{122}$$

$$\epsilon = 6\left(\frac{s}{100}\right)\left(1-\frac{s}{100}\right)\left(\frac{1}{100}\right) \tag{123}$$

$$\dot{\epsilon} = \frac{6}{10^4}\left(1-\frac{s}{50}\right). \tag{124}$$

These control state perturbations, useful for accomplishing a lane change maneuver with amplitude 1.0 m, are plotted in Figure 30.

D Concepts from Analytic Geometry

Given a function $\mathbf{p}(s)$ defining a two dimensional trajectory as a function of arclength s, this section reviews various concepts from analytic geometry that are used in the the main body of the report.

Let $u(t)$ denote the speed of travel. Then,

$$u(t) = \frac{ds(t)}{dt} = \|\mathbf{v}(t)\| \tag{125}$$

where $\mathbf{v}(t)$ is the velocity of a point moving along the trajectory. Since the point $\mathbf{p}$ is confined to the trajectory, $\mathbf{v}(t)$ is tangent to the trajectory by definition. Note that

$$s(t) = \int_0^t u(\tau)d\tau \tag{126}$$

which is used in both the trajectory curve fit and control algorithms.

When the trajectory is linearly parameterized as

$$\mathbf{p}(s) = \phi(s)^T[\theta_n, \theta_e] = \phi(s)^T\Theta, \tag{127}$$

where $\theta_n, \theta_e \in \Re^m$ and $\phi(\cdot) : \Re \mapsto \Re^m$, then the velocity along the trajectory satisfies

$$\mathbf{v}(t) = \frac{d\mathbf{p}(t)}{dt} = \frac{d\mathbf{p}(t)}{ds}\frac{ds}{dt} \tag{128}$$

$$= \left(\frac{d\phi}{ds}\right)^T \Theta u(t). \tag{129}$$

Since $u(t)$ is by definition the magnitude of $\mathbf{v}(t)$, the vector

$$\mathbf{T} = \frac{\mathbf{v}(t)}{u(t)} = \left(\frac{d\phi}{ds}\right)^T \Theta \tag{130}$$

is the unit vector tangent to the trajectory. Define the components of $\mathbf{T}$ as $\mathbf{T} = [T_1, T_2, 0]$. Then, the trajectory heading is

$$\psi(s) = arctan2(T_2, T_1) \tag{131}$$

where $arctan2$ is a four quadrant arctangent. The normal to the trajectory, defined positive to the right in the direction of travel, is by the right hand rule

$$\mathbf{N} = \begin{vmatrix} \hat{\mathbf{i}} & \hat{\mathbf{j}} & \hat{\mathbf{k}} \\ T_1 & T_2 & 0 \\ 0 & 0 & -1 \end{vmatrix} = \begin{bmatrix} -T_2 \\ T_1 \\ 0 \end{bmatrix}. \tag{132}$$

The trajectory curvature vector $\mathbf{K}$ is the derivative of $\mathbf{T}$ with respect to s. Since $\mathbf{T}$ is a unit vector, only its direction can change. The scalar trajectory curvature κ is the norm of $\mathbf{K}$. Therefore, with the trajectory defined as in eqn. (127),

$$\kappa = \left\|\frac{d\mathbf{T}}{ds}\right\| = \left\|\left(\frac{d^2\phi}{ds^2}\right)^T \Theta\right\|, \tag{133}$$

which has units of m^{-1}. Therefore, for the curvature to be well-defined, the basis functions must be at least twice differentiable with respect to s. Based on the curvature κ and speed of travel along the trajectory v_T, the magnitude of the vehicle rotation rate in $\frac{radians}{s}$ should be $\frac{v_T}{R_\kappa}$ where $R_\kappa = \frac{1}{\kappa}$. The sign of the desired vehicle rotation rate depends on the direction in which the tangent is rotating and can be determined as the sign of the third component of $\mathbf{T} \times \mathbf{K}$, so that

$$
\begin{aligned}
r_c &= ((\mathbf{T} \times \mathbf{K}) \cdot [0, 0, 1])\, v_T && (134)\\
&= \|\mathbf{T}\|\|\mathbf{K}\| \sin(\theta_{TK}) v_T && (135)\\
&= \kappa v_T \sin(\theta_{TK}) && (136)\\
&= \sin(\theta_{TK}) \frac{v_T}{R_\kappa} && (137)
\end{aligned}
$$

where r_c denotes the desired yaw rate command and θ_{TK} is the angle between $\mathbf{T}$ and $\mathbf{K}$ which is always ± 90 degrees.